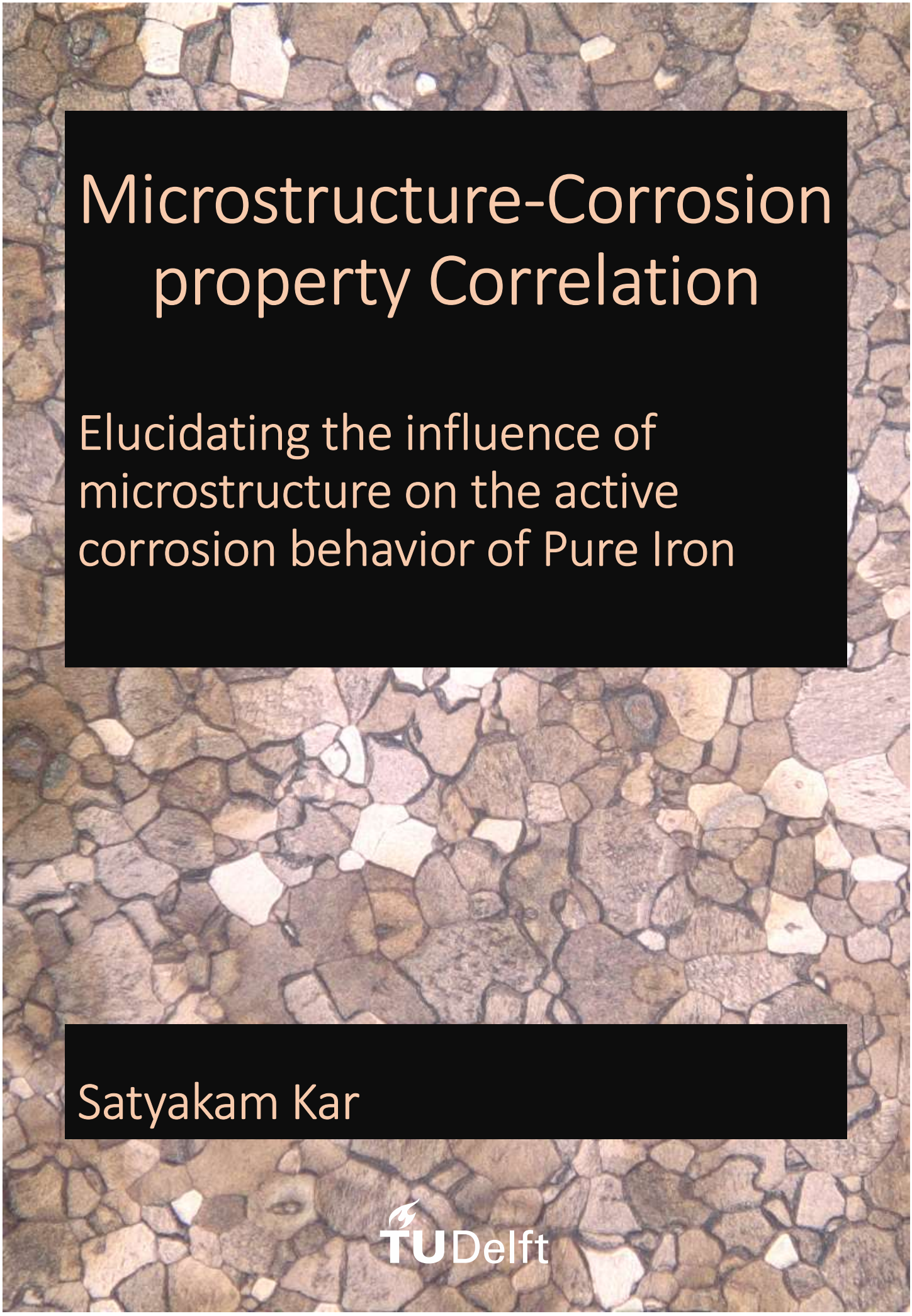

Microstructure-Corrosion property Correlation

Elucidating the influence of microstructure on the active corrosion behavior of Pure Iron

Satyakam Kar

TU Delft

Microstructure-Corrosion property Correlation

Elucidating the influence of microstructure on the active corrosion behavior of Pure Iron

by

Satyakam Kar

in partial fulfilment of the requirements for the degree of

Master of Science in Materials Science and Engineering
at the Delft University of Technology,
to be defended publicly on Friday October 23, 2020 at 3:00 PM.

Student number:	4796306	
Thesis committee:	Dr. Y. Gonzalez-Garcia,	TU Delft, Supervisor
	Prof. dr. J. Sietsma,	TU Delft
	Dr. P. Taheri,	TU Delft
	Dr. J. G. Buijnsters,	TU Delft
	A. Yılmaz,	TU Delft, Daily supervisor

TU Delft

Acknowledgement

This Master's thesis project has been a wonderful learning experience of my life. I would like to acknowledge the people for helping me with the successful completion of the project.
I express sincere gratitude to my supervisor Assoc. Prof. Yaiza Gonzalez-Garcia for her support and guidance during the project. I appreciate your valuable advice and motivation during the challenging period of the COVID pandemic.
I thank my daily supervisor Aytac Yılmaz for his continuous feedback and assistance with the experiments. I appreciate your calmness and constructive feedback. My sincere thanks to Konstantina Traka for her valuable inputs on modeling study and texture analysis.
I would also like to thank the lab technicians Agnieszka Kooijman-Banaszak and Sander van Asperen for practical tips and training. I thank Ruud Hendrikx for performing the XRD texture measurements.
I thank fellow Master and PhD students working at the corrosion lab for pleasant conversations and friendly environment during the project.
Finally, I thank my family for being with me through thick and thin.

Satyakam Kar
Delft, October 2020

Abstract

Microstructure-corrosion property correlation is an open question in the field of materials science. The microstructure of metals and alloys consists of several features with different individual corrosion response. The corrosion behavior of the macroscopic system is an outcome of the complex interaction of the components of microstructure. Hence, a definitive understanding of the corrosion response of the microstructural features is needed for improving the material durability and design.
In the present work, the effect of grain size on the active corrosion behavior of pure iron is investigated. Samples with different grain sizes are obtained by annealing heat-treatment. The microstructure of samples is characterized by optical microscopy, electron backscatter diffraction and X-ray diffraction. Electrochemical characterization using potentiodynamic polarization and electrochemical impedance spectroscopy are performed on the samples in deaerated 0.1 M and 0.01 M H_2SO_4 solutions. The surface topography of the corroded sample surface is characterized by atomic force microscopy. Following the experiments, a numerical corrosion model is attempted to replicate the observations. The results reveal an aggregate effect of grain size and crystallographic orientation of grains on the corrosion behavior of the samples.

Contents

List of Figures

List of Tables

1

Introduction

Corrosion is an important natural phenomenon associated with metals. Its significance in the design and selection of materials for engineering applications stems from its ability to deteriorate the integrity of metallic structures over time. This poses a danger to human life and safety. According to a recent study by the National Association of Corrosion Engineers (NACE), the global expenditure on corrosion is estimated to be around 2.5 trillion USD. This value amounts to about 3.4% of the global gross domestic product of 2013 [1]. Based on the application, suitable corrosion control and prevention techniques are employed. Hence, it is essential to develop a fundamental understanding of the factors influencing the corrosion resistance of a material in a given environment.

Apart from chemical composition, the processing operation of a material has a significant effect on the corrosion behavior due to its ability to modify the microstructure. This modification in microstructure can manifest in the form of change in grain size, grain boundary density, internal stress, preferential crystallographic orientation, formation of precipitates and intermetallic compounds, and segregation of alloying elements [2]. Each of these variables individually influences the corrosion behavior. Out of these variables, the grain size is of particular interest for metallurgists because of the well-known Hall-Petch relation. It predicts an improvement in yield strength with grain refinement. The mechanical properties of metals and alloys improve with grain refinement [3–6]. On the contrary, the effect of grain size on the corrosion behavior of metals is not apparent. Previous works have reported both an increase and a decrease in corrosion rate with a reduction in grain size, as reviewed by Ralston et al. [2] and Miyamoto et al. [7]. In these works, the contradictory conclusions primarily arise due to the predominant influence of microstructural parameters other than grain size on the material's corrosion behavior. Secondly, the corrosion behavior of the material also depends on the solution environment. In the active condition, the corrosion response is governed by the resistance of the material to dissolution. In the passive condition, the corrosion response depends on the quality and stability of the passive film [8]. Hence, it is essential to consider all the contributing factors while performing corrosion studies on the effect of grain size.

Studies focusing on the grain size effect on corrosion have been performed on pure metals to eliminate the effects of precipitates and segregation of alloying elements. Ralston et al. [9] studied the effect of grain size on the corrosion of pure aluminum in 0.1 M NaCl solution. They observed a decrease in the corrosion rate with a decrease in grain size. Different processing routes were used in the work to vary the grain size. They conclude texture and internal stress could have affected the corrosion behavior. A similar study was done by Op't Hoog et al. [10]

with pure magnesium in 0.1 M NaCl solution. They observed a significant improvement in corrosion resistance of samples fabricated by equal channel angular pressing (ECAP). They highlighted the role of the processing route adopted to achieve a microstructure with superior corrosion resistance. In these studies, the exact role of grain size in the corrosion response remains hidden under overlapping effects of texture and internal stress. Lapeire et al. [11] studied the effect of grain size on the corrosion behavior of pure copper in 0.1 M HCl solution. They successfully achieved texture and internal stress at similar levels across the samples. They observed an increase in the corrosion rate with reduction in grain size. Limited studies on the relation between grain size and corrosion have been conducted in pure iron as well [12–15]. However, these studies lack a comprehensive characterization of microstructure and report a dominant influence of texture and internal stress generated during processing. Since iron and its alloys are widely used for engineering applications, it is necessary to explore the effect of grain size on the corrosion behavior of iron in detail.

1.1. Aim of the thesis

The current work aims to understand the effect of grain size on the corrosion behavior of pure iron. The scope of this work is limited to understanding the corrosion behavior in the active condition. Material processing is carried out by annealing cold rolled iron sheet to obtain a set of samples with different grain sizes. The microstructure of the samples is characterized by optical microscopy, X-ray diffraction (XRD), and electron backscatter diffraction (EBSD). The corrosion behavior of these samples is studied in deaerated 0.1 M H_2SO_4 and 0.01 M H_2SO_4 solutions. The central research question and hypothesis for the current work are summarized as follows:

Research question

What is the influence of grain size on the corrosion behavior of pure iron in the active condition?

Hypothesis

In the active condition, the corrosion behavior of a metal is governed by its resistance to undergo dissolution in the environment. By reducing the grain size, the grain boundary density in the metal increases. Since grain boundaries are characterized by a disordered arrangement of atoms with less than usual atomic coordination, they have a higher susceptibility to corrosion attack. Hence, without the predominant influence of other microstructure features, it is expected that the corrosion rate increases with a decrease in grain size.

1.2. Thesis outline

The thesis consists of five chapters. In chapter 1, a brief introduction to the current work is given. Chapter 2 presents a detailed review of the fundamental concepts and existing literature related to the current research work. Chapter 3 describes the material and the methods followed to perform the experiments and modeling studies. Chapter 4 includes the results achieved in the current work, along with a critical interpretation. Finally, in chapter 5, the concluding remarks are provided along with recommendations based on the current work.

2

Literature review

This chapter provides a detailed overview of the fundamental concepts and relevant literature for the present work. The chapter is divided into four sections. In the first section, the fundamentals of corrosion are explained with iron as the focal point. The second section describes the passivity of iron. The third section elucidates the role of processing induced variables on the corrosion behavior of metals, and the fourth section presents the principles of corrosion modeling with focus on the numerical modeling of corrosion.

2.1. Corrosion of iron

Corrosion refers to the degradation of material over time due to interaction with its environment. According to IUPAC, corrosion is defined as the *"irreversible interfacial reaction of a material (metal, ceramic, polymer) with its environment which results in consumption of the material or in dissolution into the material of a component of the environment. Often, but not necessarily, corrosion results in effects detrimental to the usage of the material considered. Exclusively physical or mechanical processes such as melting or evaporation, abrasion or mechanical fracture are not included in the term corrosion [16]."* Corrosion of metals is an electrochemical reaction. It involves charge and mass transfer. The electrochemical reaction comprises anodic (oxidation) and cathodic (reduction) reactions to maintain charge balance. In the corrosion of iron, the anodic reaction involves oxidation of iron to give ferrous ion and two electrons (equation 2.1). The cathodic reaction depends on the environment condition. The cathodic reactions corresponding to different environments are given in equations 2.2-2.5 [17].

$$Fe(s) \rightarrow Fe^{2+}(aq) + 2e- \tag{2.1}$$

$$2H^{+}(aq) + 2e- \rightarrow H_2(g) \quad \text{pH} \leqslant 7, \text{ no } O_2 \tag{2.2}$$

$$2H_2O(l) + 2e- \rightarrow H_2(g) + 2OH^{-}(aq) \quad \text{pH} \geqslant 7, \text{ no } O_2 \tag{2.3}$$

$$O_2(g) + 4H^{+}(aq) + 4e- \rightarrow 2H_2O(l) \quad \text{pH} \leqslant 7, O_2 \tag{2.4}$$

$$O_2(g) + 2H_2O(l) + 4e- \rightarrow 4OH^{-}(aq) \quad \text{pH} \geqslant 7, O_2 \tag{2.5}$$

The atmospheric corrosion of iron is called 'rusting.' The cathodic reaction, in this case, is equation 2.5. The overall reaction results in the formation of ferrous hydroxide. The ferrous hydroxide gets further oxidized in the presence of water to give hydrated ferric oxide (rust). The schematic of these processes is shown in fig. 2.1 [17].

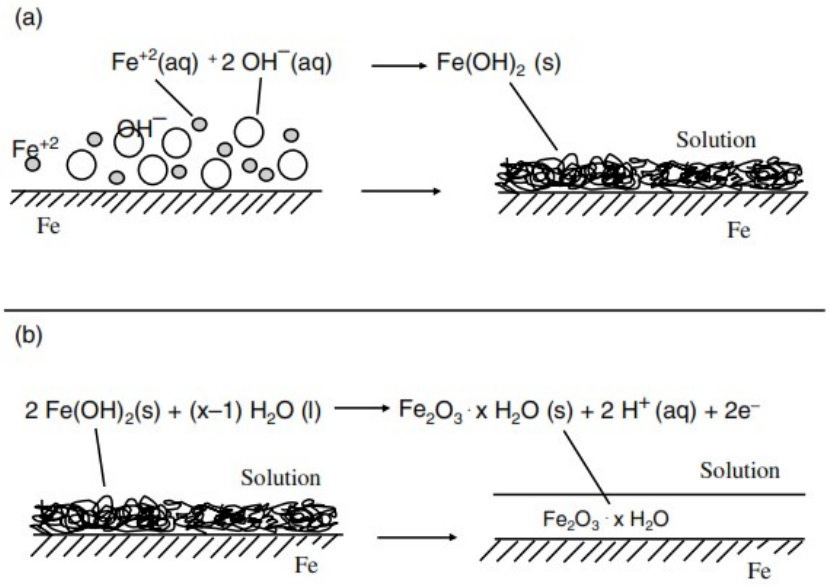

Figure 2.1: Schematic representation of rusting of iron by (a) precipitation of ferrous hydroxide and then (b) conversion to hydrated ferric oxide [17]

Every corrosion process needs anodic reaction, cathodic reaction, and mediums for conduction of ions and electrons. When metal is in an aqueous environment, interface develops between the two phases. The charge-distribution across this interface is called the electrical double layer. The electrical double layer results in a potential difference between the metal and the solution medium. This is also known as the absolute electrode potential. Since it is not possible to measure the absolute electrode potential, it is always reported against a reference electrode potential. The potential of the hydrogen electrode under standard conditions (SHE) is the reference and set as 0 V. The standard electrode potential (E^0) of different metals is summarized in the electromotive force (EMF) series. It gives an idea of the reactivity of a metal. Under non-standard conditions, the electrode potential of a metal (E) can be calculated using the Nernst equation (equation 2.6). Here, n is the number of electrons involved in the reaction, F is Faraday's constant, R is the universal gas constant, T is the absolute temperature. a_P and a_R are the activities of products and reactants, respectively [17].

$$E = E^0 - \frac{RT}{nF} ln\left(\frac{a_P}{a_R}\right) \tag{2.6}$$

A convenient approach to study the corrosion behavior of a metal given by thermodynamics is the Pourbaix diagram. Pourbaix diagram of metal shows its corrosion tendency by defining species stable under different combinations of potential and pH. Fig. 2.2 shows the Pourbaix diagram of iron at 25°C and dissolved ionic activity of 10^{-6} M. The potential is reported with respect to SHE. The lines in the diagram have been drawn using the Nernst equation for a reaction involving neighboring species in the plot. The dotted lines (a) and (b) mark the stability region of water. Regions favoring the formation of ions are marked 'corrosion'and denote active corrosion condition. The regions promoting the formation of protective oxide film on the surface of iron are marked 'passivity'. At potential below -0.62 V, iron remains immune to any corrosive action. However, at higher potential, it readily oxidizes to Fe^{2+} ions across acidic to neutral pH mediums. Fe^{2+} ions oxidize to Fe^{3+} ions above 0.77 V. Unfortunately, the Pourbaix diagram has limitations as well. It applies to pure metals only. It does not give any information about the rate of corrosion. The role of chloride ions in localized corrosion and the protective

properties of the passive films are missing [17]. Electrochemical techniques can be used to measure corrosion kinetics. The theory of the methods are discussed in the section 3.3.1.

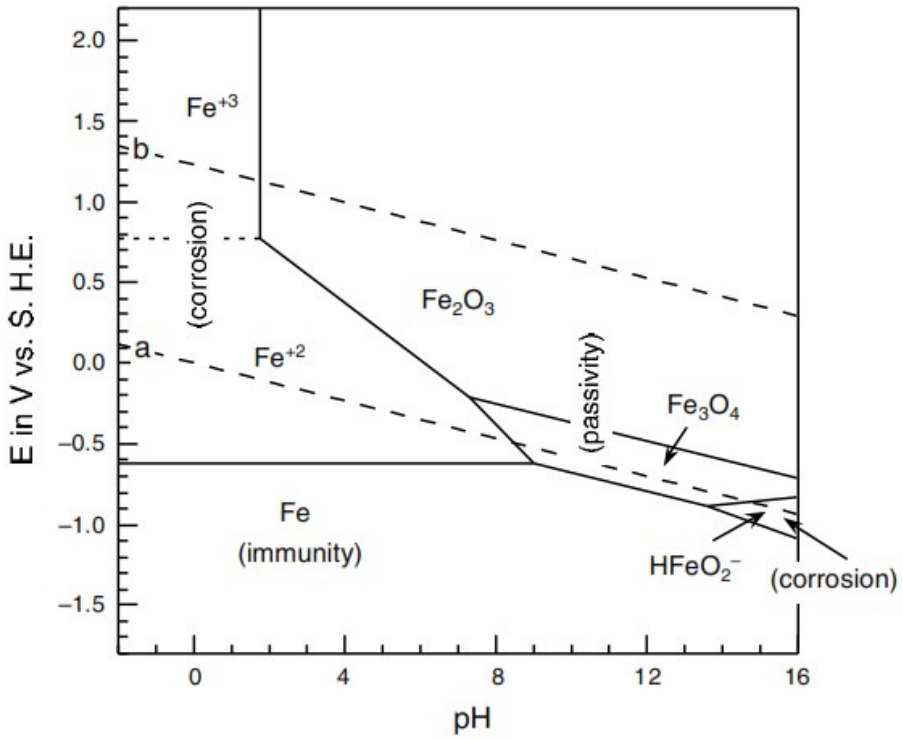

Figure 2.2: Pourbaix diagram of iron at 25°C and 10^{-6} M dissolved ionic concentration [17].

2.2. Passivity of iron

Passivity is the property of metals and alloys to resist corrosion under oxidizing conditions by forming a protective film on the surface. The film, formed by the reaction of the metal with its environment, reduces the corrosion rate by acting as a barrier for the environment. Passivity is observed in a large group of metals, including iron. Transition metals and their alloys usually form thin passive films in the order of tens to several hundred angstroms [17]. The properties of the passive film depend on the metal being studied and environmental factors like temperature, pH, and redox potential. The passivation process can be visualized from anodic polarization of the metal. Fig. 2.3 shows a schematic anodic polarization curve of an active-passive metal. On scanning in the anodic direction, the current density linearly increases, followed by a sudden decrease at a specific anodic potential. This potential is called the Flade potential or passivation potential (E_{PP}). On further increasing the potential, the current density remains more or less invariant, followed by an increase again at a higher anodic potential. The Flade potential marks the transition from active to passive behavior due to the formation of a passive film. Hence, the current density corresponding to the Flade potential is called the critical current density (i_{crit}). i_{pass} denotes the current density in the passive region. Beyond the passive region, the current density increases again because of the breakdown of the passive layer or decomposition of water in the solution. This region is designated as the transpassive region. The shape of the polarization curve is sensitive to environmental conditions [17, 18].

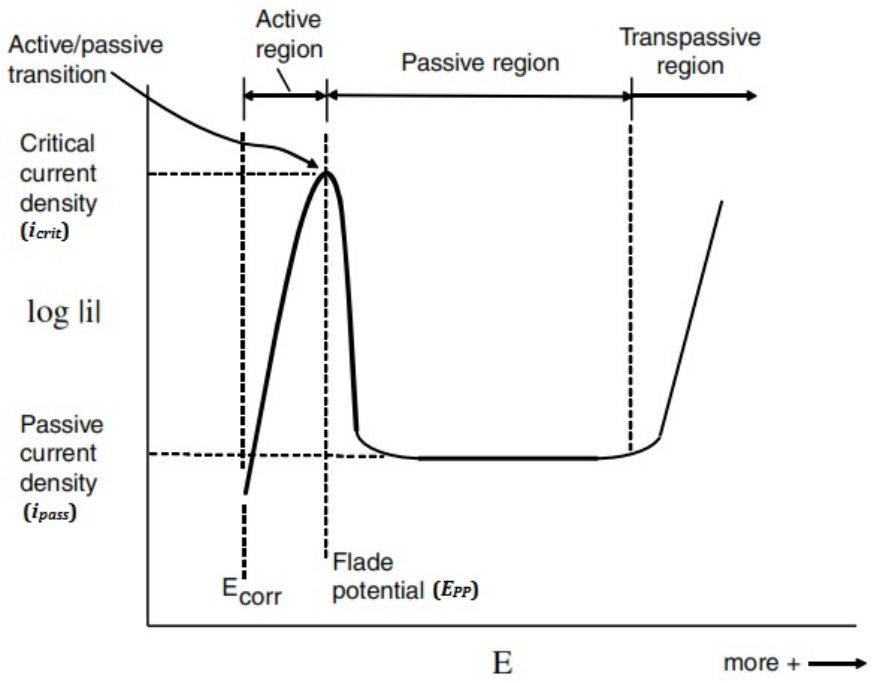

Figure 2.3: Schematic anodic polarization curve for active-passive metal

For iron, the Pourbaix diagram shows the regions of passivity where Fe_2O_3 and Fe_3O_4 formation is favorable. Passivation studies on iron do not agree unanimously on the structure and composition of the film. The disagreements arise due to the difference in conditions used to form the passive film, low thickness of the film, and possible modification of the film while performing ex-situ studies [17, 19]. Nevertheless, understanding the passivity of iron is fundamental to studies on improving the passivation properties of iron by the addition of alloying elements. Some of the widely accepted models for passivity of iron are discussed further briefly.

2.2.1. Duplex layer model

As per this model, the passive film of iron consists of two layers. The inner layer is made of Fe_3O_4, while the outer layer is made of γ-Fe_2O_3. This model is supported by the work of Nagayama and Cohen [20], who studied the passivity of iron in a borate buffer solution (pH=8.4). During cathodic reduction of the passive film, they observed two distinct plateaus in the cathodic reduction curves associated with the reduction of the outer Fe_2O_3 layer and then the inner Fe_3O_4 layer. Studies using different characterization techniques have confirmed the duplex layer model [21–23]. In contradiction, some studies have shown the occurrence of a two-stage reduction for homogeneous film composed only of Fe_2O_3 [24, 25].

2.2.2. Hydrous oxide model

This model states that the passive film of iron contains water. It might be in the form of hydrated oxides or hydroxides. Revie et al. [26] used auger electron spectroscopy to study the passivation of iron in $KOH+H_3BO_3$ solution (pH=8.1) with special care to avoid contamination. They reported the formation of hydrated ferric oxide. Murphy et al. [27] used the secondary-ion mass spectrometry (SIMS) and confirmed the presence of water in the passive film. However, the SIMS study by Mitchell et al. [28] showed that hydroxyl groups were only present on the surface. Similarly, XPS study on the passive film of iron in borate and phosphate buffer solutions showed the presence of water at the surface only [29].

2.2.3. Spinel/Defect model

This model states that the passive film on iron is a single-phase nanocrystalline spinel oxide with many defects. It bears similarity but different from Fe_2O_3 and Fe_3O_4. The model was supported by in-situ X-ray studies that found different Fe - Fe distance and site occupancies of Fe^{2+}/Fe^{3+} in the passive film than that is found in any known oxides or hydroxides [30, 31]. Davenport et al. [32] in their study called this new phase as the LAMM phase.

The growth and dissolution of the passive film on iron are well explained by the point defect model proposed by MacDonald and co-workers [33–35]. The model is based on the idea that the passive film has point defects like cationic and anionic vacancies and cationic interstitials. The film starts forming above the Flade potential. The film is associated with a high electric field close to the level of dielectric breakdown and hence can be treated like a semiconductor. In iron, the major defects are the Fe interstitial and oxygen vacancies. Hence, the film behaves like an n-type semiconductor. During the growth process, the defects are generated and annihilated at the metal-film and film-solution interfaces. In the case of iron, the growth kinetics is controlled by the diffusion of cation vacancies. The film growth stops when there is a condensation of uncharged metal vacancies at the metal-film interface, resulting in separation.

2.3. Effect of processing induced factors on corrosion

All metals and alloys invariably undergo several stages of processing (thermal, mechanical, thermo-mechanical) to attain a microstructure which fulfills the desired application requirements. From the fundamentals of corrosion, it is known that every corrosion process is a couple of anodic and cathodic reactions. These reactions occur on the same metal surface. This is possible because the surface of the metal has heterogeneous energy distribution. It contains defects (grain boundaries, dislocations), crystal orientations with different packing densities of atoms, and possible surface contamination [17]. During processing, the heterogeneity of metal surface can change, resulting in varying corrosion behaviors with different processing methods for the same metal. Hence, it is essential to understand the effect of the processing induced factors on corrosion. These factors include grain size, crystallographic texture, residual stress, segregation of impurities, segregation of precipitates, and alloying elements [2]. In the present study, the focus is on pure metals to eliminate the role of alloying additions and precipitates.

2.3.1. Grain size

Grain size is the fundamental feature for describing the microstructure of metals. Most of the metal processing techniques aim at achieving fine grain size to improve the mechanical properties of the metals. The familiar Hall-Petch relation demonstrates the improvement in strength with the reduction in grain size. As the grain size decreases, the grain boundary density and number of triple junctions increases. Grain boundaries and triple junctions are regions of atomic disorder with atoms not fulfilling their usual coordination number. Hence, these atoms have higher reactivity than atoms from inside the grains [2]. The effect of grain size on the corrosion behavior of pure metals in different environments has been studied. The observations are discussed further with a particular focus on iron. A summary of the literature for iron can be found in table 2.1 and table 2.2.

Iron

The effect of grain size on the corrosion of iron has been studied in active [12–15], passive [8, 14, 36], and simulated body fluid (SBF) environment [37, 38]. In most of these studies,

the reduction in grain size of iron is achieved by plastic deformation like rolling and equal channel angular pressing (ECAP). Contradicting results have been published on the effect of grain size in both active and passive conditions. Wang and co-workers [12, 13] studied the corrosion behavior of bulk nanocrystalline iron separately in acidic sulfate (0.05 M H_2SO_4 +0.25 M Na_2SO_4) and 1 M HCl solutions. They noted improved corrosion resistance for the nanocrystalline sample than the conventional polycrystalline ingot sample. This improvement was explained by nobler corrosion potential, lower corrosion current density and higher charge transfer resistance for the nanocrystalline sample. They attributed these results to the strong (110)<111> texture observed in the nanocrystalline sample after the rolling operation. Jinlong et al. [14] studied the effect of cold rolling temperature on the corrosion resistance of pure iron in 0.5 M H_2SO_4 solution. They observed a decrease in cathodic current with a reduction in grain size and no visible effect on the anodic current response. The charge transfer resistance was found to be higher for the cold-rolled sample than the annealed sample. However, XRD analysis showed a decrease in (110) peak intensity and an increase in (200) peak intensity for the cold-rolled sample than the annealed sample. The conclusion of underlying cause in studies of Wang and co-workers do not hold in this study even though all of them report improvement in corrosion resistance with finer grain size. Contradicting to these results, Zhang et al. [15] reported higher polarization resistance for the as-cast pure iron sample than those processed by ECAP in 0.5 M H_2SO_4 solution. Furthermore, the ECAP samples showed higher polarization resistance after annealing treatment.

In passive conditions, corrosion behavior is controlled by the protective properties of the passive film. Yamamoto et al. [8] studied the passivation properties of pure iron subjected to different amounts of rolling reduction in a borate buffer solution (pH=8.4). Compared to the annealed sample, the rolled samples showed higher passivation current density, lower charge transfer resistance, and higher density of defects in the passive film. Further, the passive film was thicker for the cold-rolled sample than the annealed sample. They attributed these observations to the high dislocation density in the rolled sample, which accelerated the film growth but resulted in more defective film. Jinlong et al. [14] also studied the passivation behavior in borate buffer (pH=9.2) with and without chlorine ions. They observed that iron samples rolled at room and cryogenic temperatures provide better passivation properties than the annealed sample in both solutions. The room temperature rolled sample performed better among the rolled samples even though it had slightly larger grain size. This result was ascribed to the higher dislocation density in the cryo-rolled sample. Afshari et al. [36] studied the corrosion behavior of iron in 10 wt.% NaOH solution over a wide range of grain sizes. They observed that corrosion resistance improved as the grain size was reduced. A similar observation was also reported for pure iron in simulated body fluid (Hank's solution) [37].

Table 2.1: Literature summary of effect of grain size on corrosion of iron in active condition.

Processing method	**Grain size range**	**Solution**	**Corrosion resistance (with grain size reduction)**	**Remarks**	**Reference**
Severe hot rolling	38.9 nm to 50 μm	0.05 M H_2SO_4 +0.25 M Na_2SO_4	Increases	Better resistance due to (110)<111> texture.Overlapping effect of texture, residual stress and grain size.	[12]
Severe hot rolling	38.9 nm to 50 μm	1 M HCl	Increases	Better resistance due to (110)<111> texture.Overlapping effect of texture, residual stress and grain size.	[13]
ECAP	250 nm to 450 nm	0.5 M H_2SO_4	Decreases	Annealing treatment helps in improving polarization resistance. Overlapping effect of residual stress and grain size. No analysis of texture in the study.	[15]
Annealed, Cold rolled at room temperature and cryogenic temperature	-	0.5 M H_2SO_4	Increases	Better resistance due to decrease in cathodic reaction kinetics. Overlapping effect of texture, residual stress and grain size.	[14]

Table 2.2: Literature summary of effect of grain size on corrosion of iron in passive condition.

Processing method	Grain size span	Solution	Corrosion resistance (with grain size reduction)	Remarks	Reference
Cold rolling	-	Borate buffer pH=8.4	Decreases	High dislocation density results in thicker but more defective passive film. No analysis of texture.	[8]
Annealed, Cold rolled at room temperature and cryogenic temperature	-	Borate buffer (pH=9.2), Borate buffer with 0.5 M NaCl	Increases	Resistance reduces with increase in dislocation density for fine grain sample.	[14]
Cast, annealed, electro-deposition	45 nm to 300 μm	10 wt.% NaOH	Increases	Finer grains give more nucleation sites for passivation film with better resistance and thickness.	[36]
Rolling followed by annealing	14.1 μm to 168 μm	Hank's solution (pH=7.4)	Increases	Finer grains give more active sites for dense passive film formation.	[37]
As-cast, Laser metal deposition, Selective Laser melting	12 μm to 350 μm	Hank's solution (pH=7.2-7.4)	Decreases	Residual stress and dislocations destabilize passive film locally.	[38]

Other metals

The effect of grain size on corrosion has been studied for other metals as well. For Cu, the corrosion resistance decreased with a decrease in grain size in a 0.1 M HCl solution [11]. This was attributed to an increase in grain boundary density, which provides more active sites for corrosion. However, the fine grain samples showed uniform corrosion, while the coarse-grained samples exhibited preferential dissolution at the grain boundaries. Similar observations were also seen in other studies of pure copper [39, 40]. In the alkaline environment, the decrease in grain size by cold rolling resulted in better passivation properties of the film. This was ascribed to the higher activity of atoms in grain boundaries, which result in the rapid formation of the passive layer [41]. Studies on Ti reported an improvement in corrosion resistance with a decrease in grain size [42, 43]. The finer grain size provides more nucleation sites for easier formation of the passive film. However, the studies on Ti do not comment on the role of texture. In the case of Ni, the reduction in grain size decreased the corrosion resistance in 2 N H_2SO_4 [44]. The fine-grained sample improved the kinetics of cathodic reduction of hydrogen and also had higher passivation current density than the coarse-grained sample. On the contrary, cold-rolled Ni exhibited better passivation properties than the annealed Ni sample in the borate buffer solution [45]. Similar improvements in passivation properties have been noted for Mg [46] and Al [9] as well.

From the studies so far in the active and passive conditions, it is clear that factors like texture and residual stress affect the corrosion behavior of metals. In several instances, they have emerged as the dominant features [12–15]. Hence, these factors need to be considered while relating grain size with corrosion resistance. Most of the studies miss out on this aspect. Hence, understanding the role of grain size in the corrosion behavior of metal becomes difficult. Ralston et al. [47] made the first attempt to propose a general relation between corrosion rate and grain size by summarizing the corrosion studies on different metals and alloys. The relationship can be expressed as:

$$i_{corr} = A + B * d^{-0.5} \tag{2.7}$$

In this equation, i_{corr} is the corrosion current density, d is the grain size, A is a constant dependent on the corrosion medium, and B is a material constant depending on the composition or impurity level. Fig. 2.4 shows the corrosion current density as a function of grain size from different studies. A distinction between active and passive behavior is made at 10 μA/cm^2. Using grain boundary length as the deciding factor, they proposed that corrosion rate increases with a decrease in grain size in active condition and decreases with a decrease in grain size in passive condition. This behavior is illustrated schematically in fig. 2.5 in the form of polarization curves. The factor 0.5 in the equation 2.7 comes from the simulations, which showed that the grain boundary length is related to grain size as $d^{-0.5}$ for random microstructure [47]. The relation is useful in understanding the effect of environment and impurity or composition on the corrosion behavior of metals.

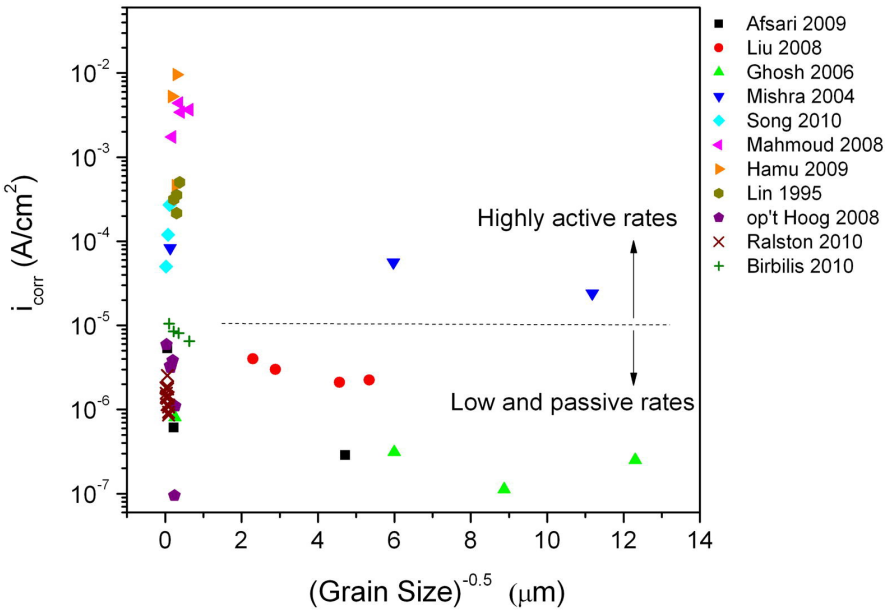

Figure 2.4: Effect of grain size on corrosion rate for different materials in different environments compiled by Ralston et al. [47].

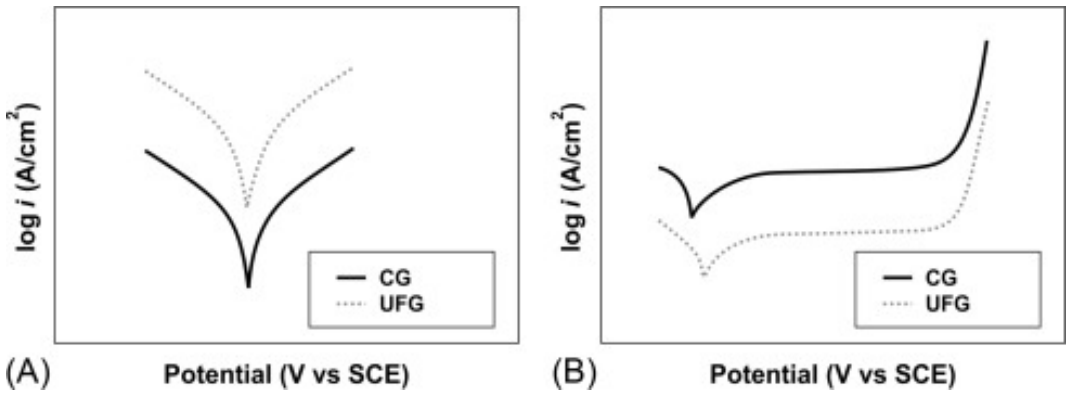

Figure 2.5: Schematic representation of the effect of grain size on corrosion behavior in (A) active and (B) passive condition (CG - coarse grain, UFG - ultra-fine grain) [48].

Gollapudi [49] tried to extend the relation by including the effect of grain size distribution. The proposed relation can be expressed as:

$$i_{corr} = A + B * d^{-0.5} exp\left(-\frac{9}{8}S_n^2\right) \tag{2.8}$$

In this equation, S_n is the standard deviation of the number weighted grain size distribution. S_n varies between 0 and 1. In physical terms, S_n = 0 signifies every grain has the same size. S_n usually lies in the 0.3 - 0.5 range. This relation is proposed for pure metals under uniform corrosion. As per the relation, for a given average grain size, a narrow grain size distribution results in better corrosion resistance in passive condition than a broad grain size distribution. Narrow grain size distribution results in compact and homogeneous passive layer formation due to the uniform distribution of active sites (grain boundaries and triple junctions). But in active condition, broad grain size distribution results in better corrosion resistance due to lower grain boundary volume associated with coarse grains [49]. This explanation is shown schematically in fig. 2.6.

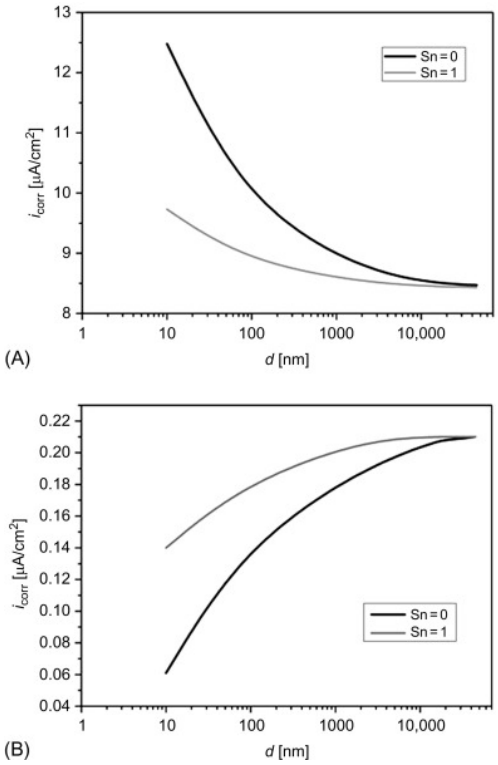

Figure 2.6: Schematic representation of the effect of grain size distribution on corrosion rate in (A) active and (B) passive conditions [48].

2.3.2. Texture

Texture is a characteristic feature in the microstructure of metals. Crystallographic texture refers to the preferential orientation of grains in a specific direction. Most of the metals and alloys for structural applications are polycrystalline in nature. During processing by plastic deformation, the atoms accommodate strain by slip and twinning. This process re-orients the grains resulting in the emergence of texture. Texture can also be induced by phase transformation and recrystallization [50]. In the present context, texture plays a vital role in the corrosion behavior. Atoms along specific crystallographic planes are more densely packed than others. As a result, a variation in the reactivity of atoms on different planes arises facing the corrosion medium [2]. Corrosion studies using micro-electrochemical techniques have been performed in active and passive conditions on metals. The findings are discussed next with a special focus on iron. A summary of the literature for iron can be found in table 2.3.

Iron

The role of texture in the corrosion behavior of iron is evident from the earlier discussion of studies of Wang et al. [12, 13]. Fushimi et al. [51] studied the grain dependent dissolution of iron in 0.05 M H_2SO_4. They observed the corrosion resistance to following the order of (110) > (111) > (001). The corrosion activity was found to be governed by the cathodic hydrogen evolution reaction. They credited their observation to the decomposed d-valence charge at the surface of different crystal planes, which also followed the same sequence. Schreiber et al. [52] studied the anisotropic dissolution of iron by different polishing techniques. Atomic force microscopy (AFM) showed the formation of steps in grain boundaries between dissimilar orientations due to the difference in dissolution rates. After electropolishing, neighboring grains of (001) orientation formed walls at grain boundaries, while trenches are observed in grain boundaries between grains of the same orientation after chemical polishing. This is shown in

fig. 2.7. Fushimi et al. [53] studied the passivation behavior of different crystal orientations in borate buffer (pH = 8.4) using scanning electrochemical microscopy (SECM). Using $Fe(CN)_6^{4-}$ as the mediator, the probe current on (001) plane was found to be lower than (111) and (101) planes. The lower current on (001) plane was attributed to the formation of a thicker passive film. In another study, Fushimi et al. [54] studied the local breakdown of the passive layer by chloride ions using liquid phase ion gun. The induction time for breakdown followed the sequence (001) > (111) > (110). This shows better passivation properties of the film formed on (001) plane. A similar sequence was also reported by Davenport et al. [32] based on less defectivity of the passive film on (001) orientation. Takabatake et al. [55] studied the grain dependent passivation properties of iron in 0.05 M H_2SO_4. The resistance of passivation film followed (110) > (111) > (001). They ascribed this observation to the composition of the film rather than the thickness. Based on the duplex layer model of the passive film, a thicker Fe_2O_3 layer provides better corrosion resistance for the same overall thickness of the passive film. They observed the Fe^{3+}/Fe^{2+} ratio to follow the same sequence on different planes in XPS analysis.

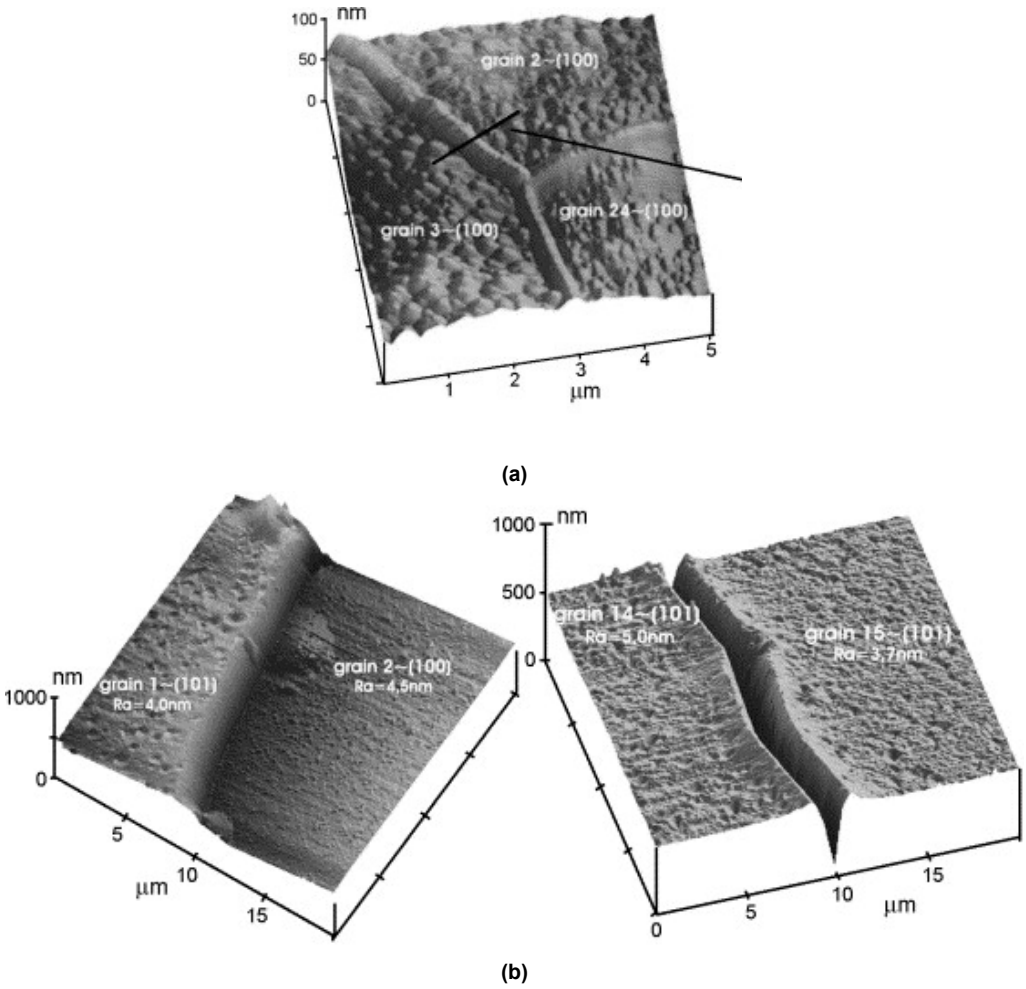

Figure 2.7: AFM images showing the formation of (a) walls in grain boundaries after electropolishing, (b) steps and trenches in grain boundaries after chemical polishing [52].

Table 2.3: Literature summary of corrosion activity of iron on different crystal planes.

Property	Solution	Sequence	Reference
Dissolution rate	0.05 M H_2SO_4 (pH=1)	(001) >(111) >(110)	[51]
Dissolution rate	Acetate buffer (pH=6)	(111),(110) >(001)	[56]
Passive film quality	Borate buffer (pH=8.4)	(001) >(110),(111)	[53]
Passive film quality	Borate buffer (pH=8.4)	(001) >(110)	[32]
Passive film quality	Borate solution (pH=6.5)	(001) >(111),(110)	[54]
Passive film quality	0.05 M H_2SO_4	(110) >(111) >(001)	[55]

Other metals

The grain dependent corrosion behavior is also witnessed for other metals. In the case of rolled copper, Lombardia et al. [57, 58] found that grains oriented close to <111>// ND showed higher corrosion activity than those along <001>// ND direction in active condition. They also observed the corrosion activity of grains along <001>// ND to depend on the orientation of neighboring grains. This is due to the formation of the anode-cathode couple between neighboring grains with a large difference in electrochemical potential [59]. In the passive state, they observed a stable and thicker passive layer on grains oriented close to <111>// ND than <001>// ND [58]. Wang et al. [60] studied the grain dependent corrosion behavior of pure Al in 3.5 wt.% NaCl solution. The corrosion resistance followed the sequence (001) > (110) > (111). They ascribed the result to the bonding electron density on different crystal planes, which plays an important role in accelerating the cathodic reaction. Hoseini et al. [61] compared the effect of texture and grain size on the corrosion of Ti in 0.16 M NaCl solution. They report texture to have a more dominant effect than grain size. They attributed close-packed (0002) orientation parallel to the surface for high corrosion resistance. Besides grain orientation, the effect of grain boundary type has also been studied. For Cu, Bettayeb et al. [62] found high angle grain boundaries (HAGBs) to be more susceptible to intergranular corrosion than low angle grain boundaries (LAGBs) and special grain boundaries like coincidence site lattice (CSL). Slight angular deviation (> 1.70°) from perfect $\Sigma 3$ CSL twin boundary also renders them susceptible to corrosion attack. Orlowska et al. [63] also found pitting corrosion to occur preferentially along HAGBs in pure Al. HAGBs have higher energy than LAGBs and CSL boundaries. Hence, the fraction of HAGBs in the microstructure needs to be accounted for while assessing the corrosion behavior of metals.

2.3.3. Residual stress

Residual stress is the stress that exists in a material after the removal of externally applied forces. During plastic deformation, the strain imparted on the metal creates lattice defects

that increase the internal energy. This extra accumulated strain energy results in residual stress. Residual stress can affect the corrosion behavior of metal. In active condition, the presence of residual stress increases the corrosion susceptibility due to the higher activity of atoms [2]. However, in passive condition, the effect is more complicated because the corrosion resistance depends on the quality of the passive film formed. In the case of Cu [41], Ni [45], and Ti [43], the corrosion resistance improved with the amount of plastic deformation in the passive condition. The improved passivity was attributed to the rapid formation of a passive film with low defect density. But, in the case of Fe, plastic deformation resulted in a passive film with more defects [8, 38]. Nevertheless, these studies do not analyze passivity behavior over a long time period. Bagherifard et al. observed a decrease in resistance of passive film with time for shot-peened Fe sample due to breakdown and separation of the protective layer [64]. The use of annealing step to reduce the residual stress can be beneficial in active condition, but in passive condition, it depends on the material's response.

2.3.4. Segregation of impurities

The presence of impurities in pure metals is a common phenomenon. Thermal processing steps can promote the segregation of impurities and affect the corrosion behavior of metals [2]. Bolyanov et al. [42] reported better passive film formation in fine-grained Ti than coarse-grained Ti. They attributed the segregation of impurities along grain boundaries to affect the passive film formation in the coarse grain Ti sample. For a fixed concentration of impurities, a sample with finer grains has more impurity-free grain boundaries than a coarse grain sample. Mercier et al. [65] studied the role of segregated Fe impurities along grain boundaries on the corrosion of Mg. The presence of Fe along grain boundaries enhanced Mg corrosion by acting as cathodic sites for cathodic hydrogen evolution reaction. Preferential attack on grain boundaries has been reported for Co with S as impurity [66]. The presence of S as impurity has been reported to interfere with the formation of passive films in Ni [67]. Hence, it is necessary to acknowledge the amount and distribution of impurities in the sample during the corrosion study.

2.4. Corrosion modeling

Modeling of the corrosion process forms an essential part of the corrosion studies. The broad purpose of corrosion modeling is to assess and predict corrosion-related damage to structures. This aids in the effective utilization of resources. However, corrosion is a complex phenomenon. It is a multi-physics problem involving interaction between electrochemistry, metallurgy, fluid flow, and stress, to name a few. Further, each of these phenomena operates at different time and length scales. Hence, researchers model the corrosion problem at different scales. The integration of these models gives a complete understanding of the corrosion problem. The approach in corrosion modeling can be empirical or deterministic, depending on the nature of the problem. Further, uncertainty in corrosion models can exist due to an incomplete understanding of mechanism or lack of data. Hence, the reliability of models should be validated by comparing with experimental data [68–70]. Some examples of corrosion modeling in literature are summarized in table 2.4. In the following subsection, numerical modeling of corrosion is discussed in detail.

Table 2.4: Literature summary of some corrosion models.(FEM: finite element modeling, IGSCC: intergranular stress corrosion cracking, RE: rare-earth)

Model Type	Purpose	Input	Output	Reference
Numerical model (FEM)	Effect of corrosion product layer on the corrosion rate evolution with time.	Governing equations and parameters from experiments	Mass loss with time, pH evolution with time	[71]
Semi-empirical model	To model corrosion system implicitly with corrosion products.	Governing equations and parameters from experiments	Physical relation	[72]
Monte-Carlo simulation	Effect of microstructure on crack propagation in IGSCC	Simulation parameters and experimental data	Crack propagation, percolation frequency	[73]
Mathematical model	Effect of amount and type of RE element on corrosion of Mg alloys	Experimental data	Mathematical relation	[74]
Cellular automata	Modelling intergranular corrosion	Relative probability of corrosion of grains and grain boundaries	crack length evolution with time	[75]
Analytical model	Effect of grain size and second phases on corrosion	Experimental data	Physical relation	[76]
Numerical model (FEM)	Micro-galvanic corrosion	Governing equations and parameters from experiments	Evolution of corrosion front and current density distribution	[77]
Cellular automata	Simulating pit shape evolution	Relative local corrosion probability	Pit shapes	[78]
Numerical model (FEM)	Effect of texture on pit growth and shape	Governing equations and parameters from experiments	Pit depth, pit shape, ion concentration evolution with time	[79]

2.4.1. Numerical modeling of corrosion

Numerical modeling based on finite element analysis is a convenient method for modeling different corrosion phenomena. It involves discretization of the system under study by meshing. The governing physical equations are solved at nodes of each mesh element to generate solutions over the entire system. The improvement in computational power has eased finite element modeling of corrosion in complex geometries [80]. Several notable research works on numerical modeling of corrosion can be found in the literature. Deshpande [81] developed a numerical model of the galvanic corrosion. The model predicts the corrosion rate of the in-

dividual constituents in the galvanic couple by tracking the moving electrochemical interface. The observations of the model are verified by conducting scanning vibrating electrode technique (SVET) experiments and surface profile analysis. In another work by the same author, the model is implemented to study micro-galvanic corrosion of AM50 Mg alloy [77]. The model successfully incorporated the effect of phase fraction and phase distribution on the corrosion behavior. Sun et al. [82] developed a numerical model to study the evolution of crevice corrosion in stainless steel with time. The model is validated by pH distribution in the crevice, crevice shape evolution, and deposition of corrosion products. Brewick et al. [79] studied the microstructure dependent growth of pits after initiation in their numerical model and found irregular stress distributions in the corrosion pits depending on their geometry [83]. As stated earlier, the model solves equations that govern the physics of the system. For corrosion modeling, these equations are discussed below.

Governing equations

Corrosion can be expressed in the form of an electrochemical system. It consists of electrode and electrolyte. The corroding metal, acting as the electrode, conducts current through the movement of electrons. The corroding environment, acting as the electrolyte, conducts current by the movement of charged species (ions). The conductivity of the electrode is usually several orders of magnitude higher than that of the electrolyte [80].

In the model, the values of electric potential and current density are solved in the electrode and electrolyte domains. In the electrode, the relation is given by the vector form of Ohm's law (equation 2.9). In this equation, i_s is the electrode current density vector, σ_s is the electrode conductivity, and ϕ_s is the electrode potential. In the case of electrolyte, the current density vector (i_l) is related to the flux of the charged species i (N_i) by equation 2.10. Here, F is the Faraday's constant and z_i is the charge of species i. The flux of charged species in the electrolyte is given by the Nernst-Planck equation (equation 2.11). In the equation, D_i is the diffusion coefficient of species i, c_i is the concentration of the species i, u_i is the mobility of species i, ϕ_l is the electrolyte potential and U is the velocity of electrolyte. The equation from left to right depicts the contribution of diffusion, migration, and convection to the flux of species, respectively. The equation ignores the interaction between ions. Combining equations 2.10 and 2.11, the electrolyte current density vector can be rewritten, as shown in equation 2.12 [80].

$$i_s = -\sigma_s \nabla(\phi_s) \tag{2.9}$$

$$i_l = F \sum_i z_i N_i \tag{2.10}$$

$$N_i = -D_i \nabla c_i - z_i u_i F c_i \nabla \phi_l + c_i U \tag{2.11}$$

$$i_l = -F \left(\nabla \sum_i D_i c_i z_i \right) - F^2 \nabla \phi_l \sum_i z^2{}_i u_i c_i + UF \sum_i z_i c_i \tag{2.12}$$

The equation 2.12 can be simplified by making suitable assumptions. In the current modeling work, the electrolyte is assumed to be incompressible, electro-neutral, well-mixed (i.e. no concentration gradient in the electrolyte) and has constant electrical conductivity. As a result, the contributions of flux from diffusion and convection can be neglected. This simplification results in a linear relationship between the current density and potential gradient similar

to Ohm's law (equation 2.13). The electrolyte conductivity (σ_l) accommodates the other parameters of the migration term. The electroneutrality condition implies that the total charge of the electrolyte to be zero. This condition requires the divergence of the electrolyte potential gradient to be zero (equation 2.14) [77].

$$i_l = -\sigma_l \nabla(\phi_l) \tag{2.13}$$

$$\nabla^2 \phi_l = 0 \tag{2.14}$$

For the conservation of current, the electrochemical interface also needs to be taken into consideration. Current flows across electrode-electrolyte interface through electrochemical reactions. The electrochemical reaction kinetics is given by the Tafel equation (equation 2.15),which is used in the current work. Here, i_0 is the exchange current density, β is the Tafel slope and η is the overpotential defined by equation 2.16. E and E_{eq} are the applied potential and equilibrium potential, respectively [80].

$$\eta = \beta * log\left(\frac{i}{i_0}\right) \tag{2.15}$$

$$\eta = \phi_s - \phi_l - E_{eq} \tag{2.16}$$

3

Materials and Methods

This chapter outlines the materials used, and the methods followed to perform the experimental and modeling studies. The material processing, microstructure characterization, electrochemical characterization,surface characterization and the numerical modeling are presented sequentially in sections to answer the proposed research question.

3.1. Material processing

3.1.1. Material

A cold-rolled sheet of Armco iron (supplied by AK Steel, Netherlands) is used in the present work. The sheet, with a thickness of 2 mm, is laser-cut to obtain samples of length 10 mm and width 5 mm. The chemical analysis of the sample is performed by wavelength dispersive spectroscopy using a JEOL JXA 8900R microprobe with an electron beam energy of 10 keV and a beam current of 100 nA. Following background correction, the measured X-ray intensities of constituent elements are compared to those of a reference standard to estimate the chemical composition. The obtained composition is summarized in table 3.1. The sample has Fe purity exceeding 99.5%.

Table 3.1: Elemental composition of iron samples

	Fe	C	N	Si	Mn	P	S	Al	Cr	Cu	Mo	Ni	Sn
wt.%	Bal.	0.001	0.003	0.003	0.04	0.003	0.003	0.004	0.014	0.007	0.001	0.012	0.002

3.1.2. Microstructure design

The as-received iron samples are heat-treated using a Bähr DIL 805 A/D dilatometer to obtain different grain sizes. The samples are heated to the annealing temperature at a rate of 10 °C/s under approximately 10^{-20} bar vacuum. The annealing duration is 10 minutes for every sample. After annealing, the samples are quenched to the room temperature using helium gas flow. The annealing temperatures selected in the present study are 700 °C, 950 °C, and 1100 °C. The corresponding heat treatment cycles are labeled Fe-700, Fe-950, and Fe-1100, respectively, in the schematic fig. 3.1 and hereafter used as sample names.

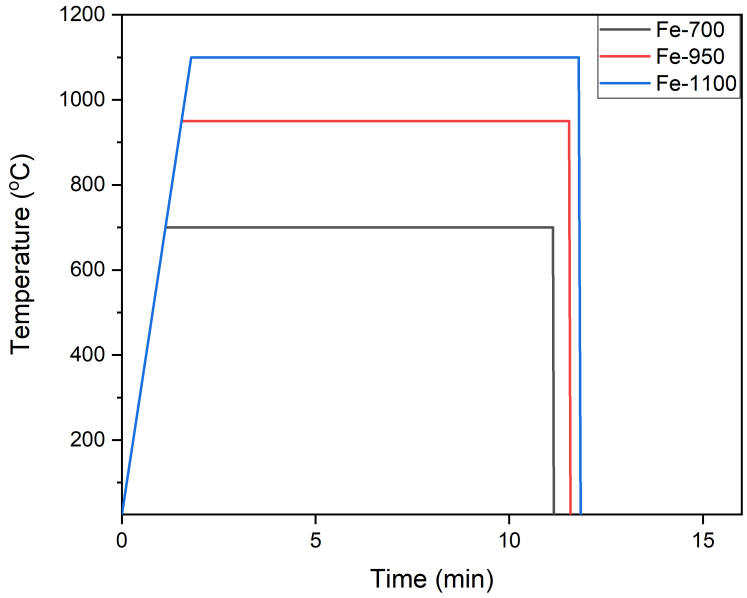

Figure 3.1: Illustration of the heat treatment cycles used to obtain samples with different grain sizes.

3.2. Microstructure characterization

3.2.1. Sample preparation

The heat-treated iron samples undergo sample preparation steps before microstructure characterization. The samples are embedded in epoxy resin (Struers ClaroCit) and cured at room temperature and under 2 bar pressure for one hour. The samples embedded in epoxy resin undergo sanding sequentially from P80 to P4000 grit SiC paper. This step is followed by polishing with alcohol based diamond particle suspension (Struers DiaDuo-2) of particle size 3 µm and 1 µm to obtain a mirror-like finish. The samples are then cleaned with isopropanol in an ultrasonic bath for 10 minutes and dried with airflow.

3.2.2. Optical microscopy

The microstructure of the heat-treated samples is studied using the Keyence VHX-5000 digital microscope. The samples are etched with a 2% Nital solution to reveal the microstructure. The samples are also examined under the microscope after electrochemical tests. The images from optical microscopy are used to calculate the grain size and observe the nature of corrosion attack in different samples. The average grain size calculation is done by using the line intercept method on three images for each sample.

3.2.3. EBSD

Electron backscatter diffraction is performed on the samples to extract their microstructural information such as grain size, grain boundary fraction, the fraction of high-angle and low-angle grain boundaries, and geometrically necessary dislocation (GND) density. The samples undergo sanding and polishing, as discussed in section 3.2.1. An additional step of OPS polishing is done before ultrasonic cleaning. The measurements are conducted using a JEOL JSM 6500F FEG-SEM microscope with an EDAX/TSL detector. The step size and working distance are 1 µm and 17 µm, respectively. The scan is performed over an area of 1.44 mm^2 in each sample. The data processing and analysis are done using TSL-OIM v7.3 software and

MATLAB® with the MTEX toolbox [84–88]. The grain identification is done using a threshold misorientation angle of 5°. The grain boundaries are classified as low-angle and high-angle grain boundaries using a threshold misorientation angle of 15°.

3.2.4. XRD

The macro-texture analysis is performed on the polished sample surface using Bruker D8 Discover X-ray diffractometer with Eulerian cradle and parallel beam geometry. The X-ray radiation used is Co Kα (λ= 0.179 nm) with an accelerating voltage 45 kV and a current of 25 mA. The measurements are performed on the normal plane of the samples consisting of the rolling direction and transverse direction. Data processing and analysis are done using Bruker software Texture Edit, Texture Evaluation, and DiffracSuite EVA 5.2. Fig. 3.2 illustrates the placement of samples in the diffractometer.

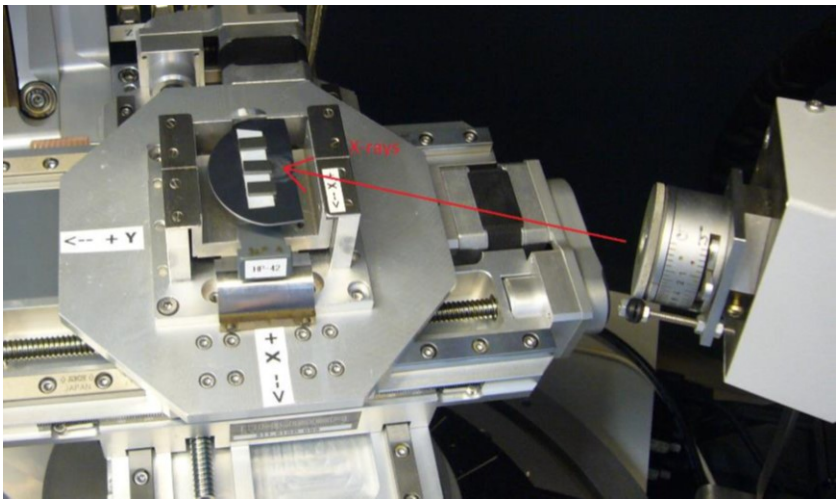

Figure 3.2: Illustration showing the samples inside the diffractometer with the direction of X-rays

3.3. Electrochemical characterization

3.3.1. Theory

Several electrochemical techniques exist that can provide useful information about the corrosion behavior of metals. It is common in corrosion studies to use multiple characterization methods for a better understanding of the corrosion process [17, 18]. The theory and principle of two important techniques: potentiodynamic polarization (PDP) and electrochemical impedance spectroscopy (EIS) are explained further in detail.

Potentiodynamic polarization (PDP)

PDP is an electrochemical technique in which the response (current) of the system is recorded by sweeping linearly over a selected range of potential. The experimental set-up consists of a 3-electrode electrochemical cell connected to a potentiostat. A potentiostat is a device that can be used to control the potential or current through a cell and measure the other corresponding signal. Fig. 3.3 shows the 3-electrode cell. It consists of a working electrode, counter electrode, and the reference electrode in the electrolyte. It can also have special connection for gas inlet and outlet. The material under examination is the working electrode. In corrosion studies, the corrosion behavior of the working electrode is studied. The reference electrode has a constant potential and serves as a reference for measuring the potential of the working electrode. The counter electrode completes the cell circuit. It is usually made of an inert material like platinum or graphite. Once the cell is assembled, it is allowed to attain a stable

open circuit potential (OCP) before performing experiments. During this period, no current flows in the circuit. As the oxidation and reduction reactions on the electrode surface reach equilibrium, the OCP becomes stable [17, 18].

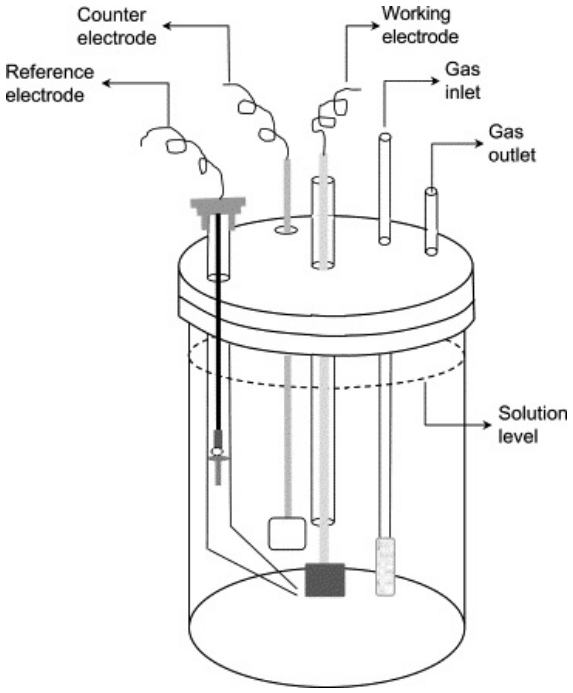

Figure 3.3: Schematic diagram of a 3-electrode electrochemical cell [18]

In PDP, the potential range of interest is defined first. The sweep begins in the positive direction from the lowest potential. The scanning rate is kept small to maintain steady-state like conditions. A potential (E)-current (I) plot is generated during the scan. The current is usually normalized with the area of the working electrode to get current density (i). The current density is plotted in logarithmic scale as it can spread over orders of magnitude. This graph can be used to determine parameters like corrosion current density (i_{corr}), corrosion potential (E_{corr}) and resistance polarization (R_P), which quantify the corrosion behavior of the material under study [17, 18]. From the fundamentals of electrochemistry, the concept of polarization is well-known. Polarization refers to the deviation of potential from its equilibrium potential due to a net surface reaction resulting in current flow. It has been categorized into three types: activation polarization, concentration polarization, and ohmic polarization. Activation polarization arises due to a rate-limiting step controlling the half-cell reaction. Concentration polarization arises due to the limiting effect of mass-transfer of species in the vicinity of the electrode surface. Ohmic polarization, as the name suggests, is the potential drop associated with ohmic resistance of the solution and surface films. The change in potential due to polarization is quantified by the overpotential (η). If the overpotential is positive, it is called anodic polarization and if it is negative, it is called cathodic polarization [17]. The general relationship between current density and overpotential is given by the equation 3.1. In this equation, i_0 is the exchange current density, α is the anodic charge transfer coefficient, $C_O(0,t)$ and C_O^* are the concentration of oxidized species at the surface and bulk level. Similarly, $C_R(0,t)$ and C_R^* are the concentration of reduced species at the surface and bulk level. f stands for nF/RT where n is the number of electrons involved in the reaction, F is Faraday's constant, R is the universal gas constant and T is the absolute temperature. On simplifying the equation by assuming a well-stirred solution with no mass-transfer effects, we get the familiar Butler-Volmer

equation (equation 3.2) [17, 89].

$$i = i_0 \left[\frac{C_O(0,t)}{C_O^*} e^{-\alpha f \eta} - \frac{C_R(0,t)}{C_R^*} e^{(1-\alpha) f \eta} \right] \tag{3.1}$$

$$i = i_0 (e^{-\alpha f \eta} - e^{(1-\alpha) f \eta}) \tag{3.2}$$

At large overpotential (η > 118 mV), the equation gives the Tafel behavior. The value of 118 mV comes from the consideration that the back reaction contributes less than 1% of the current [89]. If the plot obtained by PDP contains linear regions in the cathodic and anodic sweep over a decade of current, they can be extrapolated towards the corrosion potential to intersect to give the corrosion current density. A schematic of this extrapolation procedure is shown in fig. 3.4. The corrosion rate (r) in thickness per unit time can be calculated from the current density using the equation 3.3. Here, a is the molar mass of the corroding metal, n is the number of electrons involved, F is Faraday's constant and D is the mass density of the corroding metal [17, 18, 89].

$$r = \frac{ia}{nFD} \tag{3.3}$$

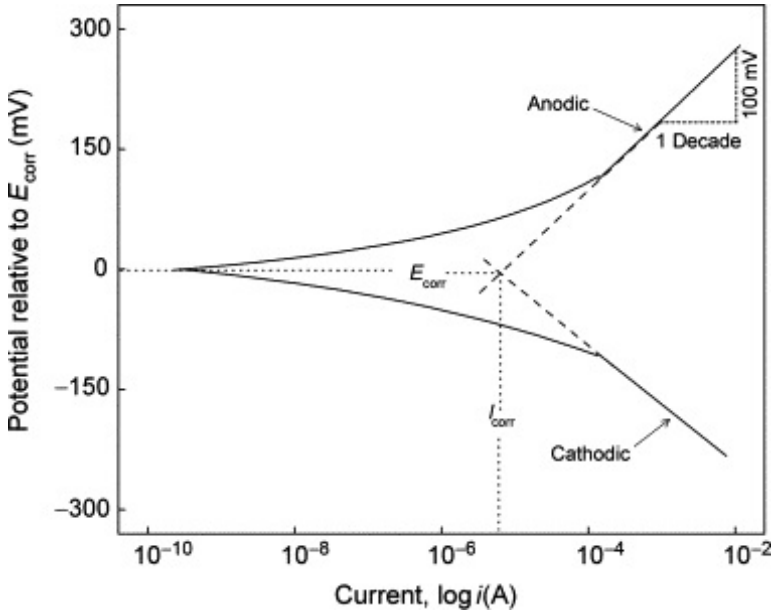

Figure 3.4: Determination of corrosion current density by Tafel extrapolation [18]

At low overpotential (10-20 mV), the Butler-Volmer equation simplifies to a linear relation between overpotential and current density. The slope of the curve plotted in linear scale gives the polarization resistance (as shown in the fig. 3.5). The Stern-Geary equation gives the inverse relation between the corrosion current density and the polarization resistance (equation 3.4). Here, b_a and b_c are the anodic and cathodic Tafel slopes, respectively. A material with high corrosion resistance has low i_{corr} and high R_P value [17, 89].

$$i_{corr} = \frac{1}{2.303 R_P \left(\frac{1}{b_a} + \frac{1}{|b_c|} \right)} \tag{3.4}$$

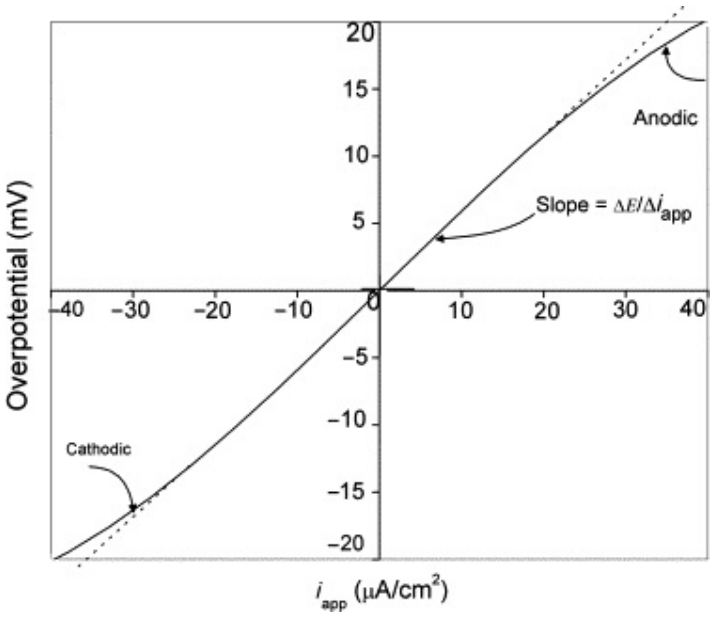

Figure 3.5: Determination of polarization resistance [18].

Electrochemical impedance spectroscopy

EIS is a non-destructive technique to understand the complex phenomena occurring at the electrode-electrolyte interface. The method involves applying a small perturbation of voltage or current periodically and recording the response of the system. Generally, an amplitude of a 10-20 mV AC signal is applied to the system and the current response is recorded. The perturbation displaces the system from its present state, followed by relaxation to a new steady state. The relaxation process of the system is studied over a wide range of frequencies of the excitation signal (10^{-2} to 10^{5} Hz). The experimental set-up consists of a 3-electrode cell, a frequency generator, a frequency response analyzer, and a potentiostat for controlling the potential of the working electrode. The AC potential and current are sinusoidal and can be expressed at any instant in time (t) by equations 3.5 and 3.6, respectively. Here, V_0 and I_0 are the amplitudes of voltage and current, ω is the angular frequency, and ϕ is the phase difference between the voltage and current. These voltage and current can be represented in complex form using Euler's equation (equation 3.7) They are shown in equations 3.8 - 3.9. The impedance of the system $Z(\omega)$, given by Ohm's law in the complex form, is presented by the equation 3.10. Z_0 is the magnitude of impedance. The impedance consists of a real part and an imaginary part [17, 18, 90].

$$V(\omega, t) = V_0(cos(\omega t)) \tag{3.5}$$

$$I(\omega, t) = I_0(cos(\omega t - \phi)) \tag{3.6}$$

$$e^{j\theta} = cos(\theta) + jsin(\theta) \tag{3.7}$$

$$V(\omega, t) = V_0 e^{j\omega t} \tag{3.8}$$

$$I(\omega, t) = I_0 e^{j(\omega t - \phi)} \tag{3.9}$$

$$Z(\omega) = \frac{V(\omega, t)}{I(\omega, t)} = Z_0(cos(\phi) + jsin(\phi)) \tag{3.10}$$

EIS data processing is done by representing the impedance measured in terms of an equivalent electrical circuit. This representation helps in simplifying the corrosion process occurring at the interface. A typical representation of the metal-solution interface as electrical circuit

is shown in fig. 3.6. Here R_Ω is the solution resistance, R_P is the polarization resistance or charge-transfer resistance, and C_{dl} is the capacitance associated with the electrical double-layer. The impedance measurements performed by the software can be represented by two plots. They are the Nyquist plot (also known as complex-plane plot or Cole-Cole plot) and the Bode plot. In the Nyquist plot (fig. 3.7), the imaginary part of impedance (Z'') is plotted against the real part (Z') for every frequency. The frequency increases along the direction shown. The length of the line drawn from origin to the graph gives the magnitude of impedance for the specific frequency. The angle θ is the phase difference described earlier. The graph has a semi-circular shape and intersects the x-axis at two points. From the calculations, the intersection at the low-frequency end ($\omega \to 0$) gives the sum of polarization resistance and solution resistance. At the high-frequency end ($\omega \to \infty$), the intersection gives the solution resistance. The frequency corresponding to the maxima of the graph is equal to the inverse of time constant of the parallel R-C circuit. The Bode-plot (fig. 3.8) expresses the magnitude of impedance as a function of the frequency. It can also include the dependence of phase angle with frequency. The capacitance C_{dl} can be calculated by extrapolating the linear portion of the plot to the y-axis, as shown in the fig. 3.8 [17, 18].

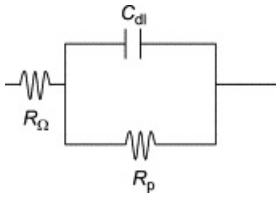

Figure 3.6: A typical equivalent electrical circuit of electrochemical interface [18]

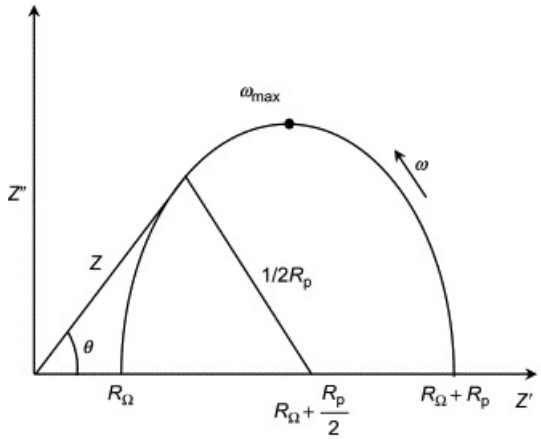

Figure 3.7: Representation of Nyquist plot

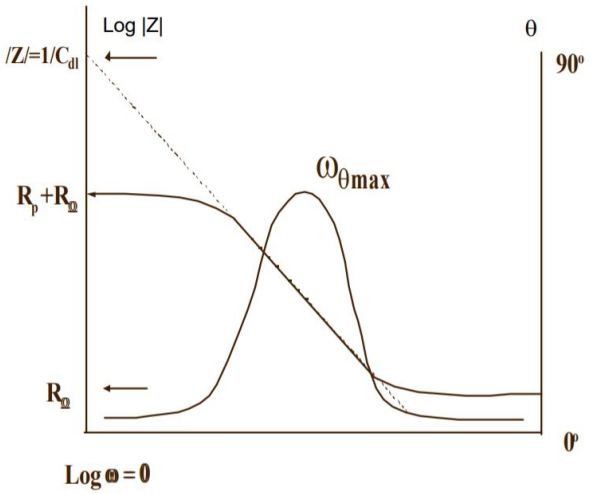

Figure 3.8: Representation of Bode plot [91]

In the present work, EIS is used to understand the metal-solution interface and develop an equivalent electrical circuit. The values of the elements in the circuit are used to compare the corrosion resistance of samples with different grain sizes. In active condition, the charge-transfer resistance of the system is the indicator of the corrosion resistance of the metal. In passive condition, the capacitance of the passive film gives a rough estimate of the film thickness [18, 90].

3.3.2. Experimental set-up

The electrochemical experiments on each sample are performed using a BioLogic VSP-300 potentiostat. The sample surface is prepared by grinding and polishing, as discussed in section 3.2.1. The sample is coated along the edges with a BLR Electrolube sealant (fig. 3.9) to prevent crevice corrosion. A piece of adhesive copper tape is stuck on the rear-end of the exposed metallic surface for convenient electrical connection. The sample is now mounted in a custom 3-electrode cell set-up. In this cell, the sample acts as the working electrode, stainless-steel mesh acts as the counter electrode, and Ag/AgCl electrode filled with saturated KCl acts as the reference electrode. The set-up is placed in Faraday cage to avoid to avoid interference from external electromagnetic fields. This is shown in fig. 3.10. The experiments are performed in deaerated 0.1 M H_2SO_4 and 0.01 M H_2SO_4 solutions. The preparation of these solutions is discussed in Appendix A1. The deaeration step is carried out by purging N_2 gas through 100 ml of the solution for one hour. The beaker containing the solution is sealed with Parafilm M laboratory film during deaeration to avoid exposure to open air as much as possible (fig. 3.11).

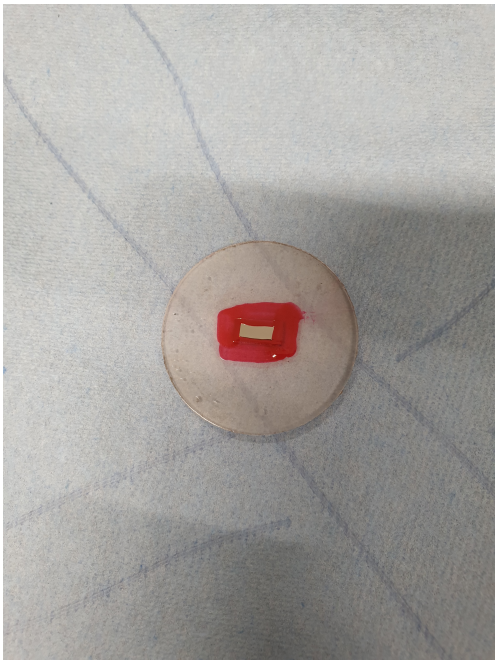

Figure 3.9: Polished sample with the sealant applied before the experiment.

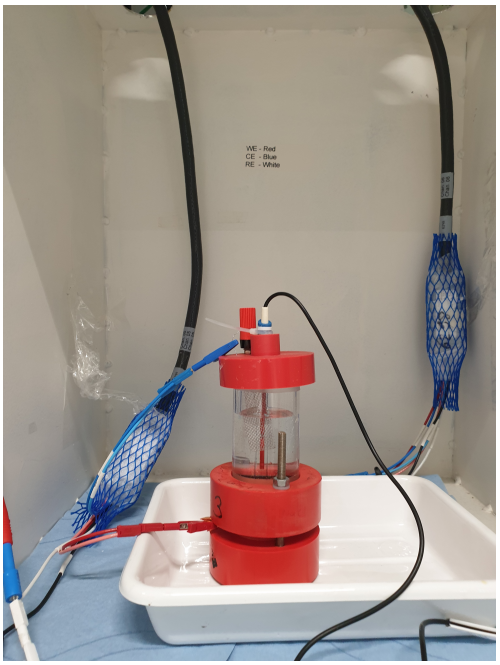

Figure 3.10: Illustration showing the custom 3-electrode cell set-up in a Faraday cage used to perform the electrochemical experiments.

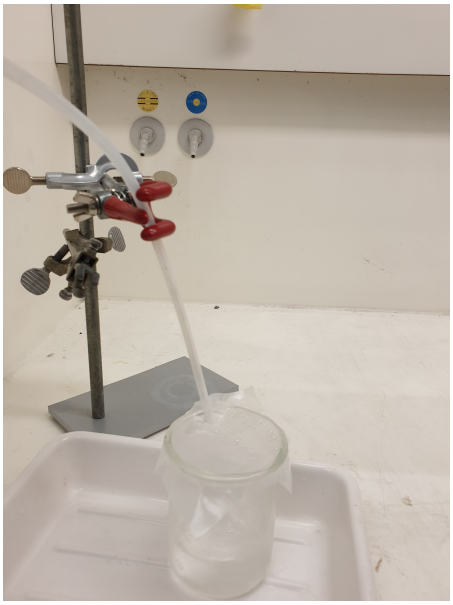

Figure 3.11: Illustration of the deaeration step of the corrosion medium before experiment.

3.3.3. Potentiodynamic polarization

Following the set-up, system is allowed to stabilize for one hour at room temperature to obtain a steady open circuit potential (OCP). The measurement is then performed in the potential range of -250 mV to +250 mV with respect to the OCP. The scan rate is 0.167 mV/s.

The exposed surface area of the sample is measured using a Keyence VHX-5000 digital microscope after the test is completed. An illustrative area measurement image is shown in fig. 3.12. The polarization experiment of the sample is repeated at least 3 times in each environment to ensure the reproducibility of the results. The data collection and analysis is done using EC-Lab v11.34 software. The polarization data is used to determine the electrochemical parameters by the Tafel extrapolation method. The linear fitting of the cathodic branch is done around -50 mV to -150 mV from the equilibrium potential. For the anodic branch, the linear fitting is performed around +30 to +50 mV from the equilibrium potential.

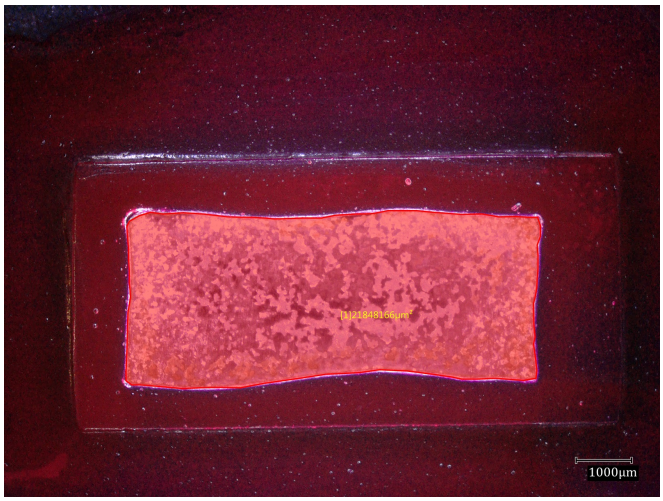

Figure 3.12: Optical image illustrating the measurement of the exposed area of the sample.

3.3.4. Electrochemical Impedance Spectroscopy

Electrochemical impedance spectroscopy (EIS) is performed on the samples to understand the electrode-electrolyte interface and complement the corrosion behavior results of samples from polarization tests. The system is first allowed to stabilize for 1 hour at room temperature before the experiment to obtain a steady open-circuit potential. The measurement is performed in sine mode using an AC excitation voltage signal of 10 mV amplitude in the frequency range from 30 kHz to 10 mHz. The impedance measurements are repeated at least 3 times for a sample in each environment to ensure the reproducibility of results. The impedance data normalized by the exposed surface area of the sample is analyzed using ZView v3.5h software. The fitting of the data is done with an equivalent electrical circuit to obtain the values of circuit elements and compare the corrosion behavior of samples.

3.3.5. Potentiostatic polarization

Potentiostatic polarization is performed on the samples to obtain a fresh corroded surface to carry out surface characterization. The tests are performed in the deaerated 0.1 M H_2SO_4 solution. The system is allowed to stabilize for 1 hour at room temperature before the experiment to obtain a steady open-circuit potential. The samples are allowed to corrode in a controlled manner by applying a constant potential of +40 mV relative to their OCP values recorded during experiments for a period of 10 minutes. The samples are then ready for surface characterization.

3.4. Surface Characterization

The surface topography of the samples after potentiostatic polarization is studied by atomic force microscopy (AFM). Before the AFM scan, a suitable area of interest on the sample surface is delimited by indents using Struers DuraScan 70 Vickers hardness test instrument. AFM scans are performed on the samples with low surface texture using a Bruker Dimension Edge™ in tapping mode with antimony (n) doped silicon tip. The measurements are conducted with a pixel resolution of 1024 × 1024 and a scan rate of 0.6 Hz. Data collection during the scans is done with Nanodrive v8.05 software. Data processing and analysis are done using Gwyddion v2.50 software.

3.5. Numerical modeling of corrosion

Following the experimental results, an attempt is made to model the corrosion behavior of polycrystalline pure Fe. This is achieved by building a numerical model in COMSOL Multiphysics® using the Electrochemistry module. The model predicts the corrosion behavior of pure polycrystalline iron using the corrosion behavior of different crystallographic orientations of iron. The model is adapted from the work of Abodi et al. [92] on macroscopic corrosion of AA2024 Al alloy. They generated the polarization curve of the macroscopic system using individual polarization curves of the Al matrix, intermetallic compounds, and sigma-phase precipitates as inputs to the model. The current model follows an analogous pathway to generate the polarization curve of the polycrystalline pure Fe using corrosion information of crystallographic orientations from the literature.

3.5.1. Model parameters

The input parameters of the corrosion model include electrochemical parameters of each contributing crystallographic orientation (i.e., corrosion potential, corrosion current density, and Tafel slopes), the conductivity of the electrolyte, and the range of externally applied potential. The crystallographic input data are taken from the work of Fushimi et al. [51]. They studied the corrosion behavior of six different crystallographic orientations of pure Fe in 0.05 M H_2SO_4 (pH = 1). The obtained information is shown in fig. 3.13. The average value of each corrosion parameter is used as input. The electrolyte conductivity is taken to be 4 S/m.

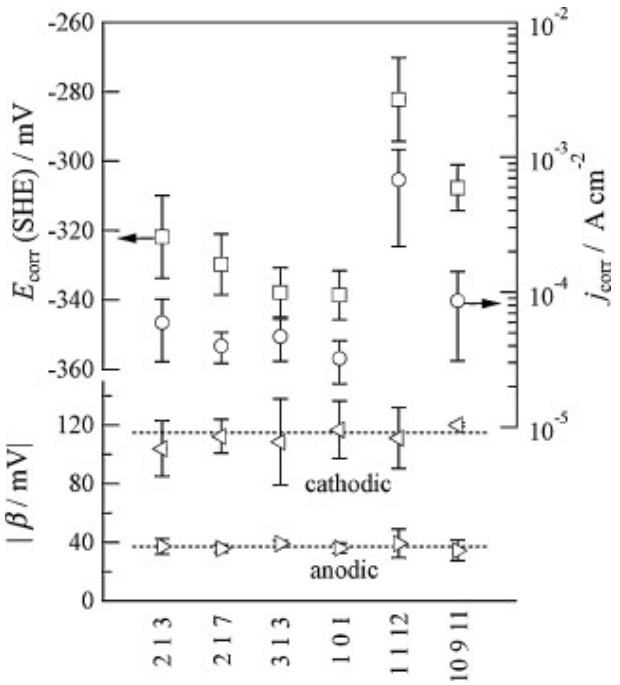

Figure 3.13: Electrochemical parameters of different crystallographic orientations in 0.05 M H_2SO_4 solution available as input for the model [51].

3.5.2. Model geometry

The schematic model geometry used in COMSOL Multiphysics® is shown in fig. 3.14. The geometry can be in 2-D or 3-D. In the 2-D geometry, the blue line indicates the electrochemical interface, and the gray region is the electrolyte domain. In 3-D geometry, the top cube is the electrolyte domain, and the bottom geometry is the electrode domain in the form of a bi-crystal. In 2-D configuration, the electrolyte domain and the electrochemical interface are modeled. In the 3-D configuration, the electrode domain is modeled additionally. This is not relevant for the current model study because the potential across the electrode is constant due to its high electrical conductivity. The modeling of electrode domains is of particular interest in the case of porous and gas-diffusion electrodes. Hence, in the present model, the 2-D geometry is used. In the current approach, the preliminary studies are done on a bi-crystal sample geometry to validate the individual polarization curves of the crystallographic orientation with their corresponding experimental polarization curves. After successful validation, the model is implemented on the three samples. The distribution of different orientations in the samples is obtained using their EBSD maps.

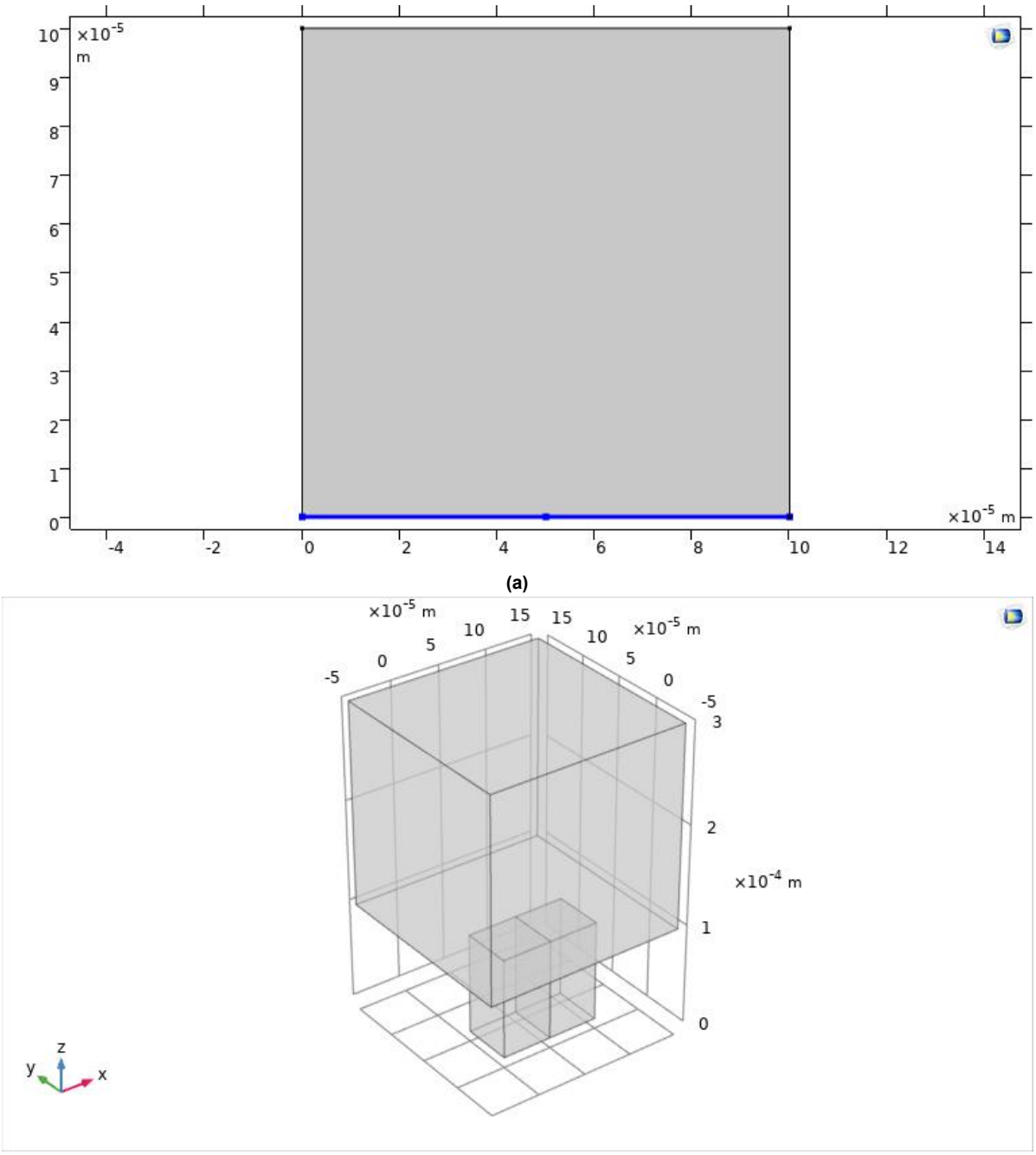

Figure 3.14: Model geometry in (a) 2-D and (b) 3-D designed in COMSOL MultiPhysics®.

3.5.3. Model boundary conditions

As discussed in the section 2.4.1, the boundary conditions imposed on the 2-D geometry are listed in table 3.2. The model calculates the current density based on the applied potential using the Tafel equation. The line average of this current density across the electrochemical interface is plotted against the applied potential to generate the polarization curve.

Table 3.2: Summary of boundary conditions imposed on the model geometry

Boundary condition	**Comments**
$i_{\mathrm{l}} = -\sigma_{\mathrm{l}} \nabla(\phi_{\mathrm{l}})$	Applied in the electrolyte domain to calculate current density based on the potential gradient.
$\eta = \phi_{\mathrm{s,ext}} - \phi_{\mathrm{l}} - E_{\mathrm{eq}}$	Applied at the electrochemical interface to define overpotential due to the externally applied potential.
$i_{\mathrm{loc}} = i_0 * 10^{\left(\frac{\eta}{\beta}\right)}$	Applied at the electrochemical interface to calculate local current density due to the applied overpotential.
$i_{\mathrm{total}} = \sum_m i_{\mathrm{loc,m}}$	Sum of currents generated across the electrochemical interface.
$\hat{n} \cdot i_{\mathrm{l}} = i_{\mathrm{total}}$	Conservation of charge by Kirchhoff's current law.
$\phi_{\mathrm{l,bnd}} = 0$	Applied at one of the electrolyte boundaries to set reference for the potential values.
$-\hat{n} \cdot i_{\mathrm{l}} = 0$	Applied at remaining electrolyte boundaries for insulation.

4

Results and Discussion

In this chapter, the results of the experiments and the model outlined in chapter 3 are presented. The results are analyzed, and correlations are made wherever necessary between the observations for better comprehension and to draw suitable conclusions. The chapter begins with the microstructure characterization results, followed by results of electrochemical characterization and surface characterization. Then, the results of the corrosion model are presented with model validation and comparison with the experimental findings. A summary and overall interpretation of the results is included in the final section of the chapter.

4.1. Microstructure characterization

4.1.1. Optical Microscopy

Fig. 4.1 shows the optical microscopy images of the samples after etching with a 2% Nital solution.The samples have a single ferrite phase. The Fe-700 sample shows fine equiaxed grains due to the recrystallization process during annealing. The Fe-950 and Fe-1100 samples exhibit relatively coarser grains due to their higher annealing temperatures. Some black spots are observed scattered in the images. They are likely to be impurities or particles from the polishing step. The grain boundaries are distinctly visible, but some grain boundaries appear under-etched. Hence, to perform accurate grain size measurement, optical images after the corrosion test in 0.1 M H_2SO_4 solution are used. The exact images used for calculation are included in the Appendix A2. The grain sizes of the samples, calculated by the line intercept method, are summarized in the table 4.1.

Table 4.1: Summary of grain size of samples calculated by line intercept method

Sample	Grain size (µm)
Fe-700	30 ± 2.4
Fe-950	48.9 ± 3.5
Fe-1100	75.5 ± 8.6

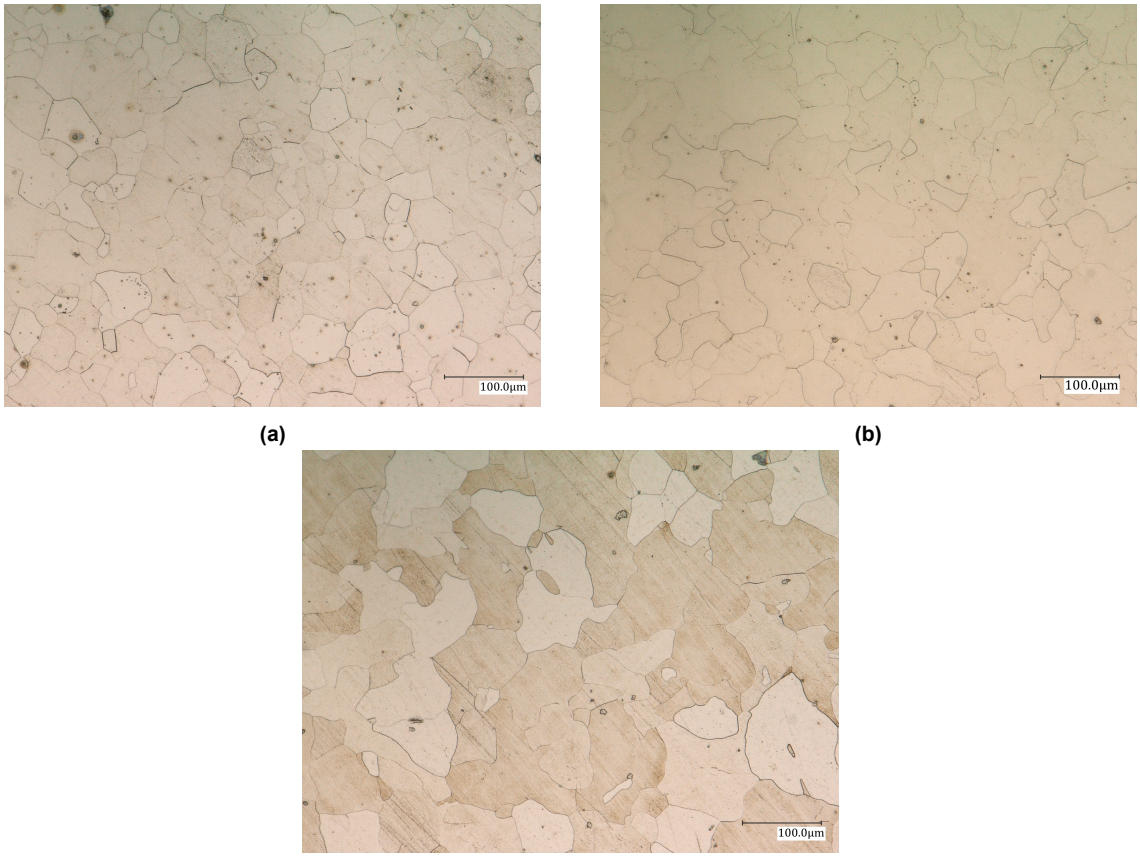

Figure 4.1: Optical microscope images of (a) Fe-700 (b) Fe-950 and (c) Fe-1100 samples after etching with 2% Nital solution. (Magnification: 500X)

4.1.2. EBSD

The microstructural features of the samples are studied by electron backscatter diffraction. Fig. 4.2 shows the inverse pole figure (IPF) maps of the samples. They are obtained after EBSD scans on the plane of the samples consisting of the rolling direction and the transverse direction. The Fe-700 sample shows prominence of grains with <111> parallel to the normal direction. For Fe-950 and Fe-1100 samples, it is difficult to comment on the texture aspect due to the relatively smaller amount of grains. Hence, XRD macro-texture analysis is performed for better understanding and is discussed in section 4.1.3. Table 4.2 summarizes other microstructural features obtained from the EBSD analysis. The grain size of the samples obtained here is similar to that calculated by the line intercept method.The grain boundary fraction increases with a reduction in grain size. The grain boundaries are classified as low angle and high angle grain boundaries using a threshold misorientation angle of 15°. Based on this classification, it is evident that high angle grain boundaries constitute a significant portion of the grain boundaries in all the samples. The geometrically necessary dislocation (GND) density calculated for the samples reveals that they are more or less in a similar order. The values indicate samples are nearly strain-free with small difference in dislocation densities.

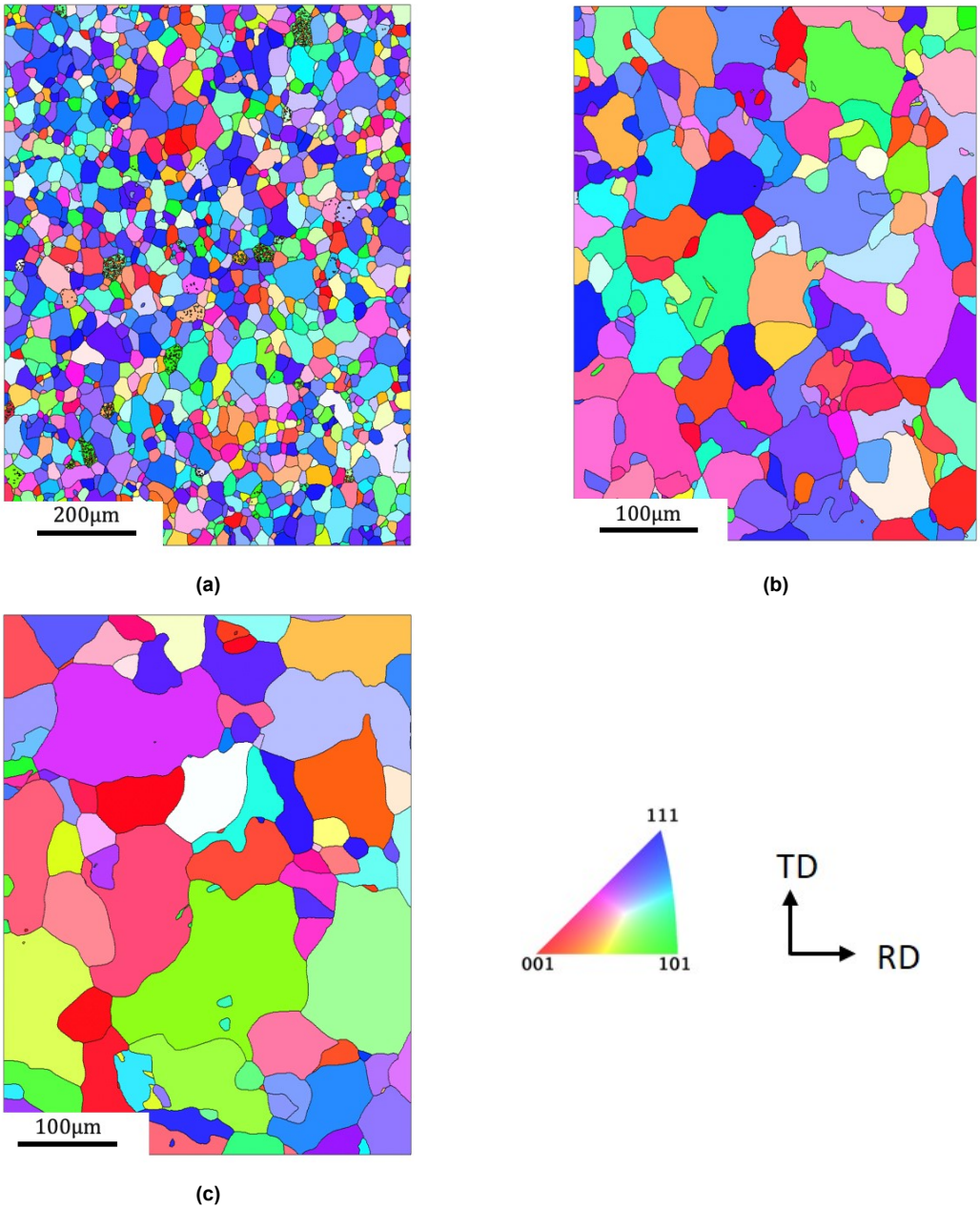

Figure 4.2: EBSD inverse pole figure maps of (a) Fe-700 (b) Fe-950 and (c) Fe-1100 samples showing grain orientations along the normal direction of the samples.

Table 4.2: Summary of microstructure parameters obtained from EBSD data of the samples.

Sample	Grain size (µm)	Grain boundary fraction (μm^{-1})	HAGB fraction (μm^{-1})	LAGB fraction (μm^{-1})	GND (m^{-2})
Fe-700	25.7 ± 2.1	0.102	0.096	0.006	$3.4 \pm 0.4 \times 10^{13}$
Fe-950	52.7 ± 4	0.052	0.050	0.002	$7.9 \pm 0.2 \times 10^{12}$
Fe-1100	91.1 ± 12.3	0.033	0.032	0.001	$4.4 \pm 0.2 \times 10^{12}$

4.1.3. XRD texture analysis

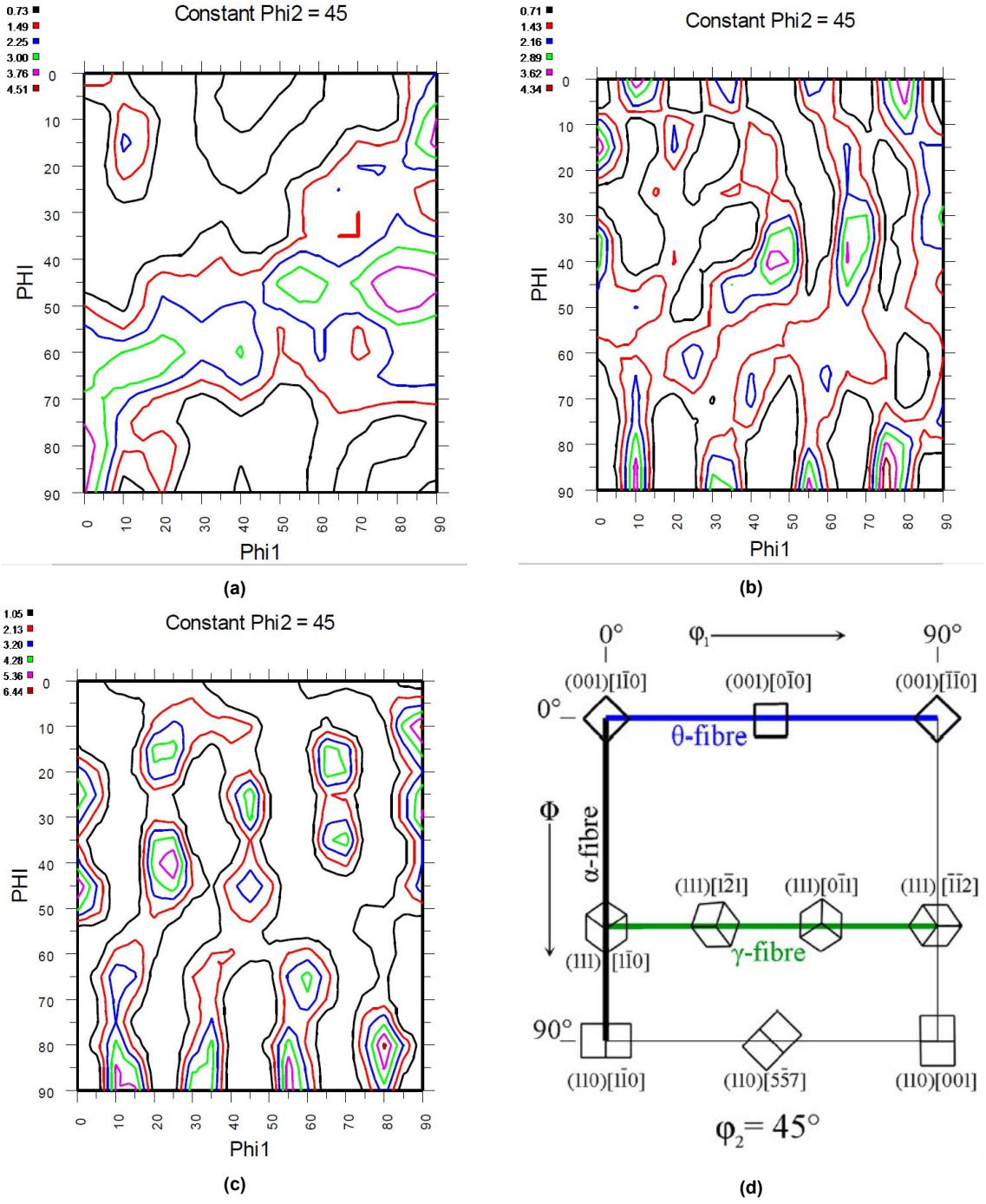

Figure 4.3: ODF section phi2 = 45°of (a) Fe-700 (b) Fe-950 and (c) Fe-1100 samples d) illustrative phi2 = 45°ODF section representing the characteristic texture components in BCC metals [50].

Fig. 4.3 shows the constant phi2 = 45°section of the orientation distribution function (ODF) plots of the three samples along with a representative ODF plot showing the characteristic texture components seen in BCC materials. The ODF plots are represented using the Bunge notation.

In the ODF section, the horizontal region near PHI = 0°denotes the grains with {001} orientation parallel to the sample's rolled surface. Fe-700 sample and Fe-1100 sample have little or no iso-intensity lines in this region, indicating a meager fraction of {001} grains. Fe-950 sample has a relatively higher density of the iso-intensity lines indicating a higher volume fraction of grains close to {001} orientation. Similarly, in the ODF section, the horizontal region near PHI = 50°to 60°denotes the grains with {111} orientation parallel to the rolled surface. Fe-700 sample has most of its iso-intensity lines lying here horizontally. This is the γ fibre that is associated with the recrystallization of rolled BCC metals and alloys [50]. Hence, the Fe-700 sample has most of the grains close to {111} orientation parallel to the rolled surface. Fe-950 and Fe-1100 samples have a significantly lower density of iso-intensity lines in the γ fibre region compared to Fe-700 and consequently have a smaller fraction of grains close to {111} orientation. Finally, in the ODF section, the horizontal region near PHI = 90°denotes the grains with {110} orientation parallel to the rolled surface of the sample. Fe-700 sample has a small region of a high density of iso-intensity lines indicating a small fraction of grains close to {110} orientation. Fe-950 and Fe-1100 samples have multiple small regions of a high density of iso-intensity lines, indicating a higher fraction of grains close to {110} orientation. Fe-950 and Fe-1100 samples also show dense regions of iso-intensity lines at several intermediate orientations, which is missing in the Fe-700 sample. This analysis gives a clear picture of the orientation distribution of grains at the corrosion front facing the solution medium in different samples.

4.2. Electrochemical characterization

4.2.1. Open circuit potential measurement

The open-circuit potential (OCP) of the sample is recorded relative to the reference electrode in the electrolyte medium to assess the system's stability before performing tests like electrochemical impedance spectroscopy (EIS) and potentiodynamic polarization. A stable OCP is a prerequisite for these tests because the excitation voltage signal in EIS and the potential sweep range in potentiodynamic polarization are applied relative to the OCP.

Fig. 4.4 shows the evolution of OCP with time for the three heat-treated Fe samples in deaerated 0.1 M H_2SO_4 and 0.01 M H_2SO_4 solutions, respectively. In all the samples, the potential shows a drop in value initially and then attains a stable value. The observed drop in potential could be associated with the dissolution of the naturally existing oxide layer on the sample surface [93]. According to the Pourbaix diagram (fig. 2.2), Fe shows active behavior at pH = 1.1 (0.1 M H_2SO_4) and 1.9 (0.01 M H_2SO_4) in the solutions used. The decrease in potential over time shows the increase in the corrosion tendency of the samples. Around t = 1500 s, the potential values begin to stabilize as the system moves close to the equilibrium. At the end of 1 hour, the average potential values are summarized in table 4.3 for the samples in both of the tested solutions. In 0.1 M H_2SO_4 solution, the potential values of the samples are close. Fe-950 sample has the most negative potential value, indicating its higher corrosion tendency than other samples. In 0.01 M H_2SO_4 solution, the potential values of the samples are far apart, as evident from the plot. Fe-700 sample has the most negative potential value followed by Fe-950 and Fe-1100 samples. These values indicate an increase in corrosion tendency with reduction in grain size of the samples in 0.01 M H_2SO_4 solution.

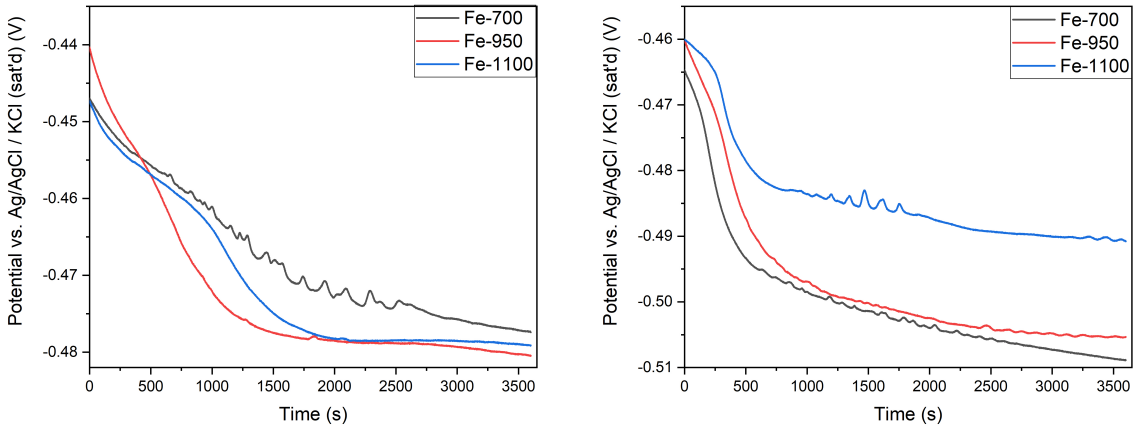

Figure 4.4: Evolution of OCP with time of the samples in (a) 0.1 M H_2SO_4 and (b) 0.01 M H_2SO_4 solutions.

Table 4.3: Summary of the OCP values of the samples in the tested solutions

Sample	OCP in 0.1 M H_2SO_4 (V)	OCP in 0.01 M H_2SO_4 (V)
Fe-700	-0.469 ± 0.011	-0.510 ± 0.012
Fe-950	-0.475 ± 0.006	-0.505 ± 0.005
Fe-1100	-0.473 ± 0.008	-0.492 ± 0.009

4.2.2. Potentiodynamic polarization measurement

Fig. 4.5 shows the corrosion behavior of samples during potentiodynamic polarization in the deaerated 0.1 M H_2SO_4 solution. A noticeable difference is observed in the cathodic branches of the polarization curves. Fe-950 sample shows a higher cathodic current density than Fe-700 and Fe-1100 samples in the applied potential range. On the contrary, the anodic branches of the polarization curves overlap over each other. This observation indicates the role of cathodic reaction kinetics in controlling the corrosion behavior of the samples. Table 4.4 summarizes the polarization parameters obtained from the curves by Tafel extrapolation. The samples have similar corrosion potential (E_{corr}) values, which is also evident from the plot. The corrosion current density (i_{corr}) values are comparable for Fe-700 and Fe-1100 samples and lower than the Fe-950 sample. This implies that on decreasing the grain size, the corrosion rate first increases and then decreases. The increase in the corrosion rate for the Fe-950 sample relative to the Fe-1100 sample can be attributed to the increase in grain boundary density, which implies more high energy active sites for corrosion [2]. However, the decrease in the corrosion rate observed for the Fe-700 sample is counter-intuitive and requires a more in-depth analysis of the role of other microstructural features. From the microstructure characterization analysis, this unexpected corrosion behavior can be attributed to the dominant effect of crystallographic texture in Fe-700 sample. The corrosion rate among crystallographic orientations of Fe in active condition follows the sequence: (110) < (111) < (001) [51]. The low corrosion rate of {111} oriented grains more than compensate for the increase in corrosion rate due to higher grain boundary fraction.

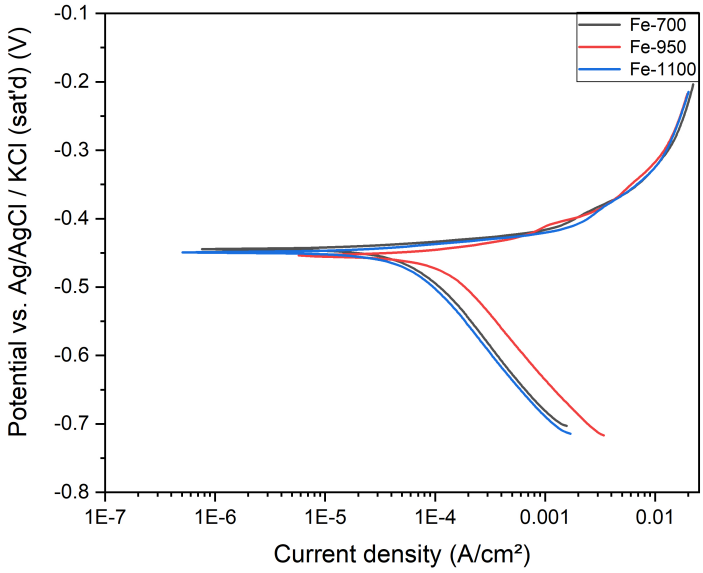

Figure 4.5: Potentiodynamic polarization curves of the samples measured in 0.1 M H_2SO_4 solution.

Table 4.4: Summary of electrochemical parameters obtained by Tafel extrapolation of polarization curves obtained in 0.1 M H_2SO_4 solution.

Sample	E_{corr} (mV)	i_{corr} (μA/cm^2)	β Anodic (mV)	β Cathodic (mV)
Fe-700	-468 ± 7	73 ± 4	45 ± 4	191 ± 15
Fe-950	-466 ± 8	149 ± 23	51 ± 5	198 ± 5
Fe-1100	-469 ± 6	76 ± 10	44 ± 2	199 ± 13

The anodic Tafel slope (β anodic) observed in this work is similar to that observed in the literature [51]. The anodic reaction mechanism is forwarded by Bockris and co-workers and is shown in the equations (4.1 - 4.3). They proposed two single-electron exchange reactions, with the de-electronation step of the adsorbed iron hydroxide (equation 4.2) as the rate-determining step [94].

$$Fe + H_2O \leftrightarrow FeOH_{ads} + H^+ + e - \quad (4.1)$$

$$FeOH_{ads} \rightarrow FeOH^+ + e - \quad (4.2)$$

$$FeOH^+ + H^+ \leftrightarrow Fe^{2+} + H_2O \quad (4.3)$$

The cathodic Tafel slope observed in this work is higher than the values observed in literature for hydrogen evolution reaction (HER). The HER is given by the Volmer-Heyrovsky-Tafel mechanism [95]. The corresponding reaction steps have been shown in the equations (4.4 - 4.6). Here 'M' denotes empty site on the metal electrode surface.

$$H_3O^+ + M + e- \leftrightarrow MH_{ads} + H_20 \quad \text{(Volmer step)} \tag{4.4}$$

$$MH_{ads} + H_3O^+ + e- \leftrightarrow H_2 + H_2O + M \quad \text{(Heyrovsky step)} \tag{4.5}$$

$$2MH_{ads} \leftrightarrow H_2 + 2M \quad \text{(Tafel step)} \tag{4.6}$$

The first step is the Volmer step, in which the hydronium ion gets adsorbed on the electrode surface as an intermediate. Now, the next step i.e. desorption can proceed in either of the two ways. The adsorbed hydrogen can either react with hydronium ion from the solution with the transfer of an electron to give molecular hydrogen (Heyrovsky step) or combine with another adsorbed hydrogen to give molecular hydrogen (Tafel step). If the Volmer step is rate-limiting, the Tafel slope is around 118 mV/decade; else, the Tafel slope is 39 mV/decade or 30 mV/decade based on the Heyrovsky step, or the Tafel step being rate-limiting, respectively. Based on the cathodic Tafel slope obtained here, it is difficult to comment on the rate-limiting step. However, the cathodic Tafel slope is consistent across the samples, indicating a similar reaction mechanism. The possibility of any dissolved oxygen in the solution resulting in a cathodic reaction to give water is ruled out based on the corrosion potential of the samples lying outside the water stability zone in the Pourbaix diagram for the pH of the used solutions. Hence, the reason for the higher cathodic Tafel slope observed could be related to the presence of adsorbed species on the electrode surface, limiting the hydrogen evolution reaction. The presence of adsorbed species has been noticed in the impedance spectroscopy results, as discussed later in section 4.2.4.

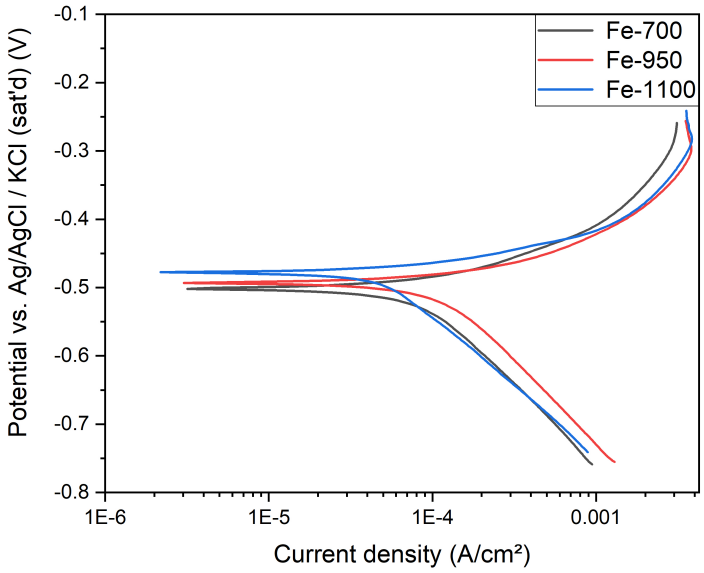

Figure 4.6: Potentiodynamic polarization curves of the samples measured in 0.01 M H_2SO_4 solution.

Fig. 4.6 shows the potentiodynamic polarization results obtained for the samples in the deaerated 0.01 M H_2SO_4 solution. This experiment aims to understand the effect of change in pH inside the active region on the corrosion behavior and the trend of corrosion rate among the samples. Some similarities and differences can be noticed here compared to the results obtained in the 0.1 M H_2SO_4 solution (fig. 4.5). The cathodic current density of the Fe-950 sample is higher than the other samples. The cathodic branches of Fe-700 and Fe-1100

samples overlap quite well, similar to the previous results in 0.1 M H_2SO_4 solution. The anodic branch of each sample is distinctly visible. The polarization parameters obtained from Tafel extrapolation are summarized in table 4.5.

Table 4.5: Summary of electrochemical parameters obtained by Tafel extrapolation of polarization curves obtained in 0.01 M H_2SO_4 solution.

Sample	**E_{corr} (mV)**	**i_{corr} (μA/cm^2)**	**β Anodic (mV)**	**β Cathodic (mV)**
Fe-700	-502 ± 12	74 ± 15	62 ± 12	220 ± 8
Fe-950	-498 ± 4	111 ± 4	75 ± 4	235 ± 7
Fe-1100	-486 ± 6	50 ± 20	48 ± 9	198 ± 23

The Fe-1100 sample shows a nobler E_{corr} value followed by Fe-950 and Fe-700 samples. The E_{corr} values of the samples are relatively more negative than those obtained in 0.1 M H_2SO_4 solution. Fe-950 and Fe-1100 samples show a decrease in the corrosion current density with dilution from 0.1 M to 0.01 M H_2SO_4 solution, while the Fe-700 sample shows negligible change in corrosion current density. The corrosion current density follows the sequence Fe-1100 < Fe-700 < Fe-950. This trend provides a better picture of the corrosion behavior. Fe-700 and Fe-950 samples individually show a higher corrosion rate than the Fe-1100 sample. It shows that the corrosion rate increases with a decrease in grain size. However, the amount of increase is controlled by grain boundary fraction and crystallographic orientation of grains. For the Fe-950 sample, a higher grain boundary fraction and the presence of a relatively higher volume fraction of {001} oriented grains reinforce each other to achieve a high corrosion rate. For the Fe-700 sample, a higher grain boundary fraction and the predominant presence of grains with {111} orientation have contrasting effects on corrosion behavior. Consequently, the net increase in the corrosion rate of the Fe-700 sample is lower than the Fe-950 sample. The combined effect of the grain size and crystallographic orientation is visible in the corrosion behavior of the samples.The cathodic Tafel slopes of the samples are higher than expected, similar to the results in the 0.1 M H_2SO_4 solution. This is likely associated with the presence of adsorbed species limiting the hydrogen evolution reaction.

4.2.3. Morphology of corroded surface

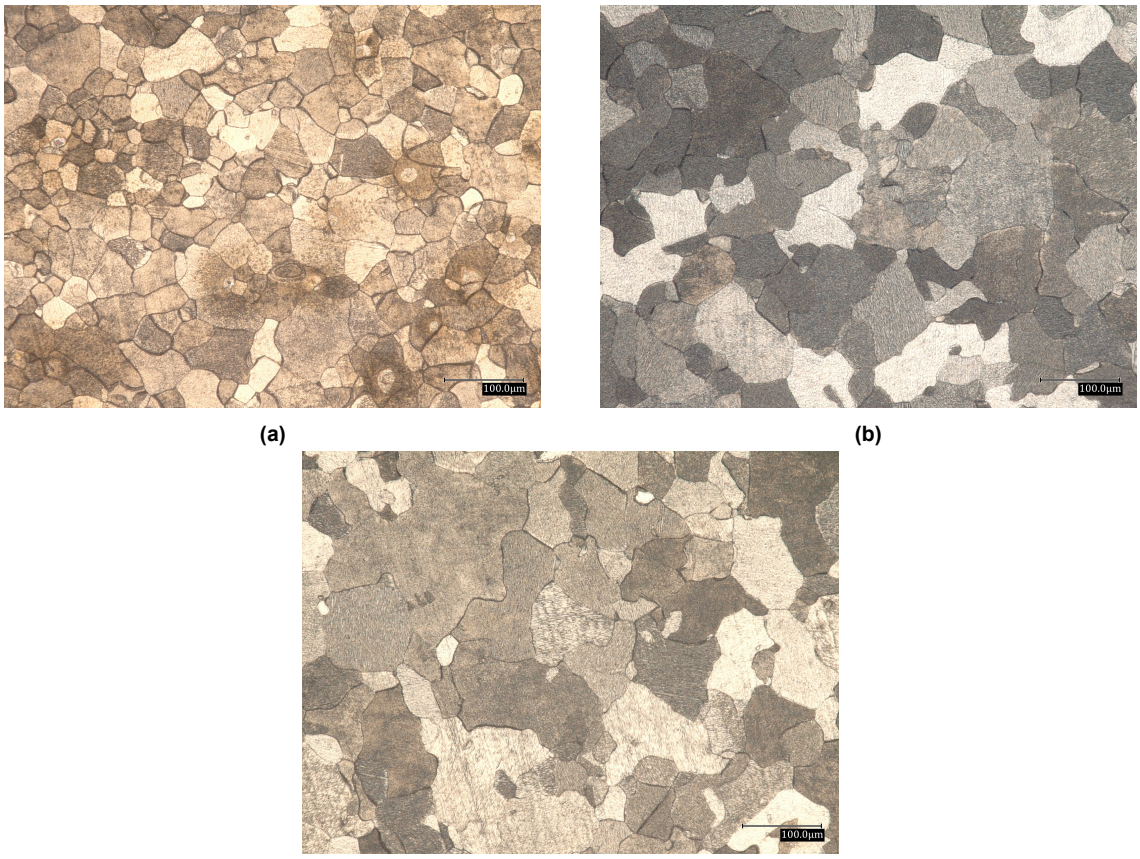

Figure 4.7: Optical images showing comparison of surface morphology of (a) Fe-700 (b) Fe-950 and (c) Fe-1100 samples after corrosion test in 0.1 M H_2SO_4 solution. (Magnification: 500X)

The surface morphology of the samples has been studied under the optical microscope after the potentiodynamic polarization tests. Fig. 4.7 shows the optical images of the samples after corrosion in 0.1 M H_2SO_4 solution. Uniform corrosion is observed in all three samples. The grain and grain boundaries are visible clearly. Some grain boundaries appear to be attacked more than others. Fe-700 sample has more grain boundaries with a deeper attack than Fe-950 and Fe-1100 samples. This could be related to the nature of grain boundaries or crystallographic orientations of the neighboring grains which form micro-galvanic couple due to difference in their corrosion activity. High angle grain boundaries have been reported to corrode more actively than low angle grain boundaries in copper [62] and aluminum [63]. For better insight, surface topography analysis of the corroded surface is pursued with atomic force microscopy (AFM) and discussed later in section 4.3.

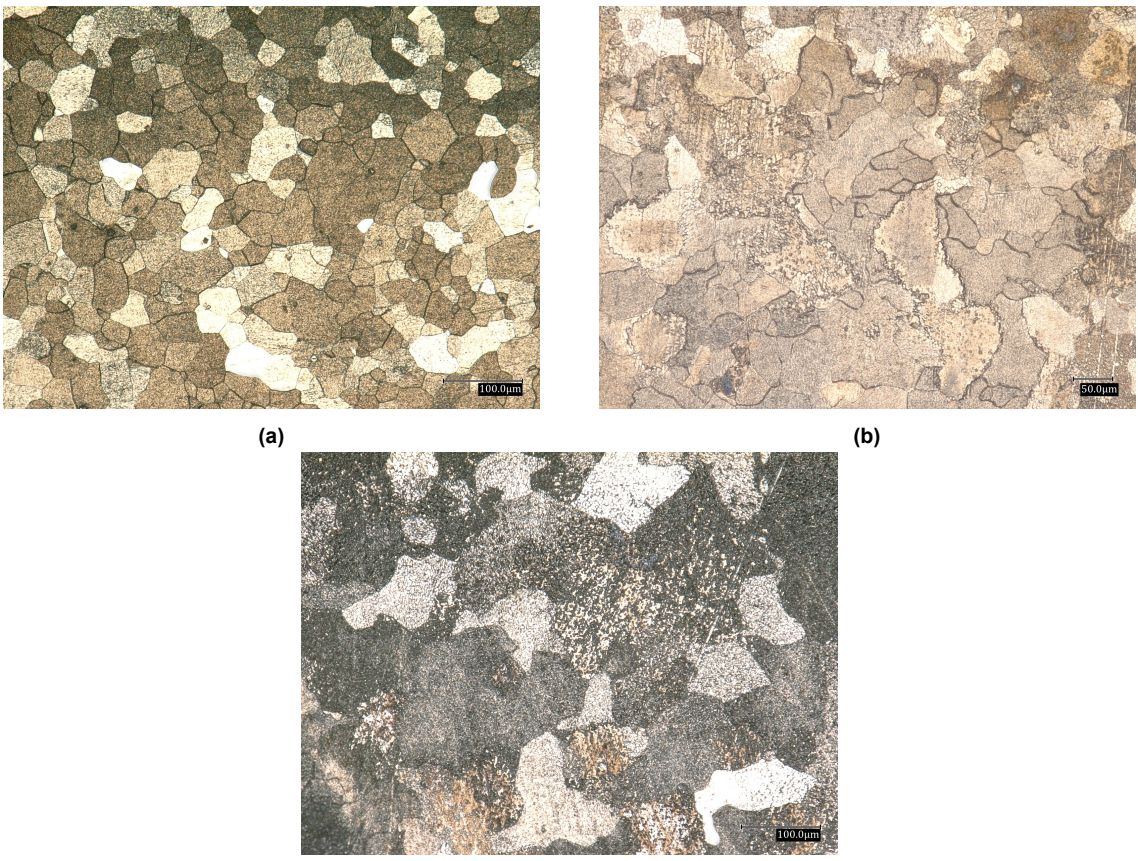

Figure 4.8: Optical images showing comparison of surface morphology of (a) Fe-700 (b) Fe-950 and (c) Fe-1100 samples after corrosion test in 0.01 M H_2SO_4 solution. (Magnification: 500X)

Fig. 4.8 shows the optical images of the samples after the corrosion study in 0.01 M H_2SO_4 solution. Grains and grain boundaries are distinctly visible in Fe-700 and Fe-950 samples. The attack on grain boundaries appears to have reduced relative to the results observed in the 0.1 M H_2SO_4 solution.Some grains appear brighter in the Fe-700 sample indicating a selective dissolution of grains based on the crystallographic orientation. In the Fe-1100 sample, the surface appears dull with a fuzzy appearance of grain boundaries, indicating a relatively lesser degree of corrosion attack than Fe-700 and Fe-950 samples. The corrosion in the 0.01 M H_2SO_4 solution is inhomogeneous. Some regions in the samples without corrosion attack are also observed. Significant variations in the surface morphology are observed in different trials of the same sample, as shown in fig. 4.9 and fig. 4.10. This variation in the morphology of the corroded surface between trials is ascribed to the dilute nature of the solution.

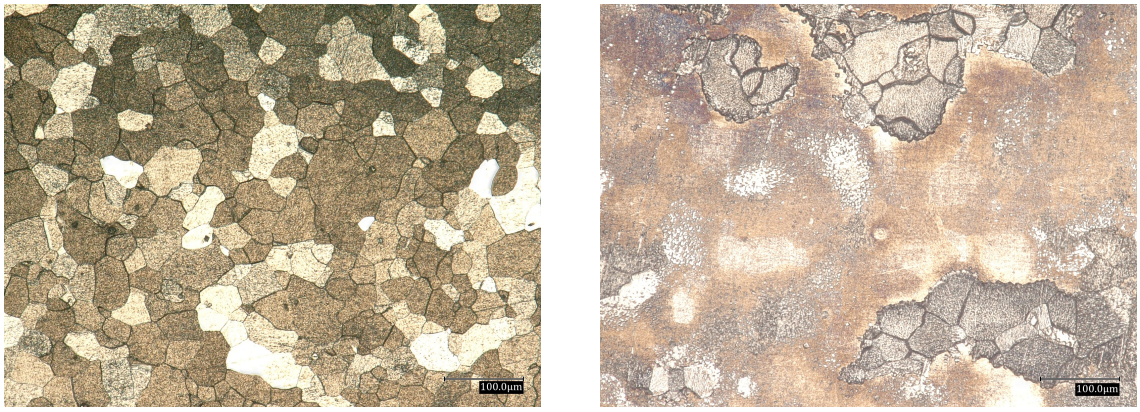

(a) (b)

Figure 4.9: Optical images of Fe-700 sample showing variation in surface morphology in different trials after corrosion test in 0.01 M H_2SO_4 solution. (Magnification: 500X)

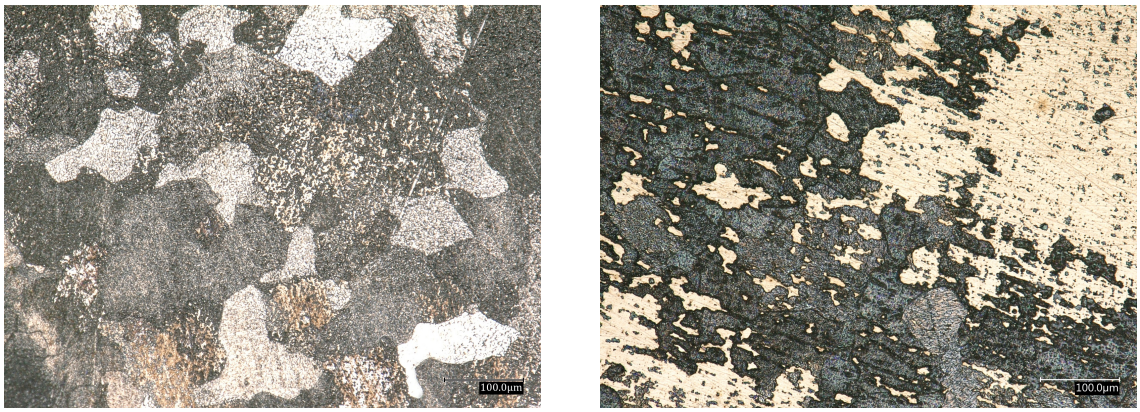

(a) (b)

Figure 4.10: Optical images of Fe-1100 sample showing variation in surface morphology in different trials after corrosion test in 0.01 M H_2SO_4 solution. (Magnification: 500X)

4.2.4. Electrochemical Impedance Spectroscopy (EIS)

EIS is performed on the samples in the solution medium to understand the electrochemical interface and the corrosion resistance of the samples. Fig. 4.11 shows the Nyquist and Bode plots of the samples in deaerated 0.1 M H_2SO_4 solution. The shape of the Nyquist plots is identical across the samples with a depressed semi-circular appearance. A single capacitive loop is observed at high to mid-frequencies in all the samples, associated with the charge transfer across the electrical double layer. At low frequencies, a small inductive loop is observed. The inductive loop is attributed to the relaxation of adsorbed species on the electrode surface. They could be intermediate Fe(I) and Fe(II) species, based on similar observations in other studies [96–99]. The diameter of the capacitive loop is an indication of the charge transfer resistance of the sample. Fe-950 sample has the smallest diameter among all samples. Fe-700 and Fe-1100 samples show capacitive loops of similar size with a slight difference. This observation indicates lower corrosion resistance of the Fe-950 sample relative to Fe-700 and Fe-1100 samples.

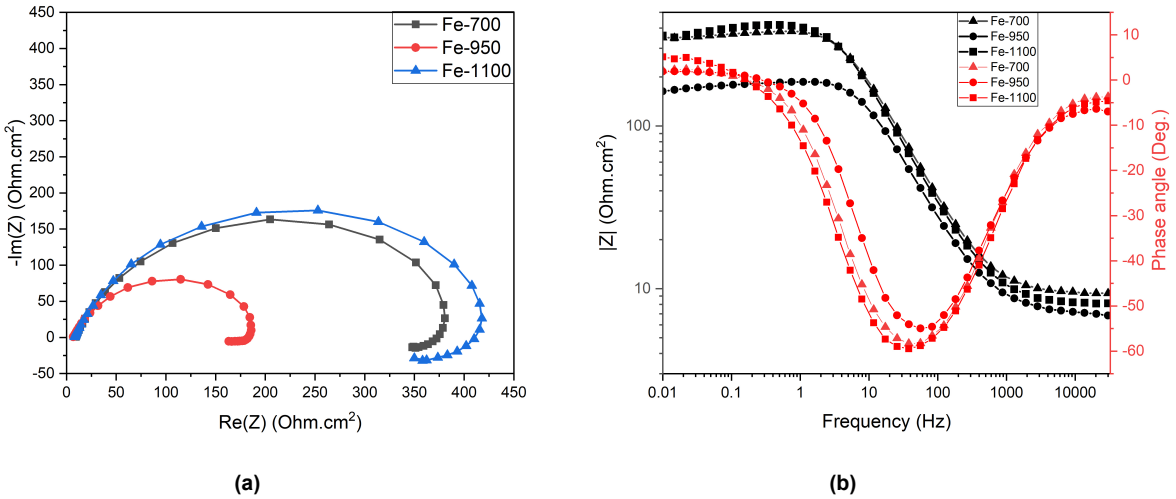

Figure 4.11: (a) Nyquist and (b) Bode plots of the samples in 0.1 M H_2SO_4 solution.

The Bode |Z| plots of the samples show frequency-independent regions at low and high frequencies and a linear slope in the intermediate frequencies associated with the double-layer capacitance. The phase angle plots show the non-ideal nature of the capacitance as the minimum phase angle is quite far from -90°(for a pure capacitor). This non-ideal behavior is ascribed to the inhomogeneities and roughness of the electrode surface [14]. The experimental data are fitted using an equivalent electrical circuit (fig. 4.12), as proposed in similar studies [14, 98], to quantify the impedance results. In the figure, R_s is the solution resistance, R_{ct} is the charge transfer resistance, R_L is the resistance and L1 is the inductance associated with the adsorbed species, and CPE1 is the constant phase element (CPE) representing the non-ideal double-layer capacitance. The CPE impedance is given by the equation 4.7.

$$Z_{CPE} = \frac{1}{Y_0(j\omega)^n} \tag{4.7}$$

Here, Y_0 is the CPE constant, ω is the angular frequency, and n is a parameter ranging from 0 to 1, with n = 1 for a pure capacitor and n = 0 for a pure resistor.

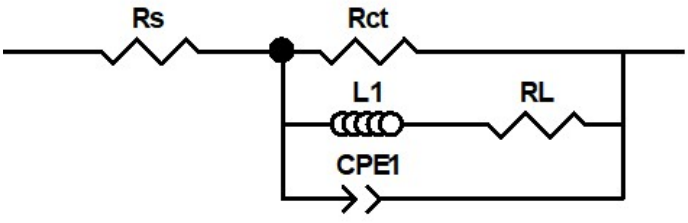

Figure 4.12: Equivalent electrical circuit for fitting the EIS data.

The average values of the circuit elements, obtained after multiple repetitions for each sample, are summarized in table 4.6. The charge transfer resistance is a measure of the corrosion resistance of the sample. Hence, the corrosion resistance initially decreases with a decrease in grain size and then increases. This trend is consistent with the potentiodynamic polarization results in the 0.1 M H_2SO_4 solution and confirms the dominant effect of texture

in the corrosion behavior of Fe-700 sample. The role of circuit elements R_L and L remain less explored in literature due to the non-stationary nature of adsorption, lack of sufficient data points in the low-frequency region, and scatter in the inductive loop data affecting the fitting accuracy [98]. In this work, the R_L and L values show large scatter, and hence, they are not analyzed further. The 'n' values are similar across the samples indicating similar nature of the electrical double layer. The low chi-square (χ^2) values indicate that a good fitting is achieved in all the samples.

Table 4.6: Summary of impedance parameters obtained after fitting the EIS plots of samples in 0.1 M H_2SO_4 solution.

Sample	R_s ($\Omega.cm^2$)	R_{ct} ($\Omega.cm^2$)	R_L ($\Omega.cm^2$)	L (H. cm^2)	CPE-Y_0 X 10^{-4} ($\Omega^{-1}.cm^{-2}s^n$)	n	χ^2 X 10^{-4}
Fe-700	7.9 ± 1.3	438.4 ± 82.9	1310.0 ± 500.9	1642.5 ± 1116.9	1.588 ± 0.117	0.816 ± 0.016	4.8 ± 1.7
Fe-950	7.2 ± 0.6	187.6 ± 43.9	707.8 ± 120.4	114.5 ± 34.9	2.199 ± 0.293	0.824 ± 0.014	10.7 ± 8.7
Fe-1100	10.7 ± 2.7	411.9 ± 161.1	1780.7 ± 868.6	3636.2 ± 4335.4	1.798 ± 0.301	0.821 ± 0.014	3.6 ± 1.7

EIS tests are also performed on the samples in deaerated 0.01 M H_2SO_4 solution. Fig. 4.13 shows the corresponding Nyquist and Bode plots of the samples. The Nyquist plot shows a depressed semi-circular capacitive loop at high to mid-frequencies and a small inductive loop at low frequencies. The consistent appearance of inductive loops in both of the tested solution mediums and across all samples shows that it is not a mere artifact. As discussed earlier, the inductive loop is associated with the relaxation of adsorbed intermediate species on the electrode surface. The diameters of the capacitive loops follow the sequence Fe-1100 > Fe-700 > Fe-950. Hence, their corrosion resistance also follows the same order. The Bode phase angle plots show that the double layer behaves as a non-ideal capacitor since the minimum phase angle falls quite short of the expected -90°, the phase difference for a pure capacitor. This non-ideal behavior is attributed to the surface roughness and heterogeneity [14]. The impedance data are fitted using the equivalent electrical circuit, as shown in fig. 4.12. The average values of the circuit elements, obtained after multiple repetitions for each sample, are summarized in table 4.7. The solution resistance is higher than in 0.1 M H_2SO_4 solution because of the dilute nature of the solution. The charge transfer resistance values confirm the assessment of corrosion resistance of samples discussed earlier in this section. As the grain size decreases, the corrosion resistance first decreases and then increases. The observations from EIS results are consistent with that from the potentiodynamic polarization tests in 0.01 M H_2SO_4 solution and highlight the combined effect of the grain size and the crystallographic orientations on the corrosion behavior of the samples. The 'n' parameter is similar across the samples indicating similar nature and quality of the electrical double layer. The role of circuit elements R_L and L in the corrosion behavior is not considered in the analysis owing to the reasons stated earlier in the section.The low chi-square (χ^2) values indicate that a good fitting is achieved in all the samples.

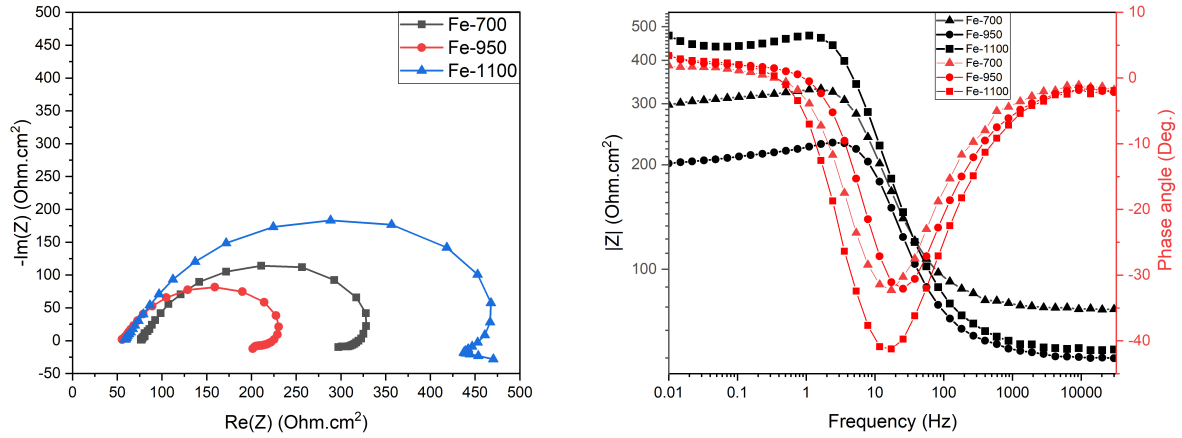

Figure 4.13: (a) Nyquist and (b) Bode plots of the samples in 0.01 M H_2SO_4 solution.

Table 4.7: Summary of impedance parameters obtained after fitting the EIS plots of samples in 0.01 M H_2SO_4 solution.

Sample	R_s ($\Omega.cm^2$)	R_{ct} ($\Omega.cm^2$)	R_L ($\Omega.cm^2$)	L (H. cm^2)	CPE-Y_0 X 10^{-4} ($\Omega^{-1}.cm^{-2}s^n$)	n	χ^2 X 10^{-4}
Fe-700	63.3 ± 9.5	307.7 ± 85.6	880.5 ± 112.6	194.4 ± 34.01	1.786 ± 0.667	0.827 ± 0.015	3.7 ± 1.4
Fe-950	52.5 ± 5.9	209.5 ± 23.4	645.4 ± 111.4	92.9 ± 24.6	1.987 ± 0.338	0.817 ± 0.008	3.9 ± 0.7
Fe-1100	53.5 ± 4.8	457.8 ± 125.1	1182.1 ± 246.5	431.3 ± 283.1	1.290 ± 0.524	0.819 ± 0.032	6.4 ± 3.2

4.3. Surface characterization

The corrosion morphology observed in section 4.2.3 is pursued further by analyzing the topography of the corroded surface of samples. Fig. 4.14 shows the optical images of the samples after the potentiostatic polarization experiment in 0.1 M H_2SO_4 solution. The images are a good representation of the sample surface during the early stages of the potentiodynamic polarization experiment. Here, the grain boundaries appear less attacked relative to that observed in fig. 4.7. Further, in all the samples, some grains appear bright while the rest appear dull. This indicates the preferential dissolution of grains, likely due to their own and their neighbors' crystallographic orientation.

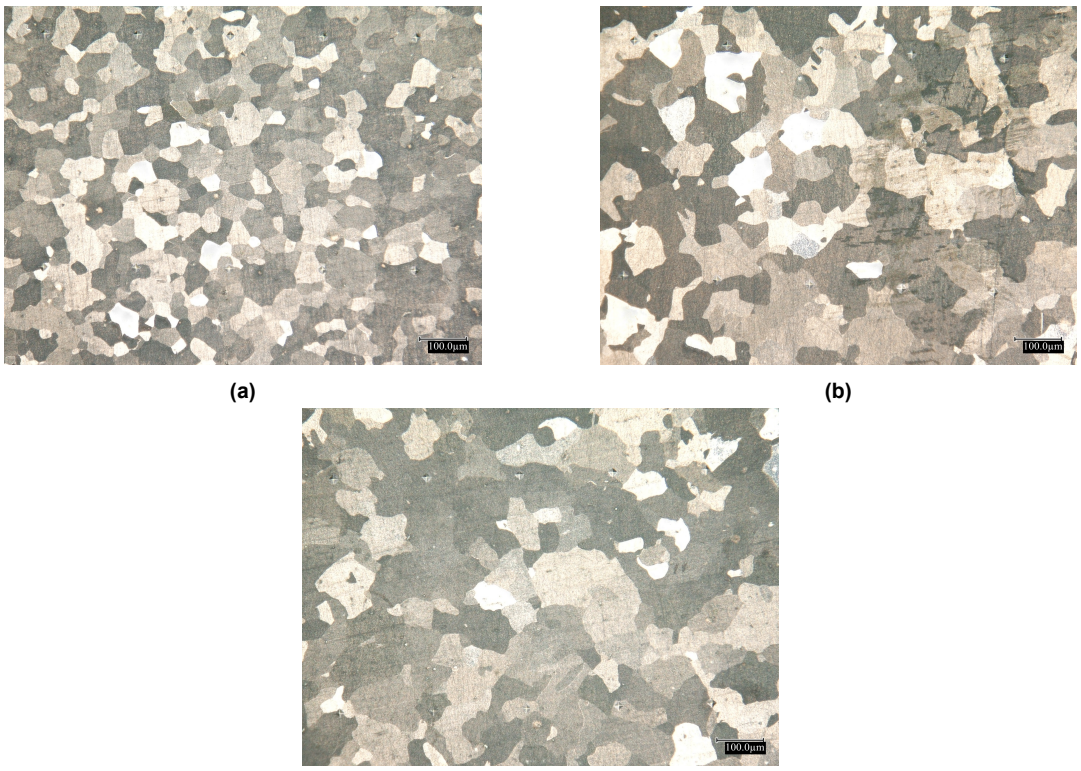

Figure 4.14: Optical images of (a) Fe-700 (b) Fe-950 and (c) Fe-1100 samples after potentiostatic poarization test in 0.1 M H_2SO_4 solution. (Magnification: 500X)

The AFM scans reveal interesting features observed in the surface topography of the samples. Fig. 4.15 show a high-resolution AFM scan on the Fe-700 sample surface and the line profile scans conducted across the grain boundary. The grain boundaries are distinctly visible. A striking difference is observed in the surface texture of grains. The grain on the left appears rougher with undulations, while the grain on the right looks relatively smooth. These observations are evident in the line profile scans. A step-like feature is observed at the grain boundary. The step height is about 230 nm in profile-1 and about 190 nm in profile-2. This shows anisotropy in the dissolution of grains during corrosion. The height variations within the grain are attributed to the inherent roughness of the surface and the possible presence of corrosion products and oxides of iron.

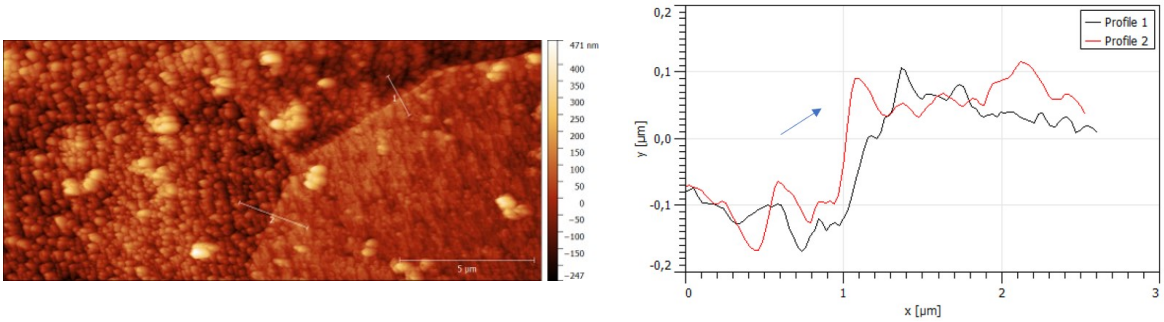

Figure 4.15: AFM topography of a region on corroded Fe-700 sample surface and the line profile scans across grain boundary (x- position, y- depth/height).

Fig. 4.16 and 4.17 shows small region AFM scans near the grain boundary in the Fe-700 sample with the line profile scans. The line profiles show contrasting topography at the grain boundaries. In fig. 4.16, the grain boundary appears as a peak while in fig. 4.17, it appears like a valley. Fig. 4.18 shows an AFM image of another region in the Fe-700 sample and the line profile scans. Here, Profile-1 and profile-2 show a step-like topography across the grain boundary, while profile-3 shows a wall-like topography at the grain boundary with the grains at a lower level on both sides of the wall. The wall height is about 160 nm and has a width of about 1 µm.

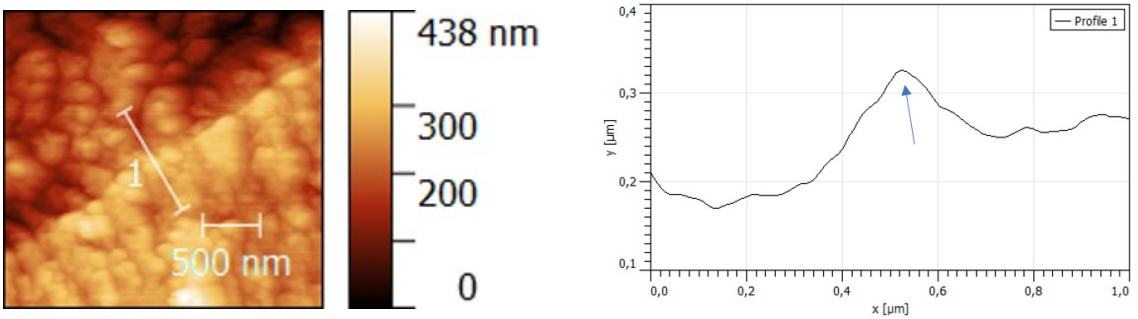

Figure 4.16: AFM topography of a small region near grain boundary on corroded Fe-700 sample surface and the line profile scan (x- position, y- depth/height).

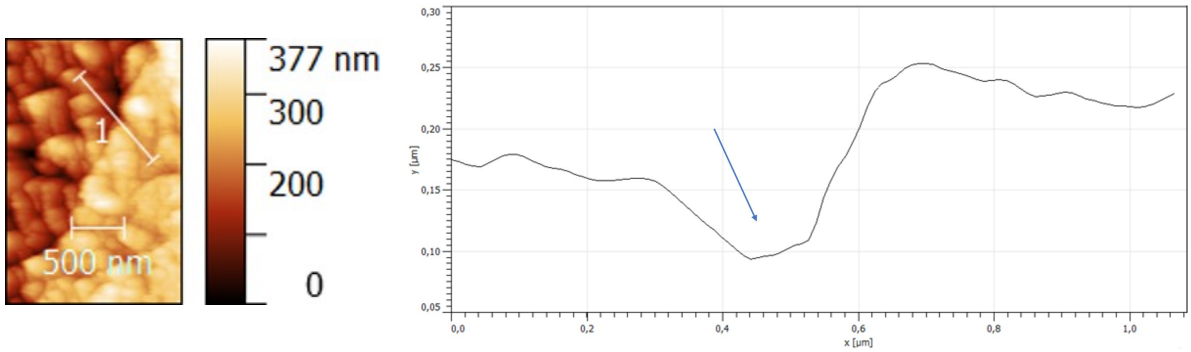

Figure 4.17: AFM topography of a small region near grain boundary on corroded Fe-700 sample surface and the line profile scan (x- position, y- depth/height)

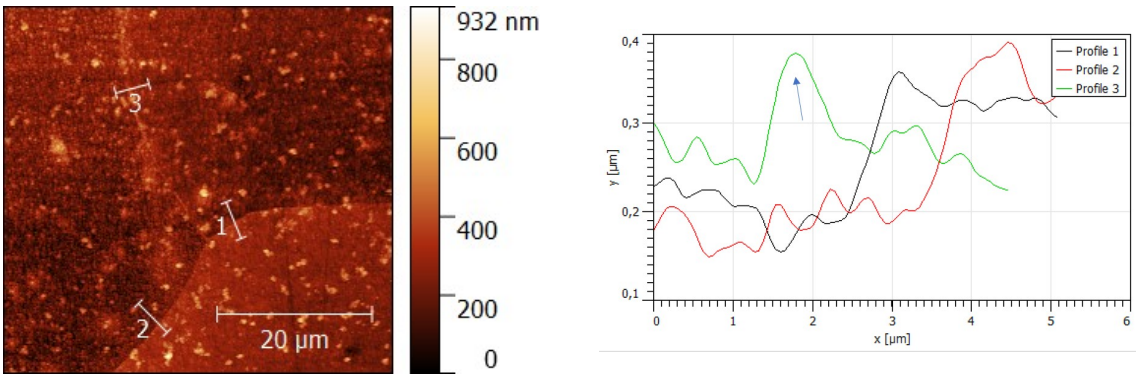

Figure 4.18: AFM topography of another region on corroded Fe-700 sample surface and the line profile scans across grain boundary (x- position, y- depth/height).

Fig. 4.19 shows the AFM scan image of a region in the Fe-950 sample and the line profile scans across the grain boundary. The line profiles show a sharp drop in height at the grain boundaries, which gives rise to a trench-like topography. The depth of the trench is about 160 nm in profile-1 and about 230 nm in profile-2. Fig. 4.20 shows the AFM scan of a region in the Fe-1100 sample. Profile-1 and Profile-2 show do not show any distinguishable difference across the grain boundary. Profile-3 shows a trench like topography with a depth of nearly 200 nm across the grain boundary.

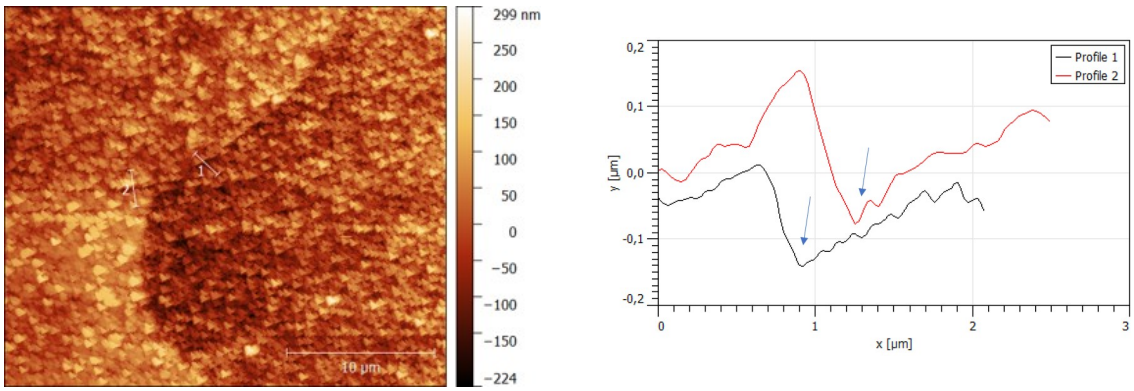

Figure 4.19: AFM topography of corroded Fe-950 sample surface and the line profile scan across grain boundary (x- position, y- depth/height).

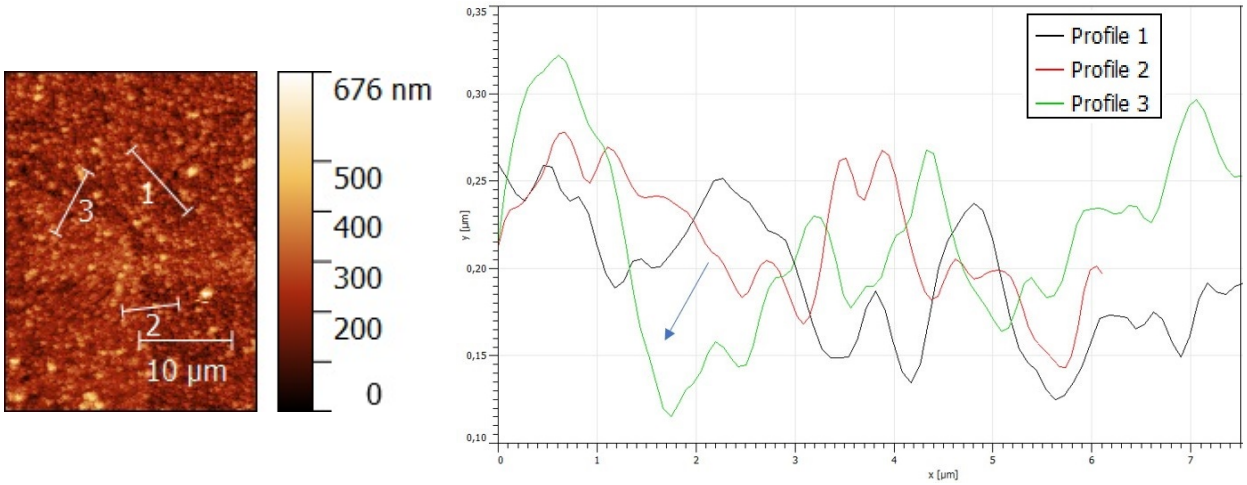

Figure 4.20: AFM topography of corroded Fe-1100 sample surface and the line profile scan across grain boundary (x- position, y- depth/height).

It is important not to jump to conclusions by correlating the observed features individually to their corresponding sample. The AFM scans represent only a small region of the sample. It is reasonably possible to obtain all the topographies within the same sample. Hence, the origin of such features is analyzed, irrespective of the sample. In the current study, the topography across the grain boundary could be described by shapes like step, wall, and trench. These observations have been addressed in other research works [52, 100, 101] and highlighted in the literature review section 2.3.2. The step geometry is associated with neighboring grains having a large difference in their corrosion behavior. A good example is the neighboring combination of (001) and (110) orientation grains of iron studied by Schreiber et al. [52]. The (001) grain corrodes faster than (110), resulting in a step topography at the grain boundary. The formation of a wall and trench-like topographies is associated with neighbor grains of similar

orientation or orientations with similar corrosion rates. The corrosion behavior of grain boundary relative to its neighboring grains is likely to be the underlying factor. However, the exact cause behind the appearance of either topography is not quite apparent because the corrosion behavior of grain boundaries can vary depending on the grain boundary energy.

4.4. Numerical corrosion modeling

4.4.1. Preliminary model results

Using the 2-D model geometry for a bi-crystal sample, the polarization curves of 3 different bi-crystal systems viz. (1 1 12) – (10 9 11), (1 1 12) – (1 0 1) and (10 9 11) – (1 0 1) are modeled. These systems closely represent (0 0 1) – (1 1 1), (0 0 1) – (1 0 1) and (1 1 1) – (1 0 1) systems respectively.The model geometry is presented here again for convenience (fig. 4.21). For bi-crystal study, the electrochemical interface (blue line) is divided in ratio 1:1 to assign the electrochemical properties of the two crystal orientations taken from fig. 3.13.

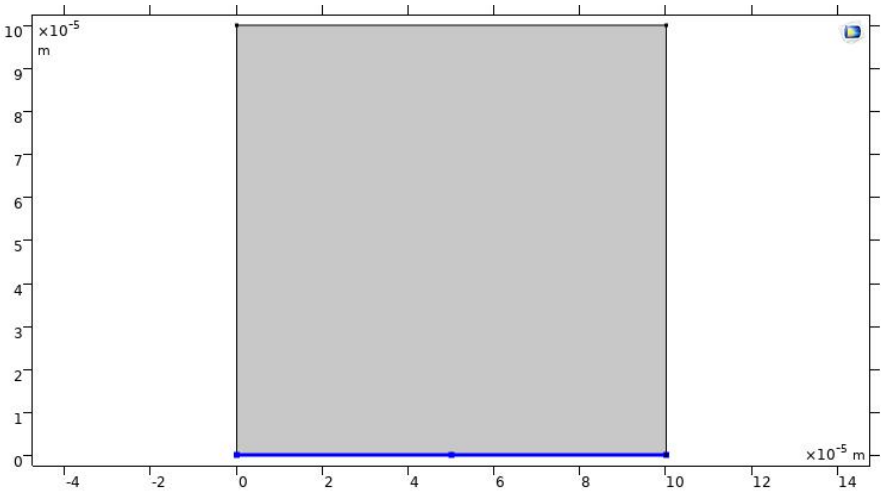

Figure 4.21: Illustration of model geometry for bi-crystal study.

Fig. 4.22 shows the modeled polarization curves for the three different bi-crystal systems along with the contributing individual polarization curves. The modeled curves clearly capture the role of the cathodic hydrogen evolution reaction (HER) controlling the corrosion kinetics. The different crystallographic orientations show significant shifts in the cathodic branch of the polarization curve. The role of cathodic reaction is also observed in the current experimental work. Fe-950 sample (with higher corrosion rate) showed higher cathodic current density than Fe-700 and Fe-950 samples. The E_{corr} and i_{corr} values of the different systems, obtained by Tafel extrapolation, are summarized in table 4.8. The (1 1 12) – (10 9 11) and (1 1 12) – (1 0 1) systems show similar corrosion current density and higher than (10 9 11) – (1 0 1) system. This is attributed to the faster HER kinetics on (1 1 12) contributing to higher corrosion current density in those two systems. The modeled polarization curves of individual orientations are validated with the experimental counterparts from the work of Fushimi et al. [51]. This is shown in fig. 4.23 for the three orientations discussed here. The range of the axes are kept the same for better comparison. The modeled polarization curves bear close similarity with the experimental curves.

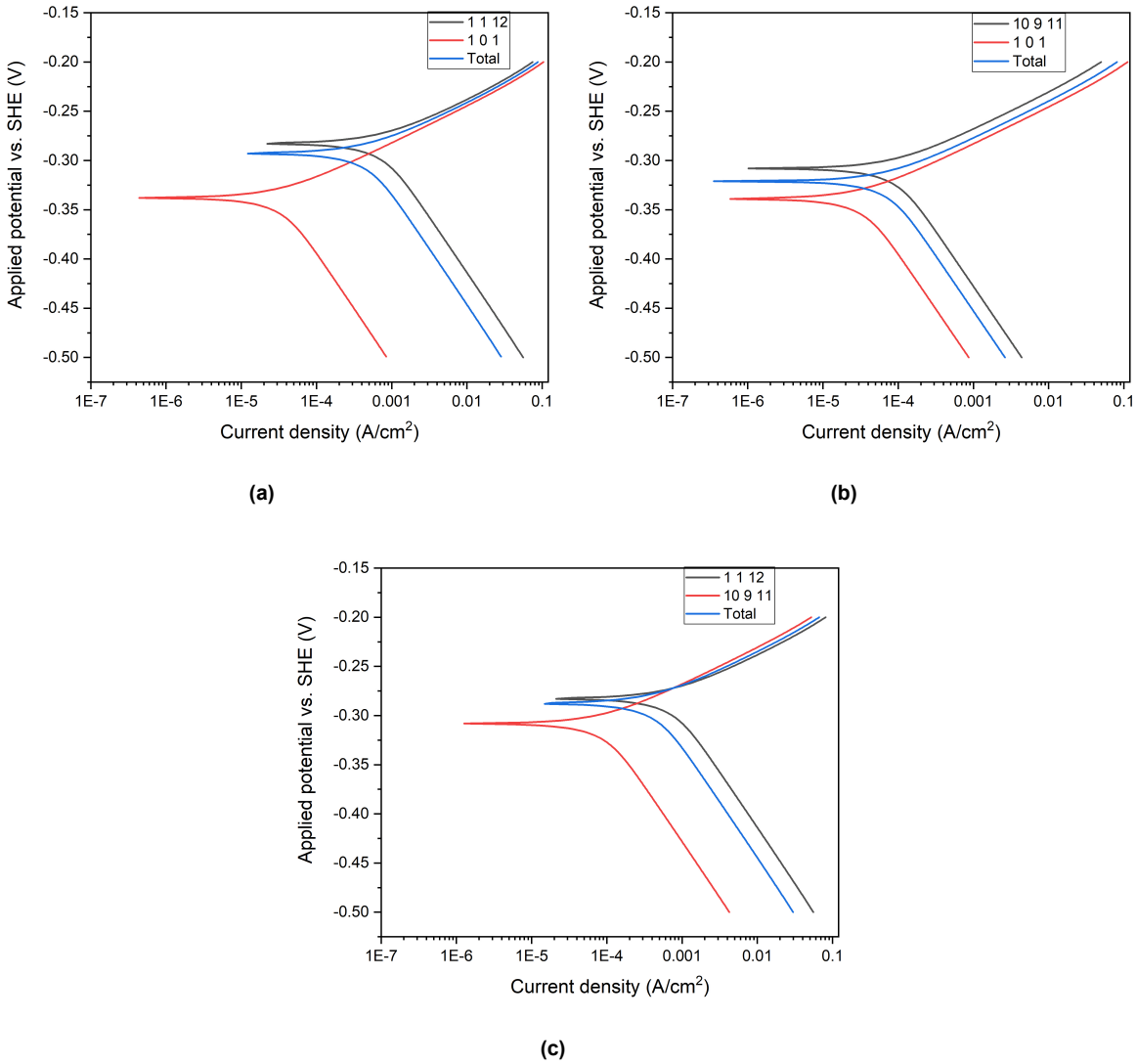

Figure 4.22: Modeled polarization curves of the bi-crystal systems (a) (1 1 12)-(101) (b) (10 9 11)-(101) and (c) (1 1 12)-(10 9 11)

Table 4.8: Summary of electrochemical parameters obtained by Tafel extrapolation of the modeled bi-crystal systems.

System	E_{corr} vs. SHE (V)	i_{corr} (A/cm^2)
(1 1 12)-(101)	-0.297	4.56×10^{-4}
(10 9 11)-(101)	-0.323	6.96×10^{-5}
(1 1 12)-(10 9 11)	-0.291	4.41×10^{-4}

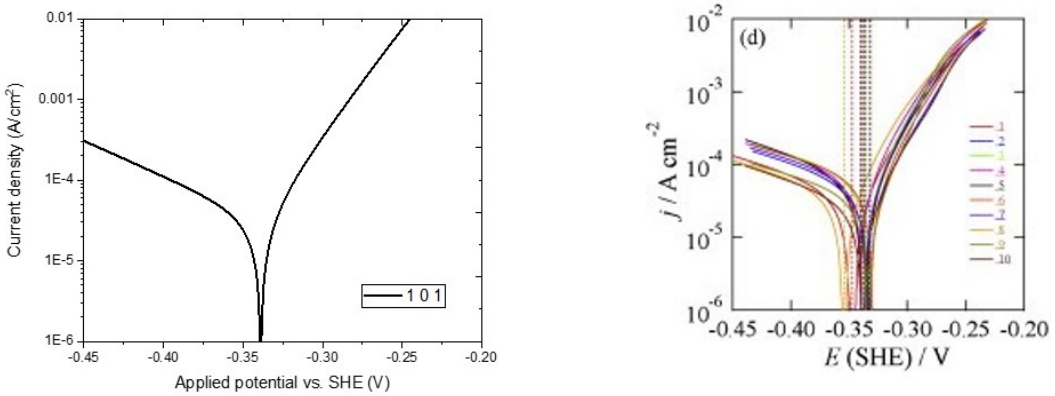

(a)

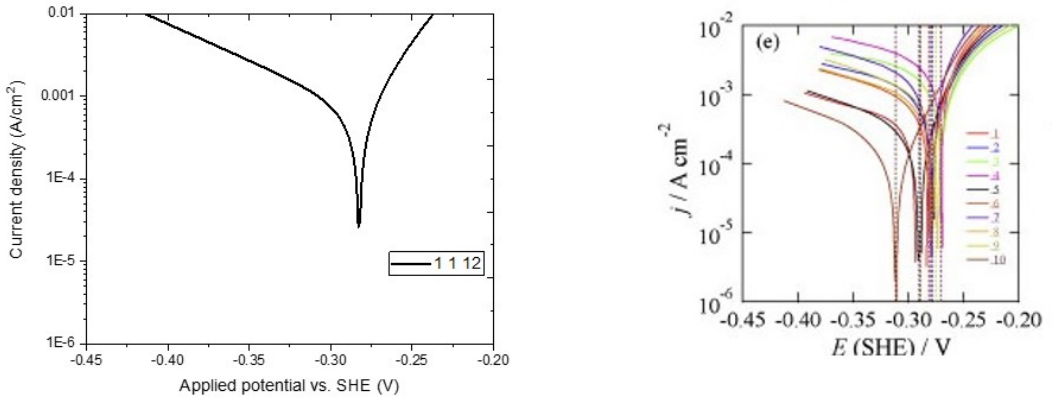

(b)

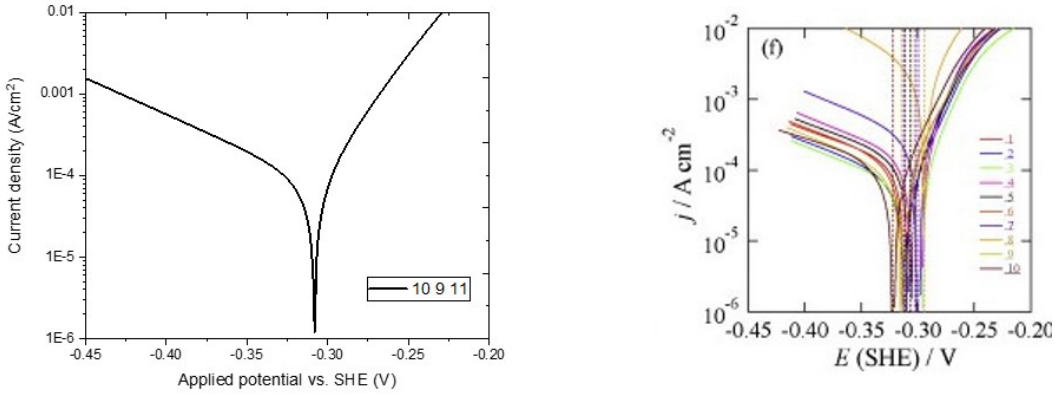

(c)

Figure 4.23: Validation of modeled polarization curves(left) of (a) (101), (b) (1 1 12), and (c) (10 9 11) orientations with their corresponding experimental polarization curves (right) from the work of Fushimi et al. [51]

4.4.2. Model results of samples

Based on successful validation, the model is extended to the current samples, albeit with some limitations and assumptions. There is a lack of complete understanding of corrosion on different crystallographic orientations in general. Most of the experimental work on iron are limited

to the basic three low index crystallographic orientations and in passive condition (table 2.3). The current work shows the significance of HER kinetics on the corrosion behavior of iron. A deeper literature analysis shows a lack of consensus about the underlying physical phenomenon controlling the HER kinetics on the electrode surface. Some of the proposed factors are work function and hydrogen adsorption free energy associated with the surface [102, 103]. These factors do not follow a monotonous behavior with change in atomic packing fraction, an easily measurable physical property. This makes it difficult to define a relationship between HER kinetics and crystallographic orientation [104]. Further, from fig. 3.13, it is observed that the scatter associated with corrosion rate of different crystallographic orientations shows quite some overlap.

Hence, to simplify the current study, only three orientations ((0 0 1), (1 1 1), and (1 0 1)) are taken into consideration. The corrosion parameters for (0 0 1) and (1 1 1) orientations are assumed to be same as that of (1 1 12) and (10 9 11) respectively. Now, in the EBSD maps of the samples (fig. 4.2), it is assumed that a grain behaves (in terms of corrosion behavior) as one of the mentioned three crystal orientations based on its relative proximity to these orientations. The EBSD maps of the samples are used to calculate area fractions of '(001)' like, '(111)' like and '(101)' like grains. This classification is done by using the RGB color code employed in the EBSD image to set color threshold. A detailed explanation of this step is added in the appendix A3. The computed area fractions on EBSD images of the samples are summarized in table 4.9. These values are used as input for the ratio to divide the electrochemical interface into three parts in the 2-D model geometry. The modeled polarization curves of the samples are shown in fig. 4.24.

Table 4.9: Summary of the calculated area fractions from the EBSD maps of the samples.

Sample	(001) area fraction	(101) area fraction	(111) area fraction
Fe-700	0.234	0.188	0.578
Fe-950	0.368	0.198	0.434
Fe-1100	0.347	0.325	0.328

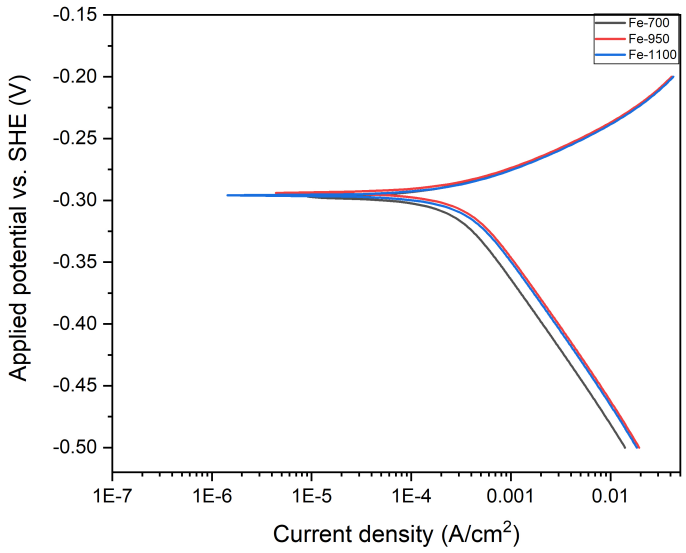

Figure 4.24: Modeled polarization curves of the three samples.

The cathodic current density of the Fe-700 sample is lower than the Fe-950 and Fe-1100 samples in the range of applied potential. The polarization curves of Fe-950 and Fe-1100 samples overlap mostly. The corrosion parameters obtained by Tafel extrapolation are presented in the table 4.10. The Fe-700 sample has the lowest corrosion density among the samples. It supports the observation from the experiments in 0.1 M H_2SO_4 solution regarding the Fe-700 sample. In the model, Fe-950 and Fe-1100 samples have similar corrosion rates. It is not in accord with the experimental observations. The possible cause can be linked to the model's limitation to incorporate the effect of grain boundaries and less statistical representation of microstructure in the model for Fe-950 and Fe-1100 sample due to fewer grains in the EBSD map.

Table 4.10: Summary of electrochemical parameters obtained by Tafel extrapolation of modeled polarization curves of the samples.

Sample	E_{corr} vs. SHE (V)	i_{corr} x 10^{-4} (A/cm^2)
Fe-700	-0.295	2.06
Fe-950	-0.291	2.95
Fe-1100	-0.294	3.07

4.5. Discussion

In the current research work, the effect of grain size on the corrosion behavior of pure Fe in active condition is studied by performing extensive microstructure and electrochemical characterization of the samples. Following the heat-treatment, the microstructure characterization reveals the expected variation in the grain size of the samples. The EBSD results show similar values of geometrically necessary dislocation density and a significant fraction of high angle grain boundaries across the samples. The XRD texture analysis shows a distinct variation in the fractions of crystallographic orientation of grains in the samples. Fe- 700 sample has a significant volume fraction of grains oriented close to {111} orientation parallel to the rolled surface. Fe-950 sample has a high fraction of grains close to {110} and {001} orientations parallel to the rolled surface while Fe-1100 sample has a high fraction of grains close to {110} orientation. Both Fe-950 and Fe-1100 samples have a good fraction of grains with intermediate orientations. The difference in the orientation distribution of grains among samples could be linked with the underlying phenomenon occurring during annealing heat treatment [50, 105]. Fe-700 sample undergoes recrystallization while Fe-950 and Fe-1100 samples undergo phase transformation from ferrite to austenite and then back to ferrite during the heat treatment. The corrosion rates vary with crystallographic orientations of grains. The sequence of corrosion rates of different crystallographic orientations is dependent on the environment. In the active condition, the corrosion response is governed by the resistance of material to undergo dissolution. In contrast, in passive conditions, the corrosion resistance depends on the stability and protective nature of the passive film formed. From the literature, the corrosion rate follows the sequence (110) < (111) < (001) for iron in active condition [51, 103]. This sequence is relevant for the current study because the electrochemical experiments are performed in active condition.

The electrochemical characterization is done using a combination of techniques like potentio-

dynamic polarization (PDP) and electrochemical impedance spectroscopy (EIS). In the 0.1 M H_2SO_4 solution, the results indicate that the corrosion rate does not follow a clear trend with grain size. The corrosion rate increases from Fe-1100 to Fe-950 sample and then decreases from Fe-950 to Fe-700 sample. The unexpected decrease of the corrosion rate in the Fe-700 sample is attributed to the dominant role of crystallographic texture in its corrosion behavior. In the 0.01 M H_2SO_4 solution, the results show the same trend in the corrosion rate as in 0.1 M H_2SO_4 solution. However, the dilution of the corrosion medium helps to elucidate the complex role of grain size and crystallographic orientations in determining the overall corrosion rate. Both Fe-700 and Fe-950 samples show a higher corrosion rate than the Fe-1100 sample in the 0.01 M H_2SO_4 solution. In the Fe-950 sample, the finer grain size and presence of a good volume fraction of grains with {001} orientation supplement each other to achieve a high increase in corrosion rate. However, in case of Fe-700 sample, the opposing effects of finer grain size and grains with predominant {111} orientation on the corrosion behavior results in a relatively smaller increase in corrosion rate than the Fe-950 sample. The results of EIS and PDP agree with each other. The change in corrosion rate with crystallographic orientations of iron in active condition is linked to the cathodic hydrogen evolution reaction (HER) kinetics on the orientations [51, 103]. The role of HER kinetics is also evident in the potentiodynamic polarization plots of the samples. Fe-950 sample shows higher cathodic current density than Fe-1100 and Fe-700 samples. The underlying factor controlling the HER kinetics on the metal surface is debatable. Extensive studies have been performed on HER kinetics in pure metals like Pt [106] and Au [107] for electrocatalysis and orientation-dependent HER kinetics have been observed. In case of Pt, the HER kinetics follow the sequence (111) < (001) < (110) and in case of Au, the HER kinetics follow the sequence (110) < (001) < (111). Multiple reasons have been proposed to be detrimental like the work function of the surface, hydrogen adsorption free energy, and surface coverage of hydrogen [102, 107–109]. The studies conducted by Fushimi et al. [51] in pure iron and Yule et al. [103] by scanning electrochemical cell microscopy (SECCM) in low carbon steel reveal the same sequence of HER kinetics, i.e., (110) < (111) < (001). However, they attribute different reasons behind their observation. Fushimi et al. [51] link their results to the decomposed d-valence charge on the orientations, while Yule et al. [103] link their results to hydrogen adsorption free energy. The studies exploring the HER kinetics in iron and its alloys are limited in literature and require more attention since it has been found to play a significant role in the current work.

The surface characterization of the corroded sample by AFM shows the variations in topography across the grain boundary in the form of wall, trench and step. The non-uniform topography arises primarily due to the difference in corrosion behavior of grain relative to its surrounding grains or grain boundaries [52, 100, 101]. A step-like feature appears at the grain boundary when there is a preferential dissolution of grain relative to its neighboring grain. It arises due to a large difference in the corrosion rates of neighboring grains. Wall and trench-like features emerge when neighboring grains have similar corrosion rates, and the grain boundary between them has a lower or higher corrosion rate [52].

A numerical corrosion model is developed in COMSOL® to predict the corrosion behavior of the samples. The EBSD maps of the samples provide the microstructure input. The corrosion behavior of three crystallographic orientations is considered. The model is simplified and limited due to the lack of experimental data and complete understanding of corrosion behavior on different crystallographic orientations. Nevertheless, the model can single out the Fe-700 sample with the least corrosion rate among the three samples. This is possible due to the dominance of crystallographic texture on the corrosion behavior of the Fe-700 sample. The model predicts similar corrosion rates for Fe-950 and Fe-1100 samples. This is likely due to the limitation of the model to incorporate the effect of grain boundaries. Larger area EBSD

scans of Fe-950 and Fe-1100 samples could have helped to do a better representation of the microstructure in the model. The model at its present state shows the gaps in the current knowledge that can be overcome with more experiments. Localized electrochemical experiments on different orientations of various metals combined with DFT calculations can help to narrow down the underlying phenomenon behind the orientation-dependent corrosion behavior.

The findings of the study relate well to the literature. Wang et al. [12, 13] reported an improvement in the active corrosion resistance of nanocrystalline Fe sample relative to the conventional polycrystalline Fe sample in acidic sulfate and 1 M HCl mediums individually. They attributed their observations to {110} crystallographic texture in the nanocrystalline sample. Jinlong et al. [14] also reported an improvement in corrosion resistance of the cold-rolled sample relative to the annealed sample in 0.5 M H_2SO_4 solution and emphasized the role of cathodic hydrogen evolution reaction kinetics in active corrosion. The conclusions about the role of crystallographic texture and cathodic reaction kinetics are evident in the present study as well. However, the link between the two observations is missing in the mentioned research works. Studies by Fushimi et al. [51] and Yule et al. [103] establish the link between HER kinetics and crystallographic orientation, which helps in a coherent interpretation of the results, as discussed earlier in the section. The present work uniquely helps to visualize the combined effect of grain size and crystallographic orientation of grains in the overall corrosion behavior of the samples. This is achieved by:

- Using a range of grain size instead of two samples with ‘coarse’ and ‘fine’ grains.
- Performing corrosion experiments in concentrated and diluted acid solutions.
- Doing a comprehensive microstructure-corrosion property correlation.

Finally, the answer to the research question posed in the work is not straight-forward. The results in the 0.01 M H_2SO_4 solution do show that there is an increase in the corrosion rate with a reduction in the grain size relative to the Fe-1100 sample. However, the extent of increase solely from the change in grain size is not apparent. The research hypothesis presented at the beginning of the work is valid in principle, but not adequate to capture all the observations of the experiments. The complexity arises because the crystallographic orientation of grains is found to be more prominent than the grain size in determining the corrosion behavior. A controlled material processing that ensures random orientation of grains while changing grain size can be useful to study the true effect of grain size on the corrosion behavior.

5

Conclusion and Recommendation

5.1. Conclusion

Based on the findings in the current research work, the following conclusions are drawn:

- The electrochemical characterization of the samples show that the corrosion rate does not follow a clear trend with grain size. The results show that the corrosion rate first increases and then decreases with reduction in grain size.The combined effect of grain size and crystallographic orientation on the corrosion behavior is the underlying cause.
- The surface characterization of the corroded samples by AFM reveals step, wall and trench-like topography across the grain boundary based on the interplay of corrosion behavior of grains and grain boundaries.
- The corrosion model, with its limitations and assumptions successfully predicts Fe-700 sample with the least corrosion rate, same as that observed in the 0.1 M H_2SO_4 experiments. This is possible due to the dominance of crystallographic texture on the corrosion behavior. The model predicts Fe-950 and Fe-1100 with similar corrosion rates, contrary to the experimental results. A larger area EBSD scan of these samples might have helped in better prediction. The corrosion modeling exercise reveals the gap in the current understanding of corrosion behavior of different crystallographic orientations in active condition. This information can be used to improve the model.
- The findings do not agree completely with the expected outcome based on the research hypothesis proposed in chapter 1. It highlights the practical complexity of studying the corrosion contribution of each microstructural feature individually. This hurdle can be overcome with improved understanding of the processing-microstructure relationship and by performing localized corrosion experiments on the sample.

5.2. Recommendation

The observations of current research work provide some interesting start points for conducting further research.

- The impedance spectroscopy results show the presence of adsorbed species on the surface. The role of these species can be explored further by studying the evolution of EIS results with immersion time. The chemical nature of these adsorbed species can be determined using suitable technique.

- Based on the observations in the model and experiments, it is worthwhile to perform localized electrochemical experiments on individual orientations and combine with DFT calculations to understand the underlying physical property that results in the variation of active corrosion behavior in different crystallographic orientations.
- Texture is observed in the current work to be play a role in the corrosion behavior. Since the texture is dependent on the processing technique, it is worthwhile to investigate the possible textures arising from different processing techniques. This can help in better design of controlled experiments.
- The corrosion studies can be performed in passive condition to understand the relation between passivity and microstructure.

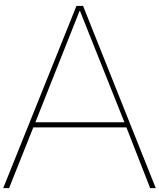

Appendix

A.1. Preparation of the solutions for corrosion tests

A.1.1. 0.1 M H_2S0_4

Calculation

H_2S0_4 molar mass = 98.08 g/mol
H_2S0_4 density = 1.84 g/ml
Concentration of stock solution = 95% w/w
Amount of stock solution needed to prepare 1000 ml of 0.1 M H_2S0_4 solution =
(0.1 x 98.08)/ (1.84 x 0.95) = 5.611 ml of stock solution

Procedure

1. About 500 ml of distilled water is taken in a 1000 ml volumetric flask.
2. Now, a measuring pipette fitted with a pipette bulb is used for pipetting out precisely 5.6 ml of sulfuric acid (Honeywell Fluka Sulfuric acid, 95 wt.% purity, CAS:7664-93-9) into the volumetric flask.
3. The flask is filled with more distilled water until the 1000 ml mark.
4. The prepared solution is transferred into a glass bottle using a funnel.

A.1.2. 0.01 M H_2S0_4

Calculation

Based on the formula for dilution of solutions M1 V1 = M2 V2; M1 and V1 are the molarity and volume of the solution before dilution respectively. Similarly, M2 and V2 are the molarity and volume of solution after dilution.
Here, M1= 0.1 M, M2 = 0.01 M, V2 = 1000 ml. So, V1 = 100 ml

Procedure

1. About 500 ml of distilled water is taken in a 1000 ml volumetric flask.
2. N2. Now, 100ml of 0.1 M H_2S0_4 is pipetted into a 100 ml volumetric flask. The acid is then emptied into the volumetric flask containing the distilled water.
3. The flask is filled with more distilled water until the 1000 ml mark.
4. The prepared solution is transferred into a glass bottle using a funnel.

A.1.3. pH measurement

The pH of the prepared solutions is measured before using it for experiments to ensure consistency in results. During the course of the experiments, the solutions were prepared 2-3 times. The pH values of the solutions recorded using InoLab pH7110 pH meter are summarized in table A.1.

Table A.1: Summary of the pH of the synthesized solutions

pH 0.1 M H_2S0_4	pH 0.01 M H_2S0_4
1.061	1.925
1.087	1.980
1.032	-

A.2. Optical images used for grain size calculation

A.2.1. Fe-700

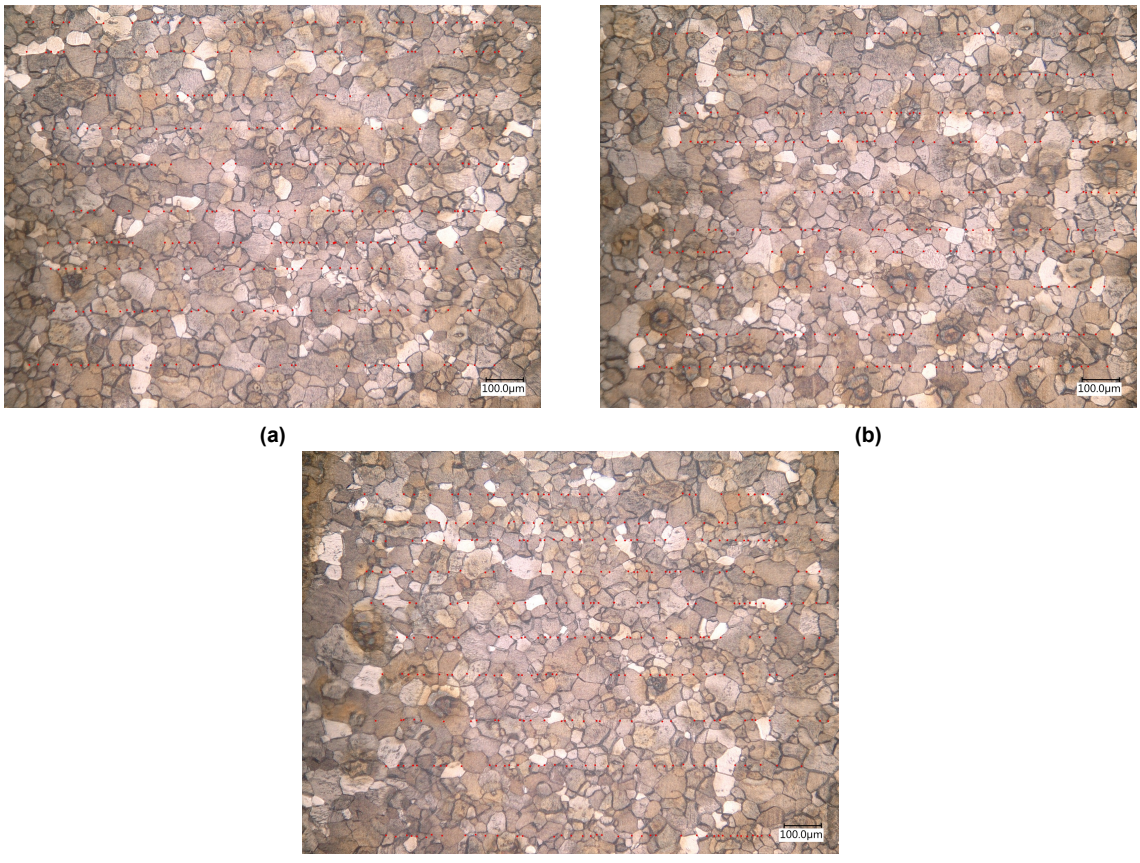

(a) (b)

(c)

Figure A.1: Optical images after potentiodynamic polarization in 0.1 M H_2SO_4 solution. (Magnification: 250X)

A.2.2. Fe-950

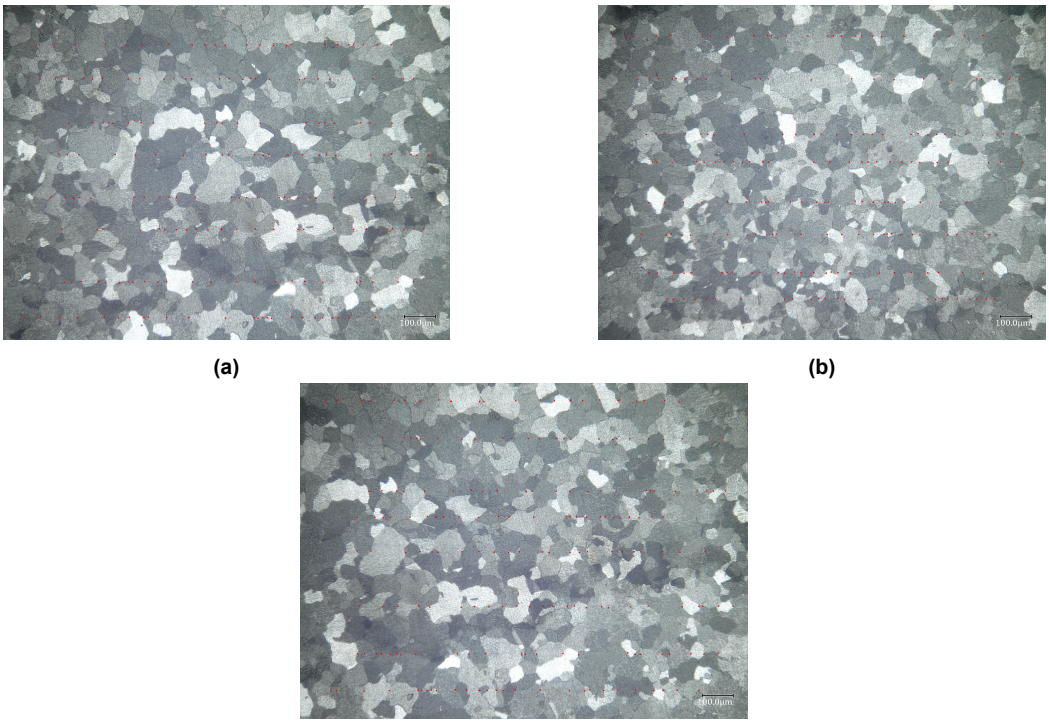

(a) (b)

(c)

Figure A.2: Optical images after potentiodynamic polarization in 0.1 M H_2SO_4 solution. (Magnification: 250X)

A.2.3. Fe-1100

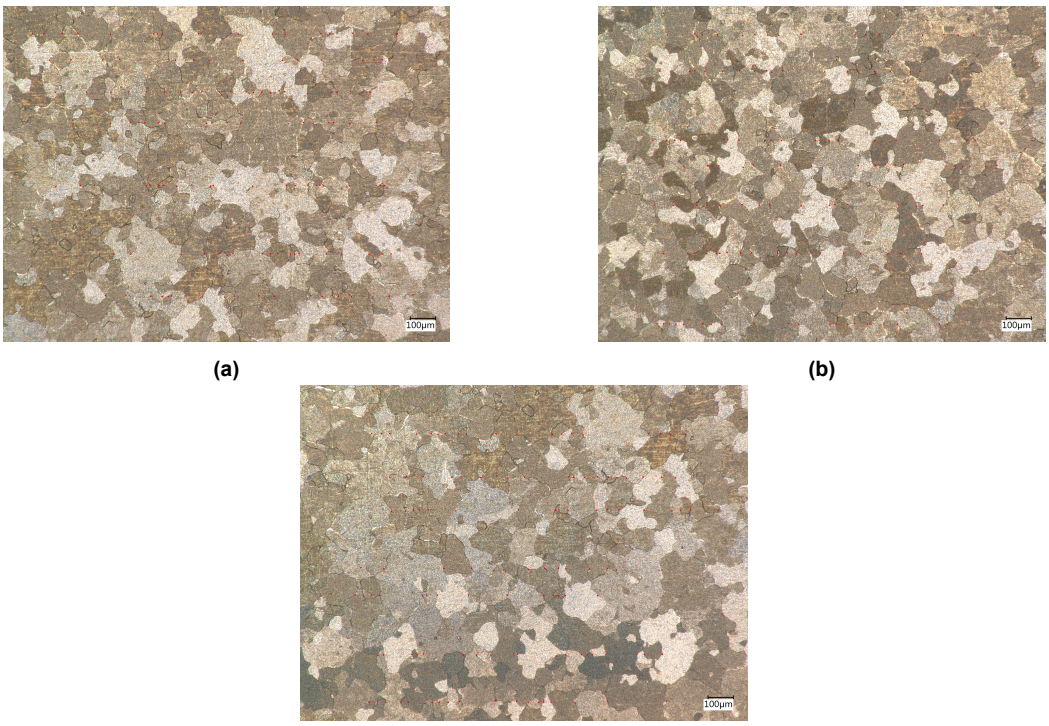

(a) (b)

(c)

Figure A.3: Optical images after potentiodynamic polarization in 0.1 M H_2SO_4 solution. (Magnification: 200X)

A.3. Steps followed to calculate area fraction of orientations from the EBSD maps

The section gives a detailed summary of steps followed to assign grain orientations as '(100)' like, '(111)' like and '(101)' like for use in the corrosion model.

Principle

The EBSD map uses a RGB color code to assign different orientations based on the misorientation with the three main orientations. The EBSD plot legend is shown in fig. A.4. Red -(001), Green - (101), Blue - (111).

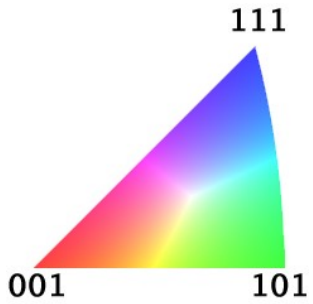

Figure A.4: EBSD plot legend.

Steps

- The EBSD map is imported in ImageJ software. The software recognizes this image as RGB code type image. On each grain, the software recognizes a (R, G, B) coordinate (fig. A.5).The scale on R, G or B has a maximum value of 255 and minimum value 0.

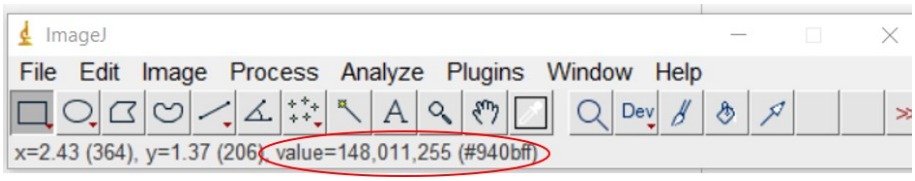

Figure A.5: Snapshot from ImageJ software.

- The EBSD image with RGB code is converted into RGB Stack. The RGB stack generates three 8-bit images each focusing on R, G and B respectively.Each of this 8-bit image uses a grey scale from 0 (black) to 255 (white).The white regions are the ones with maximum dominance of each color.This is illustrated in fig.A.6.

- Each of this 8-bit image is subjected to color threshold with both maximum and minimum threshold set as 255. The purpose is to select the white portions only, which represent maximum dominance of R, G or B respectively in the 3 8-bit images. This is illustrated in fig.A.7

- Now, the selected area is used to calculate the area fraction. This is done with the software.

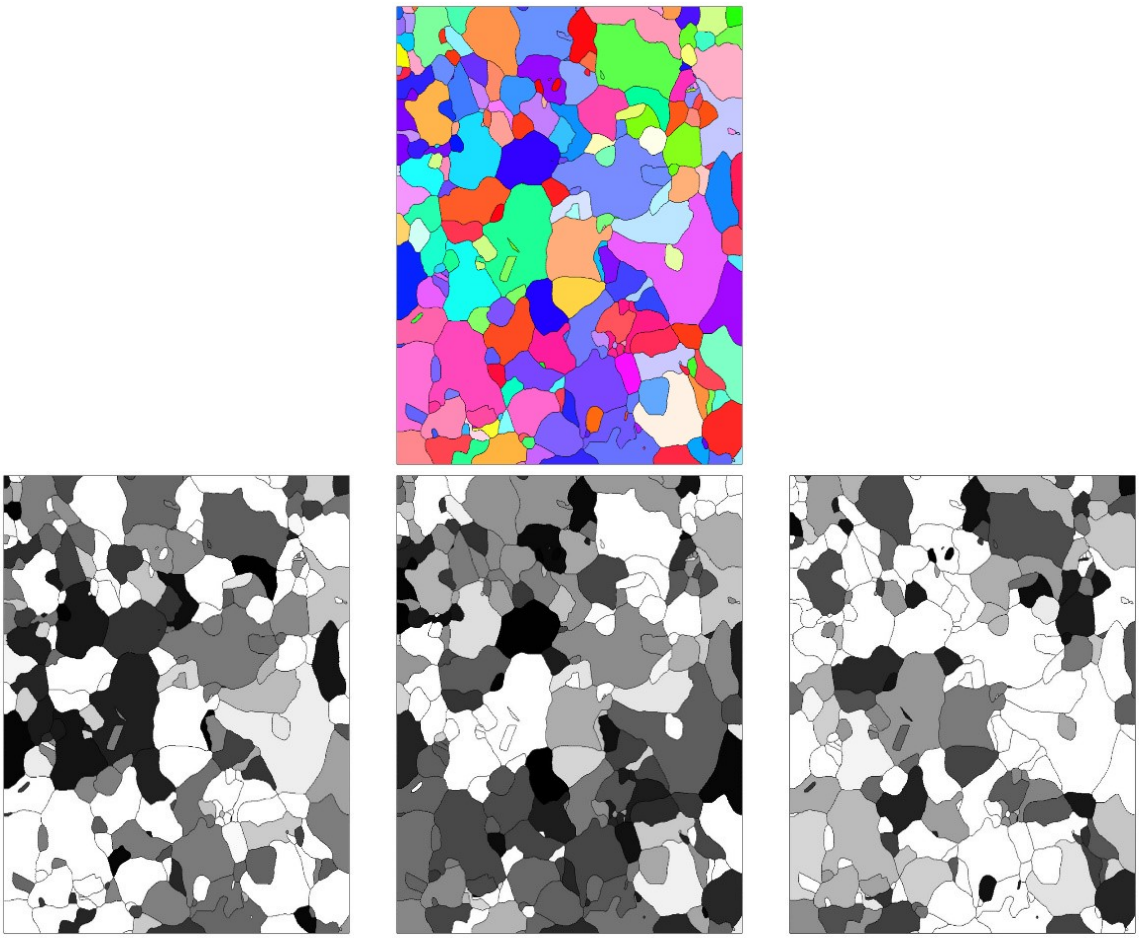

Figure A.6: Conversion of EBSD image using RGB stack tool to generate 8-bit images focusing on (a) Red (b) green and (c) blue components individually.

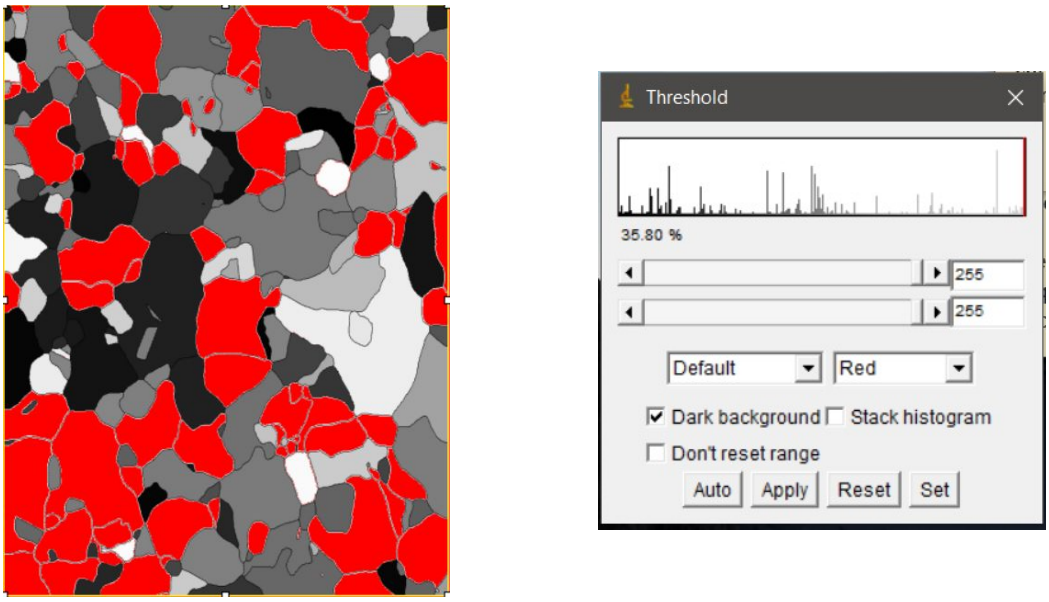

Figure A.7: Use of threshold on red 8-bit image.(Red colored region denotes the selected area by threshold.)

Bibliography

[1] G. Koch, J. Varney, N. Thompson, O. Moghissi, M. Gould, and J. Payer, *International Measures of Prevention, Application, and Economics of Corrosion Technologies Study*, Tech. Rep. (NACE International, 2016).

[2] K. D. Ralston and N. Birbilis, *Effect of grain size on corrosion: A review,* CORROSION **66**, 075005 (2010).

[3] J. M. Hyzak and I. M. Bernstein, *The role of microstructure on the strength and toughness of fully pearlitic steels,* Metallurgical Transactions A **7**, 1217 (1976).

[4] N. Hansen, *Hall–petch relation and boundary strengthening,* Scripta Materialia **51**, 801 (2004).

[5] Y. Li, A. J. Bushby, and D. J. Dunstan, *The hall-petch effect as a manifestation of the general size effect,* Proceedings of the Royal Society A: Mathematical, Physical and Engineering Sciences **472**, 20150890 (2016).

[6] S. Takaki, K. Kawasaki, and Y. Kimura, *Mechanical properties of ultra fine grained steels,* Journal of Materials Processing Technology **117**, 359 (2001).

[7] H. Miyamoto, M. Yuasa, M. Rifai, and H. Fujiwara, *Corrosion behavior of severely deformed pure and single-phase materials,* MATERIALS TRANSACTIONS **60**, 1243 (2019).

[8] T. Yamamoto, K. Fushimi, S. Miura, and H. Konno, *Influence of substrate dislocation on passivation of pure iron in pH 8.4 borate buffer solution,* Journal of The Electrochemical Society **157**, C231 (2010).

[9] K. Ralston, D. Fabijanic, and N. Birbilis, *Effect of grain size on corrosion of high purity aluminium,* Electrochimica Acta **56**, 1729 (2011).

[10] C. op't Hoog, N. Birbilis, and Y. Estrin, *Corrosion of pure mg as a function of grain size and processing route,* Advanced Engineering Materials **10**, 579 (2008).

[11] L. Lapeire, E. Martinez Lombardia, I. De Graeve, H. Terryn, and K. Verbeken, *Influence of grain size on the electrochemical behavior of pure copper,* Journal of Materials Science **52**, 1501 (2017).

[12] S. G. Wang, C. B. Shen, K. Long, T. Zhang, F. H. Wang, and Z. D. Zhang, *The electrochemical corrosion of bulk nanocrystalline ingot iron in acidic sulfate solution,* The Journal of Physical Chemistry B **110**, 377 (2006).

[13] S. G. Wang, C. B. Shen, K. Long, H. Y. Yang, F. H. Wang, and Z. D. Zhang, *Preparation and electrochemical corrosion behavior of bulk nanocrystalline ingot iron in hcl acid solution,* The Journal of Physical Chemistry B **109**, 2499 (2005).

[14] L. Jinlong and L. Hongyun, *The effects of cold rolling temperature on corrosion resistance of pure iron,* Applied Surface Science **317**, 125 (2014).

[15] L. Y. Zhang, A. B. Ma, J. H. Jiang, H. S. Wu, and H. B. Yu, *Effect of equal-channel angular pressing passes on corrosion behavior of ultrafine-grained pure iron,* in *Advances in Materials and Materials Processing V*, Advanced Materials Research, Vol. 1095 (Trans Tech Publications Ltd, 2015) pp. 942–946.

[16] K. Heusler, D. Landolt, and S. Trasatti, *pac*, Vol. 61 (1989) Chap. Electrochemical corrosion nomenclature (Recommendations 1988), p. 19, 1.

[17] E. McCafferty, *Introduction to Corrosion Science* (Springer New York, 2010).

[18] B. N. Popov, *Chapter 5 - basics of corrosion measurements,* in *Corrosion Engineering*, edited by B. N. Popov (Elsevier, Amsterdam, 2015) pp. 181 – 237.

[19] R. Revie, *Passivity of Iron-A review* (2017) pp. 209–221.

[20] M. ichi Nagayama and M. Cohen, *The anodic oxidation of iron in a neutral solution,* Journal of The Electrochemical Society **109**, 781 (1962).

[21] A. J. Davenport, *In situ XANES study of galvanostatic reduction of the passive film on iron,* Journal of The Electrochemical Society **142**, 721 (1995).

[22] J. A. Bardwell, *Use of 18o/SIMS and electrochemical techniques to study the reduction and breakdown of passive oxide films on iron,* Journal of The Electrochemical Society **135**, 413 (1988).

[23] M. Seo, J. Lumsden, and R. Staehle, *Chemical shifts in the auger spectra of passive films,* Surface Science **42**, 337 (1974).

[24] N. Sato, K. Kudo, and T. Noda, *Single layer of the passive film on fe,* Corrosion Science **10**, 785 (1970).

[25] P. Schmuki, *In situ x-ray absorption near-edge spectroscopic study of the cathodic reduction of artificial iron oxide passive films,* Journal of The Electrochemical Society **143**, 574 (1996).

[26] R. W. Revie, *The passive film on iron: An application of auger electron spectroscopy,* Journal of The Electrochemical Society **122**, 1460 (1975).

[27] O. J. Murphy, *SIMS evidence concerning water in passive layers,* Journal of The Electrochemical Society **129**, 2149 (1982).

[28] D. Mitchell, G. Sproule, and M. Graham, *Measurement of hydroxyl ions in thin passive oxide films using secondary ion mass spectrometry,* Applications of Surface Science **21**, 199 (1985).

[29] I. Sieber, H. Hildebrand, S. Virtanen, and P. Schmuki, *Investigations on the passivity of iron in borate and phosphate buffers, ph 8.4,* Corrosion Science **48**, 3472 (2006).

[30] G. Long, J. Kruger, D. Black, and M. Kuriyama, *Structure of passive films on iron using a new surface-exafs technique,* Journal of Electroanalytical Chemistry and Interfacial Electrochemistry **150**, 603 (1983), electronic and Molecular Structure of Electrode-Electrolyte Interface.

[31] A. J. Davenport, *High resolution in situ XANES investigation of the nature of the passive film on iron in a pH 8.4 borate buffer,* Journal of The Electrochemical Society **142**, 725 (1995).

[32] A. J. Davenport, L. J. Oblonsky, M. P. Ryan, and M. F. Toney, *The structure of the passive film that forms on iron in aqueous environments,* Journal of The Electrochemical Society **147**, 2162 (2000).

[33] C. Y. Chao, *A point defect model for anodic passive films,* Journal of The Electrochemical Society **128**, 1187 (1981).

[34] D. D. Macdonald, *Steady-state passive films,* Journal of The Electrochemical Society **139**, 170 (1992).

[35] D. D. Macdonald, *The history of the point defect model for the passive state: A brief review of film growth aspects,* Electrochimica Acta **56**, 1761 (2011).

[36] V. Afshari and C. Dehghanian, *Effects of grain size on the electrochemical corrosion behaviour of electrodeposited nanocrystalline fe coatings in alkaline solution,* Corrosion Science **51**, 1844 (2009).

[37] C. S. Obayi, R. Tolouei, A. Mostavan, C. Paternoster, S. Turgeon, B. A. Okorie, D. O. Obikwelu, and D. Mantovani, *Effect of grain sizes on mechanical properties and biodegradation behavior of pure iron for cardiovascular stent application,* Biomatter **6**, e959874 (2016).

[38] D. Carluccio, M. Bermingham, D. Kent, A. G. Demir, B. Previtali, and M. S. Dargusch, *Comparative study of pure iron manufactured by selective laser melting, laser metal deposition, and casting processes,* Advanced Engineering Materials **21**, 1900049 (2019).

[39] R. J. Hellmig, M. Janecek, B. Hadzima, O. V. Gendelman, M. Shapiro, X. Molodova, A. Springer, and Y. Estrin, *A portrait of copper processed by equal channel angular pressing,* MATERIALS TRANSACTIONS **49**, 31 (2008).

[40] W. Luo, C. Qian, X. Wu, and M. Yan, *Electrochemical corrosion behavior of nanocrystalline copper bulk,* Materials Science and Engineering: A **452-453**, 524 (2007).

[41] A. Fattah-Alhosseini, M. Naseri, O. Imantalab, D. Gholami, and M. Haghshenas, *The passive film characteristics of cold deformed pure copper,* Journal of Materials Engineering and Performance **25**, 4741 (2016).

[42] A. Balyanov, J. Kutnyakova, N. Amirkhanova, V. Stolyarov, R. Valiev, X. Liao, Y. Zhao, Y. Jiang, H. Xu, T. Lowe, and Y. Zhu, *Corrosion resistance of ultra fine-grained ti,* Scripta Materialia **51**, 225 (2004).

[43] A. Fattah-alhosseini, M. Vakili-Azghandi, M. Sheikhi, and M. K. Keshavarz, *Passive and electrochemical response of friction stir processed pure titanium,* Journal of Alloys and Compounds **704**, 499 (2017).

[44] R. Rofagha, R. Langer, A. El-Sherik, U. Erb, G. Palumbo, and K. Aust, *The corrosion behaviour of nanocrystalline nickel,* Scripta Metallurgica et Materialia **25**, 2867 (1991).

[45] A. Fattah-alhosseini, M. Naseri, S. O. Gashti, S. Vafaeian, and M. K. Keshavarz, *A study on passive and electrochemical response of pure nickel in borate buffer solutions: Effect of cold deformation,* Journal of Materials Engineering and Performance **27**, 3401 (2018).

[46] W. Zhang, W. T. Huo, J. W. Lu, J. J. Hu, L. C. Zhang, and Y. S. Zhang, *Significantly improved corrosion properties of ultrafine-grained pure mg processed by sliding friction treatment,* JOM **70**, 2596 (2018).

[47] K. Ralston, N. Birbilis, and C. Davies, *Revealing the relationship between grain size and corrosion rate of metals,* Scripta Materialia **63**, 1201 (2010).

[48] H. Garbacz and A. Królikowski, *Chapter 8 - corrosion resistance of nanocrystalline titanium,* in *Nanocrystalline Titanium*, Micro and Nano Technologies, edited by H. Garbacz, I. P. Semenova, S. Zherebtsov, and M. Motyka (Elsevier, 2019) pp. 145 – 173.

[49] S. Gollapudi, *Grain size distribution effects on the corrosion behaviour of materials,* Corrosion Science **62**, 90 (2012).

[50] L. A. I. Kestens and H. Pirgazi, *Texture formation in metal alloys with cubic crystal structures,* Materials Science and Technology **32**, 1303 (2016).

[51] K. Fushimi, K. Miyamoto, and H. Konno, *Anisotropic corrosion of iron in ph 1 sulphuric acid,* Electrochimica Acta **55**, 7322 (2010).

[52] A. Schreiber, C. Rosenkranz, and M. Lohrengel, *Grain-dependent anodic dissolution of iron,* Electrochimica Acta **52**, 7738 (2007).

[53] K. Fushimi, K. Azumi, and M. Seo, *Evaluation of heterogeneity in thickness of passive films on pure iron by scanning electrochemical microscopy,* ISIJ International **39**, 346 (1999).

[54] K. Fushimi and M. Seo, *Initiation of a local breakdown of passive film on iron due to chloride ions generated by a liquid-phase ion gun,* Journal of The Electrochemical Society **148**, B450 (2001).

[55] Y. Takabatake, K. Fushimi, T. Nakanishi, and Y. Hasegawa, *Grain-dependent passivation of iron in sulfuric acid solution,* Journal of The Electrochemical Society **161**, C594 (2014).

[56] A. Schreiber, J. Schultze, M. Lohrengel, F. Kármán, and E. Kálmán, *Grain dependent electrochemical investigations on pure iron in acetate buffer ph 6.0,* Electrochimica Acta **51**, 2625 (2006).

[57] E. Martinez-Lombardia, V. Maurice, L. Lapeire, I. De Graeve, K. Verbeken, L. Kestens, P. Marcus, and H. Terryn, *In situ scanning tunneling microscopy study of grain-dependent corrosion on microcrystalline copper,* The Journal of Physical Chemistry C **118**, 25421 (2014).

[58] E. Martinez-Lombardia, Y. Gonzalez-Garcia, L. Lapeire, I. D. Graeve, K. Verbeken, L. Kestens, J. Mol, and H. Terryn, *Scanning electrochemical microscopy to study the effect of crystallographic orientation on the electrochemical activity of pure copper,* Electrochimica Acta **116**, 89 (2014).

[59] L. Lapeire, E. M. Lombardia, K. Verbeken, I. D. Graeve, L. Kestens, and H. Terryn, *Effect of neighboring grains on the microscopic corrosion behavior of a grain in polycrystalline copper,* Corrosion Science **67**, 179 (2013).

[60] J. Wang and H. Li, *Why is corrosion resistance varied for (111), (100) and (110) preferred orientation of pure aluminum in NaCl solution?* Materials Research Express **6**, 066508 (2019).

[61] M. Hoseini, A. Shahryari, S. Omanovic, and J. A. Szpunar, *Comparative effect of grain size and texture on the corrosion behaviour of commercially pure titanium processed by equal channel angular pressing,* Corrosion Science **51**, 3064 (2009).

[62] M. Bettayeb, V. Maurice, L. H. Klein, L. Lapeire, K. Verbeken, and P. Marcus, *Nanoscale intergranular corrosion and relation with grain boundary character as studied in situ on copper,* Journal of The Electrochemical Society **165**, C835 (2018).

[63] M. Orłowska, E. Ura-Bińczyk, L. Olejnik, and M. Lewandowska, *The effect of grain size and grain boundary misorientation on the corrosion resistance of commercially pure aluminium,* Corrosion Science **148**, 57 (2019).

[64] S. Bagherifard, M. F. Molla, D. Kajanek, R. Donnini, B. Hadzima, and M. Guagliano, *Accelerated biodegradation and improved mechanical performance of pure iron through surface grain refinement,* Acta Biomaterialia **98**, 88 (2019).

[65] D. Mercier, J. Światowska, S. Zanna, A. Seyeux, and P. Marcus, *Role of segregated iron at grain boundaries on mg corrosion,* Journal of The Electrochemical Society **165**, C42 (2018).

[66] S. Kim, K. Aust, U. Erb, F. Gonzalez, and G. Palumbo, *A comparison of the corrosion behaviour of polycrystalline and nanocrystalline cobalt,* Scripta Materialia **48**, 1379 (2003).

[67] M. Sabatini, L. Monaco, and U. Erb, *Corrosion of nanocrystalline and coarse-grained nickel-iron (ni-fe) alloys in neutral and alkaline sulfate environments,* Corrosion Science **163**, 108233 (2020).

[68] C. D. Taylor, *Corrosion informatics: an integrated approach to modelling corrosion,* Corrosion Engineering, Science and Technology **50**, 490 (2015).

[69] D. Macdonald and G. Engelhardt, *2.39 - predictive modeling of corrosion,* in *Shreir's Corrosion*, edited by B. Cottis, M. Graham, R. Lindsay, S. Lyon, T. Richardson, D. Scantlebury, and H. Stott (Elsevier, Oxford, 2010) pp. 1630 – 1679.

[70] G. Vachtsevanos, *Corrosion modeling,* in *Corrosion Processes: Sensing, Monitoring, Data Analytics, Prevention/Protection, Diagnosis/Prognosis and Maintenance Strategies*, edited by G. Vachtsevanos, K. A. Natarajan, R. Rajamani, and P. Sandborn (Springer International Publishing, Cham, 2020) pp. 163–229.

[71] M. Mohamed-Said, B. Vuillemin, R. Oltra, A. Marion, L. Trenty, and D. Crusset, *Predictive modelling of the corrosion rate of carbon steel focusing on the effect of the precipitation of corrosion products,* Corrosion Engineering, Science and Technology **52**, 178 (2017).

[72] T. Gießgen, A. Mittelbach, D. Höche, M. Zheludkevich, and K. U. Kainer, *Enhanced predictive corrosion modeling with implicit corrosion products,* Materials and Corrosion **70**, 2247 (2019).

[73] M. Arafin and J. Szpunar, *A novel microstructure – grain boundary character based integrated modeling approach of intergranular stress corrosion crack propagation in polycrystalline materials,* Computational Materials Science **47**, 890 (2010).

[74] N. Birbilis, M. Cavanaugh, A. Sudholz, S. Zhu, M. Easton, and M. Gibson, *A combined neural network and mechanistic approach for the prediction of corrosion rate and yield strength of magnesium-rare earth alloys,* Corrosion Science **53**, 168 (2011).

[75] S. Lishchuk, R. Akid, K. Worden, and J. Michalski, *A cellular automaton model for predicting intergranular corrosion,* Corrosion Science **53**, 2518 (2011).

[76] A. Bahmani, S. Arthanari, and K. S. Shin, *Formulation of corrosion rate of magnesium alloys using microstructural parameters,* Journal of Magnesium and Alloys **8**, 134 (2020).

[77] K. B. Deshpande, *Numerical modeling of micro-galvanic corrosion,* Electrochimica Acta **56**, 1737 (2011).

[78] D. [di Caprio], C. Vautrin-Ul, J. Stafiej, J. Saunier, A. Chaussé, D. Féron, and J. Badiali, *Morphology of corroded surfaces: Contribution of cellular automaton modelling,* Corrosion Science **53**, 418 (2011).

[79] P. T. Brewick, N. Kota, A. C. Lewis, V. G. DeGiorgi, A. B. Geltmacher, and S. M. Qidwai, *Microstructure-sensitive modeling of pitting corrosion: Effect of the crystallographic orientation,* Corrosion Science **129**, 54 (2017).

[80] *Corrosion Module User's Guide, COMSOL Multiphysics®V. 5.4*, COMSOL AB, Stockholm, Sweden (2018).

[81] K. B. Deshpande, *Validated numerical modelling of galvanic corrosion for couples: Magnesium alloy (ae44)–mild steel and ae44–aluminium alloy (aa6063) in brine solution,* Corrosion Science **52**, 3514 (2010).

[82] W. Sun, L. Wang, T. Wu, and G. Liu, *An arbitrary lagrangian–eulerian model for modelling the time-dependent evolution of crevice corrosion,* Corrosion Science **78**, 233 (2014).

[83] P. T. Brewick, V. G. DeGiorgi, A. B. Geltmacher, and S. M. Qidwai, *Modeling the influence of microstructure on the stress distributions of corrosion pits,* Corrosion Science **158**, 108111 (2019).

[84] F. Bachmann, R. Hielscher, and H. Schaeben, *Texture analysis with mtex – free and open source software toolbox,* in *Texture and Anisotropy of Polycrystals III*, Solid State Phenomena, Vol. 160 (Trans Tech Publications Ltd, 2010) pp. 63–68.

[85] F. Bachmann, R. Hielscher, and H. Schaeben, *Grain detection from 2d and 3d ebsd data—specification of the mtex algorithm,* Ultramicroscopy **111**, 1720 (2011).

[86] J. Jiang, T. Britton, and A. Wilkinson, *Measurement of geometrically necessary dislocation density with high resolution electron backscatter diffraction: Effects of detector binning and step size,* Ultramicroscopy **125**, 1 (2013).

[87] P. Konijnenberg, S. Zaefferer, and D. Raabe, *Assessment of geometrically necessary dislocation levels derived by 3d ebsd,* Acta Materialia **99**, 402 (2015).

[88] J. K. Brent L. Adams, *Ebsd-based microscopy: Resolution of dislocation density,* Computers, Materials & Continua **14**, 185 (2009).

[89] A. Bard and L. Faulkner, *Electrochemical Methods: Fundamentals and Applications* (Wiley, 2000).

[90] A. Lasia, *Determination of impedances,* in *Electrochemical Impedance Spectroscopy and its Applications* (Springer New York, New York, NY, 2014) pp. 67–84.

[91] *Application Note AC I Subject: Basics of Electrochemical Impedance Spectroscopy*, Princeton Applied Research.

[92] L. Abodi, J. DeRose, S. Van Damme, A. Demeter, T. Suter, and J. Deconinck, *Modeling localized aluminum alloy corrosion in chloride solutions under non-equilibrium conditions: Steps toward understanding pitting initiation,* Electrochimica Acta **63**, 169 (2012).

[93] E.-S. M. Sherif, *A comparative study on the electrochemical corrosion behavior of iron and x-65 steel in 4.0 wt intervals,* Molecules **19**, 9962 (2014).

[94] D. M. Dražić, *Iron and its electrochemistry in an active state,* in *Modern Aspects of Electrochemistry*, edited by B. E. Conway, J. O. Bockris, and R. E. White (Springer US, Boston, MA, 1989) pp. 69–192.

[95] T. Shinagawa, A. T. Garcia-Esparza, and K. Takanabe, *Insight on tafel slopes from a microkinetic analysis of aqueous electrocatalysis for energy conversion,* Scientific Reports **5**, 13801 (2015).

[96] W. Y. Lai, W. Z. Zhao, Z. F. Yin, and J. Zhang, *Electrochemical and xps studies on corrosion behaviours of aisi 304 and aisi 316 stainless steels under plastic deformation in sulphuric acid solution,* Surface and Interface Analysis **44**, 505 (2012).

[97] L. Bai and B. E. Conway, *AC impedance of faradaic reactions involving electrosorbed intermediates: Examination of conditions leading to pseudoinductive behavior represented in three-dimensional impedance spectroscopy diagrams,* Journal of The Electrochemical Society **138**, 2897 (1991).

[98] T. Bellezze, G. Giuliani, A. Viceré, and G. Roventi, *Study of stainless steels corrosion in a strong acid mixture. part 2: anodic selective dissolution, weight loss and electrochemical impedance spectroscopy tests,* Corrosion Science **130**, 12 (2018).

[99] M. Keddam, O. Mattos, and H. Takenouti, *Mechanism of anodic dissolution of iron-chromium alloys investigated by electrode impedances—i. experimental results and reaction model,* Electrochimica Acta **31**, 1147 (1986).

[100] C. A. Schuh, K. Anderson, and C. Orme, *Rapid assessment of anisotropic surface processes: experiments on the corrosion of inconel 600,* Surface Science **544**, 183 (2003).

[101] J. Gray, B. El Dasher, and C. Orme, *Competitive effects of metal dissolution and passivation modulated by surface structure: An afm and ebsd study of the corrosion of alloy 22,* Surface Science **600**, 2488 (2006).

[102] A. R. Zeradjanin, J.-P. Grote, G. Polymeros, and K. J. J. Mayrhofer, *A critical review on hydrogen evolution electrocatalysis: Re-exploring the volcano-relationship,* Electroanalysis **28**, 2256 (2016).

[103] L. C. Yule, V. Shkirskiy, J. Aarons, G. West, C. L. Bentley, B. A. Shollock, and P. R. Unwin, *Nanoscale active sites for the hydrogen evolution reaction on low carbon steel,* The Journal of Physical Chemistry C **123**, 24146 (2019).

[104] P. Błoński and A. Kiejna, *Structural, electronic, and magnetic properties of bcc iron surfaces,* Surface Science **601**, 123 (2007).

[105] W. B. Hutchinson, *Development and control of annealing textures in low-carbon steels,* International Metals Reviews **29**, 25 (1984).

[106] N. M. Markovića, S. T. Sarraf, H. A. Gasteiger, and P. N. Ross, *Hydrogen electrochemistry on platinum low-index single-crystal surfaces in alkaline solution,* J. Chem. Soc., Faraday Trans. **92**, 3719 (1996).

[107] J. Perez, E. R. Gonzalez, and H. M. Villullas, *Hydrogen evolution reaction on gold single-crystal electrodes in acid solutions,* The Journal of Physical Chemistry B **102**, 10931 (1998).

[108] S. J. Gutić, A. S. Dobrota, E. Fako, N. V. Skorodumova, N. López, and I. A. Pašti, *Hydrogen evolution reaction-from single crystal to single atom catalysts,* Catalysts **10** (2020).

[109] N. Marković and P. Ross, *Surface science studies of model fuel cell electrocatalysts,* Surface Science Reports **45**, 117 (2002).